

POLITECNICO DI MILANO  
Scuola di Ingegneria Industriale e dell'Informazione



**Physics-Based Stochastic Framework for  
the Quantification of Uncertainty in  
Non-equilibrium Hypersonic Flows**

In collaboration with NEQRAD Laboratory,  
Department of Aerospace Engineering,  
University of Illinois at Urbana - Champaign

Relatore: Prof. Aldo Frezzotti  
Co-relatore: Prof. Marco Panesi

Tesi di Laurea di:  
Simone VENTURI, Matr. 800433  
Corso di Laurea Magistrale in Ingegneria Aeronautica



# Abstract

A reliable prediction of the uncertainty associated with the radiative heat flux experienced by a manned vehicle during the entry in a planetary atmosphere is vitally important in order to design an appropriate Thermal Protection System and to allow a safe landing or splashdown. So far, the hypersonic community has been attesting the validity of the non-equilibrium radiative models by comparing the radiation intensity obtained from numerical simulations with the value measured in shock-tube facilities. However, the radiative intensity is only a directional component of the heat flux and not necessarily a model attested to be reliable in predicting the radiation intensity along one axis generates a fair estimate of the radiative heat flux. The present work overcomes this issue by introducing a new strategy for quantifying the inadequacy of the Multi-temperature Models (MT), the current methods of choice for describing the phenomena involved in hypersonic flows. The assumption of equilibrium within each of the plasma internal modes, common characteristic of the MT models, is here replaced by a stochastic representation of the energy levels populations; the propagation of such non deterministic feature through the flow solver and the radiative model permits an accurate and reliable characterization of the uncertainty affecting the radiative heat flux. The code SMUQ, an inverse problem solver that relies on the Bayesian Inference and that implements a Delayed Rejection Adaptive Method, has been developed by the author of this thesis in order to follow systematically the methodology just mentioned. For high speeds and low pressure (re-)entries, the results show that the proposed approach not only permits to validate the heat flux solver even if only the radiative intensity has been measured, but it also allows to reduce by the 80% the uncertainty associated with the electronic energy levels populations.

**Key Words:** Uncertainty Quantification, Model Validation, Stochastic Modeling, Delayed Rejection Adaptive Method, DRAM, Bayesian Analysis, Atmospheric Entry, Thermal Protection System, TPS, Non-equilibrium flows, Hypersonic flows, Plasma, Radiative Heat Flux, Multi-temperature models, Collisional-Radiative Models.



# Sommario

Una previsione affidabile dell'incertezza relativa al flusso radiativo di calore a cui va incontro un veicolo con equipaggio durante l'ingresso nell'atmosfera planetaria risulta avere vitale importanza allo scopo di progettare un opportuno Sistema di Protezione Termica e di consentire un sicuro atterraggio o ammaraggio. Fino ad oggi, la prassi per validare un modello per il non-equilibrium radiativo è stata comparare l'intensità di radiazione calcolata attraverso simulazioni numeriche con il valore sperimentale ottenuto tramite tubi d'urto. Tuttavia, l'intensità di radiazione rappresenta solamente un contributo direzionale al flusso radiativo ed un modello considerato attendibile per il calcolo dell'intensità lungo un particolare asse non necessariamente è altrettanto affidabile nello stimare il flusso complessivo. Il presente lavoro si svincola da tale problematica introducendo una nuova strategia per la quantificazione dell'inadeguatezza dei "Multi-Temperature Models" (modelli a più temperature), attualmente i metodi più in voga per la descrizione dei fenomeni caratteristici dei flussi ipersonici. L'ipotesi che ciascuno dei modi interni del plasma si trovi in equilibrio, propria di tali modelli, viene qui sostituita da una descrizione stocastica delle popolazioni dei livelli energetici; la propagazione di tale carattere non deterministico attraverso il solutore del flusso ed il solutore della radiazione, permette una rappresentazione più accurata ed affidabile dell'incertezza che interessa il flusso radiativo. Al fine di seguire sistematicamente la metodologia appena proposta, l'autore di questa tesi ha sviluppato un codice numerico, SMUQ, un solutore di problemi inversi fondato su Inferenza Bayesiana che implementa un "Delayed Rejection Adaptive Method". Per alte velocità e basse pressioni, i risultati mostrano che l'approccio proposto non solo permette di validare il modello per il calcolo del flusso di radiazione anche nel caso in cui si disponga solo di misure dell'intensità radiativa, ma consente anche una riduzione dell'80% dell'incertezza relativa alle popolazioni dei livelli elettronici.

“The new always happens against the overwhelming odds of statistical laws and their probability, which for all practical, everyday purposes amounts to certainty; the new therefore always appears in the guise of a miracle.”

Hannah Arendt

# Contents

<b>Abstract</b>	<b>3</b>
<b>Sommario</b>	<b>5</b>
<b>1 Motivation</b>	<b>9</b>
<b>2 Predicting the Radiative Intensity in Atmospheric (Re-)Entry</b>	<b>13</b>
2.1 Introduction . . . . .	13
2.2 Governing Equations . . . . .	14
2.2.1 Modeling the internal energy of non-equilibrium flows . . . . .	15
2.2.2 Species continuity equations . . . . .	18
2.2.3 Momentum equation . . . . .	18
2.2.4 Total energy equation . . . . .	19
2.2.5 Vibrational-electronic energy relaxation equation . . . . .	20
2.3 Chemical reactions and species productions . . . . .	20
2.4 Thermodynamic properties of the gas and energy of the modes . . . . .	21
2.5 Energy exchanges between modes and relaxation energy sources . . . . .	22
2.6 Radiation Model . . . . .	24
<b>3 Uncertainty Quantification of the Atmospheric Reentry and Non-Equilibrium Flow Quantities</b>	<b>27</b>
3.1 Introduction . . . . .	27
3.2 Verification, Uncertainty Quantification and Validation . . . . .	28
3.3 Literature Review . . . . .	28
3.4 Unexplored Areas . . . . .	30
<b>4 SMUQ: A tool for quantifying the uncertainties of the unobservable quantities</b>	<b>33</b>
4.1 Introduction . . . . .	33
4.2 Predictive Problem Statement . . . . .	33
4.2.1 Kennedy and O'Hagan's approach to model validation . . . . .	35
4.2.2 Oliver's approach to model validation . . . . .	35
4.3 Parameters Sensitivity Analysis and Parameters Calibration . . . . .	38
4.4 Calibration and Uncertainty Quantification by means of Bayesian Inference	40

4.4.1	Bayes' Theorem . . . . .	40
4.4.2	Markov Chain Monte Carlo . . . . .	42
4.4.3	Metropolis-Hasting Algorithm . . . . .	44
4.4.4	The Delayed Rejection Adaptive Method for MCMC . . . . .	48
4.5	Validation . . . . .	53
4.6	SMUQ: Stochastic Modeling for Uncertainty Quantification . . . . .	55
<b>5</b>	<b>Stochastic Modeling of the Electronic States Populations</b>	<b>61</b>
<b>6</b>	<b>Results</b>	<b>65</b>
6.1	Introduction . . . . .	65
6.2	Sensitivity Analysis and Models Reductions . . . . .	70
6.2.1	Multi-Temperature Model Sensitivity Analysis: . . . . .	71
6.2.2	Stochastic MT Sensitivity Analysis: . . . . .	73
6.2.3	Model Reduction . . . . .	75
6.3	Parameters and Hyperparameters Uncertainty Quantification . . . . .	76
6.3.1	Scenario 1: . . . . .	78
6.3.1.1	Scenario 1: Multi-Temperature Model . . . . .	78
6.3.1.2	Scenario 1: Stochastic Multi-Temperature Model . . . . .	81
6.3.2	Scenario 2: . . . . .	83
6.3.2.1	Scenario 2: Multi-Temperature Model . . . . .	83
6.3.2.2	Scenario 2: Stochastic Multi-Temperature Model . . . . .	85
6.3.2.3	Considerations . . . . .	86
6.4	Forward Propagation . . . . .	89
6.4.0.1	Scenario 1: Multi-Temperature Model . . . . .	90
6.4.0.2	Scenario 1: Stochastic Multi-Temperature Model . . . . .	94
6.4.0.3	Scenario 2: Multi-Temperature Model . . . . .	96
6.4.0.4	Scenario 2: Stochastic Multi-Temperature Model . . . . .	101
6.4.0.5	Considerations . . . . .	102
<b>7</b>	<b>Conclusions and Future Research</b>	<b>103</b>
7.1	Accomplishments . . . . .	103
7.2	Future Work . . . . .	103
<b>List of Figures</b>		<b>104</b>
<b>List of Tables</b>		<b>109</b>

# Chapter 1

## Motivation

During the decades that followed the Apollo missions and the moon landing, the space exploration has been conducted almost exclusively through unmanned vehicles. Thanks to such remote research, scientists have acquired extraordinary tools for searching for life into the furthest corners of the galaxies, for studying the past of the universe and for observing unique physical phenomena. In the eyes of the human kind, however, the charm of a man stepping on a globe different from the Earth cannot be replaced even by a telescope taking pictures of the most exotic constellation. This places a responsibility with the space engineering that goes beyond the mere colonization of a backup planet. In such view, NASA and ESA have been speeding in the last years for broadening the horizons of the manned planetary exploration.

Some of the most important peculiarities that have to be faced in designing a spacecraft for the human transportation are connected with the project of the Thermal Protection Systems (TPS). For example, differently from a capsule created for shipping a rover to another planet, a manned vehicle must be able to carry back its cruise. As a consequence, it has to support not only the entry in the planet's atmosphere, but also the reentry in the Earth's one. Moreover, the phenomena involved in such reentry appear in a different magnitude compared to the coming back from the moon; this is mainly due to two reasons: first, the temperature experienced by the heat shield increases with the velocity of the spaceship, which, in turn, is directly proportional to the distance of the planet from which the vehicle is coming from [1] (Fig. 1.1). Second, the dimensions of a manned vehicle are generally larger than an unmanned one, and a bigger capsule has to deal with larger heat fluxes. All these issues, in addition to the presence of humans on board that makes a TPS failure totally unacceptable, demand a deeper level of comprehension and description of the phenomena involved in the dissipation of the capsule's kinetic energy in order to correctly predict the temperature profile experienced by the vehicle and to design a proper heat shield.

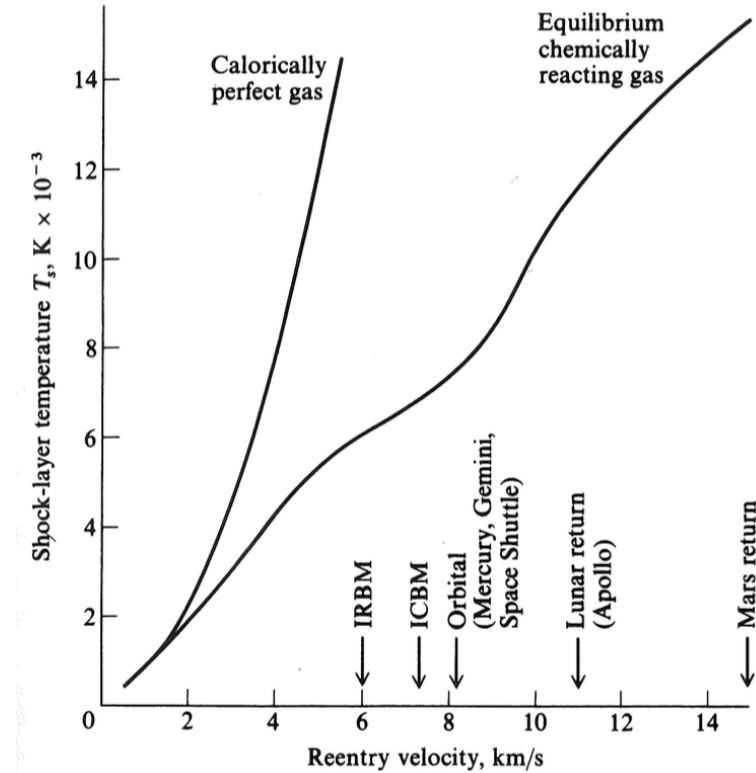


FIGURE 1.1: “Temperature behind a normal shock wave as a function of free-stream velocity at a standard altitude of 52km.” [1]

During its deceleration, the capsule transfers its kinetic energy to the thermal modes of the surrounding gas mixture. Such process generates a strong bow shock in front of the nose of the capsule and a layer of extremely hot flow (Fig. 1.2). The high temperature experienced by the gas enhances strong collisions between its particles and, based on the vehicle’s mass and velocity and on the thermodynamic and chemical characteristics of the species that form the mixture, the flow reacts differently to such sudden release of energy [1] [2] [3]:

1. Even at relative low temperatures, the energy is redistributed between the quantized modes of the atoms (translational and electronic states) and of the molecules (translational, rotational, vibrational and electronic states). For example, when the temperature of an Air mixture at constant pressure of 1atm reaches about 800K, the Nitrogen and Oxygen molecules start to be vibrationally excited.
2. At higher temperatures, the gas begins to chemically react. This means that the original molecules dissociate for forming new atoms and molecules. For Oxygen at 1atm such temperature is about 2500K, while for Nitrogen is about 1500K higher. For Air, then, the range of dissociation is 2500K to 9000K.

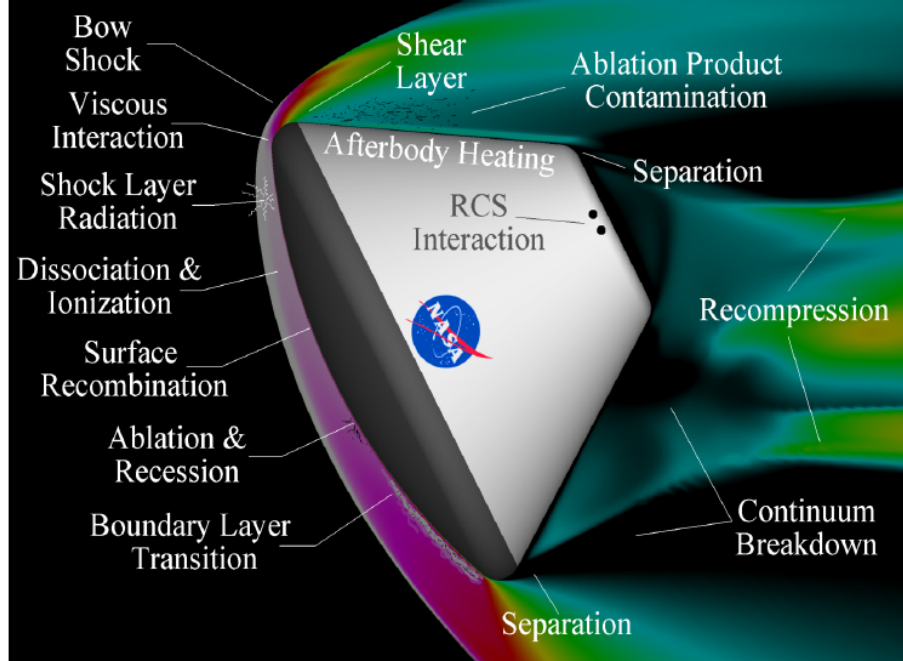


FIGURE 1.2: *Representation of the main phenomena occurring in the flow field surrounding a capsule experiencing the (re-)entry in a planetary atmosphere (courtesy of NASA).*

3. An increment of temperature after that such range is outreach can eventually cause the production of free electrons. In that case, some of the species start to ionize and the flow becomes a plasma.
4. Lastly, if the temperature of the flow field (or of some of its regions) is high enough to generate electromagnetic radiation, the species will experience de-excitations of the internal energy due to the emission of radiation and excitations of the internal states caused by its absorption. Therefore, the surface of the TPS undergoes a radiative heating that comes on the top of the standard convective heat flux.

For a manned vehicle reentering the Earth atmosphere after an interplanetary mission, the contribution of the radiative flux to the overall heating is predominant. This means that the correct prediction of the radiative intensity that the heat shield has to undergo is vitally important for designing a proper TPS that can succeed the mission and allow a safe landing (or splash down) (Fig. 1.3). However, the achievement of such goal is a hard task; the computation of the main quantities that characterize the flow surrounding a hypersonic vehicle is a complex problem that involves several different physical phenomena [4] and that represents the intersection of many disciplines, such as aerodynamics, quantum and statistical mechanics, chemical kinetics, electromagnetic theory and high performance computing [5]. The predictions of the radiation intensity

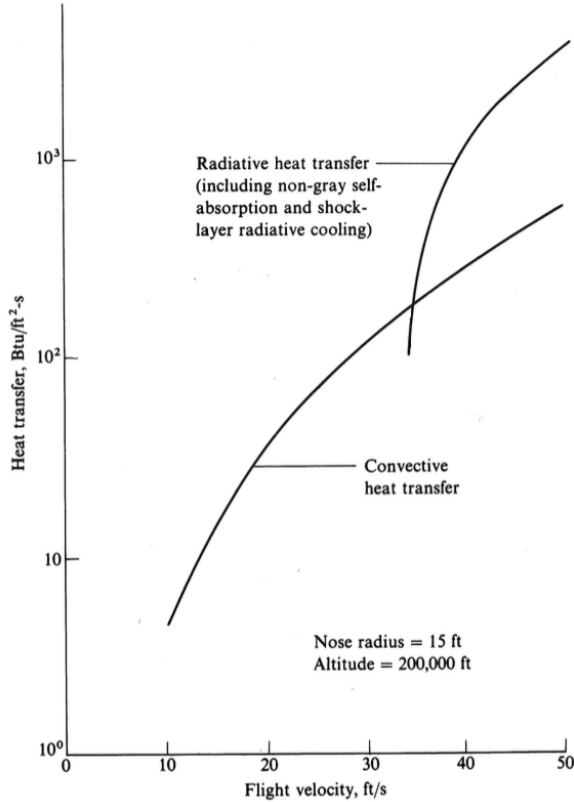


FIGURE 1.3: “Comparison of radiative and convective stagnation-point heat transfer.” [1]

made through numerical simulation are then usually characterized by significant errors. The aim of this work is to present a new strategy for quantifying the inadequacy of the Multi-Temperature Models, the current methods of choice for the description of the phenomena involved in non-equilibrium flows. The new approach relies on the computation of the error generated by the assumption of equilibrium within each of the plasma internal modes, common feature of this group of models; an accurate characterization of the uncertainty on the radiation intensity is then achieved by means of propagating such error through the flow solver and the radiative model. This thesis is organized as follows: Chap. 2 presents the physical models that have been adopted in this work for computing the main quantities of a mono-dimensional inviscid plasma flow. Chap. 3 discusses the most common approaches to the validation problem that have been used so far by the hypersonic community. Once the limitations of such methods have been explained, Chap. 4 proposes a different point of view for the validation process applied to a more generic and abstract problem. Such new perspective permits to attest the reliability in predicting unobservable quantities, as we will see, and it has been contextualized to the computation of the radiation intensity in Chap. 5. Lastly, Chap. 6 shows the results of such application and Chap. 7 reports the conclusions and outlines the future research.

# **Chapter 2**

## **Predicting the Radiative Intensity in Atmospheric (Re-)Entry**

### **2.1 Introduction**

This Chapter briefly introduces the physical models that have been used for computing the main quantities in the plasma flow surrounding the (re-)entering capsule. As It has been already mentioned, proposing a new approach for the validation of such models is the ultimate objective of this work. With this idea in mind, an exhaustive description of the phenomena involved goes beyond the purpose of this part, as well as an accurate characterization of the computational strategies which the adopted solvers rely on. Indeed, through the mechanism that will be presented in the Chap 4 different models for the non-equilibrium flow can be validated without loss of generality. For further details, the reader can refer to [1], [3], [6] and [7] for what concerns the physical aspects and to [4], [8] and [5] for the computational strategies.

As we will see, such procedure for the validation problem relies on an iterated comparison between the simulation results and some experimental data. Within the research related to hypersonic gases, most of the flow quantities measures come from the shock tubes [9], which provide a sufficiently accurate description of the thermo-chemical relaxation processes occurring in the plasma region downstream of a bow shock. The flow inside such facilities can be approximated as a one-dimensional inviscid plasma; for this reason, in Sec. 2.2 the flow governing equation are presented under such assumptions. The reacting behavior of the mixture and the internal structure of the particles introduce term that are not included in the classical Euler equations. Such peculiarities are discussed in Sec.s 2.3, 2.4 and 2.5. Lastly, Sec. 2.6 outlines the role of the radiation model in assessing the reliability of the non-equilibrium model.

## 2.2 Governing Equations

A gas mixture is composed by different chemical species that consist of a large number of atoms and molecules, in addition to free electrons in case of a plasma flow. Such particles are equipped with a certain amount of translational energy that keeps them in random motion throughout the space and with a certain amount of internal energy, which is due to the electronic excitation in case of the atom while it is also connected to the rotational and vibrational degrees of freedom in case of the molecule [10]. The physical processes occurring in the region downstream of the normal shock wave are governed by the collisions between all these particles [7]. Through such impacts, the molecules and the atoms exchange their energy and allow chemical reactions, ionizations and radiation emissions to take place. If the mixture is characterized by a low density, the particles have to travel a longer distance on average for impacting to each other (named mean free path,  $\lambda$ ) and, in turn, the collision mechanism is slow. This fact can strongly influence both the thermodynamical and the chemical states of the gas and it must be accounted in the computation of the flow quantities during the first part of the planetary entering, where altitudes are high and then densities are extremely low.

The Knudsen Number ( $Kn$ ) is a dimensionless number particularly useful in order to quantify the relative length scale of the molecular motion with respect to the macroscopic one and it is defined as the ratio between the molecular mean-free-path and the characteristic dimension of the problem under investigation (e.g., the vehicle nose radius). Such quantity permits to identify the flow regimes that the (re-)entering vehicle experiences during its trajectory (Fig. 2.1). Distinct numerical method must be used for simulating different regimes. For example, the Navier-Stokes equations (NS) are a proper representation of the flow states only in case of a continuous medium ( $Kn < 0.05$ ) while the Direct Simulation Monte Carlo (DSCM) by Bird [11] is one of the most popular method for relatively high Knudsen Number. It is important to underline, however, that the flow surrounding a large capsules is characterized by a Knudsen number higher than what a plasma around a smaller vehicle could experience at the same altitude. As a consequence, the distance from the planet at which the continuum assumption starts to hold (i.e.: about 92km for the Space Shuttle) is higher for the capsule with larger dimensions [1].

In this work, the gas inside the shock tube has been considered mono-dimensional, continuous and inviscid; the flow-solver Plato, developed at the University of Illinois at Urbana Champaign by A. Munafò', has been used for computing the flow quantities as solution of a system of equations made up of the Navier-Stokes equations for the conservation of mass, of momentum and of total energy reinforced by additional equations which permit to take into account the chemically reacting behavior of the gas and

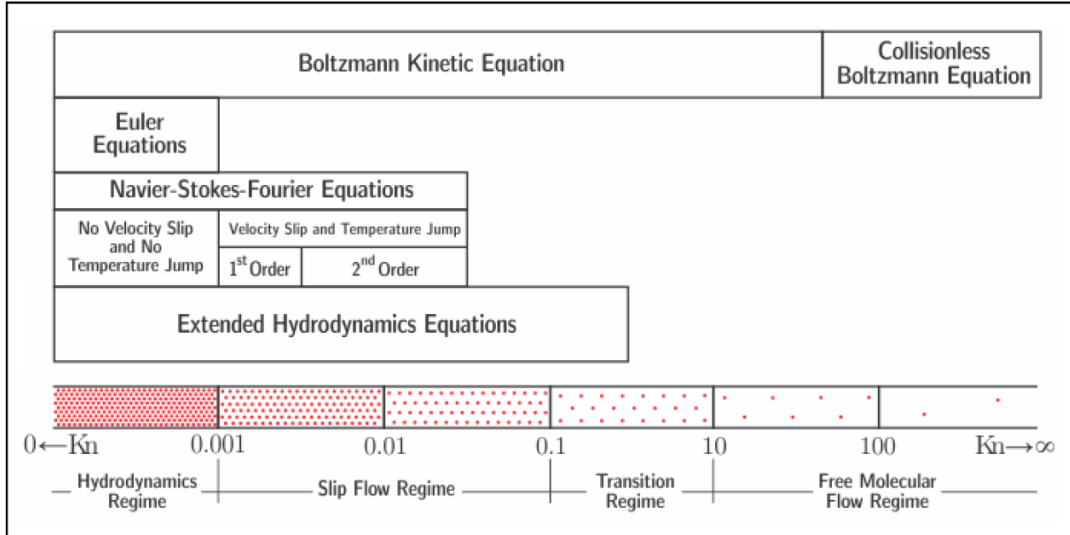


FIGURE 2.1: “Flow regime classification according to the Knudsen number” [5]

the exchange of internal energy between its particles. Such augmented system “is often referred to in literature as Multi-Temperature model (MT) or Collisional Radiative model (CR), depending on the treatment of the internal energy levels of the chemical constituents” [8].

### 2.2.1 Modeling the internal energy of non-equilibrium flows

At this point, before examining in details the above mentioned equation another fundamental dimensionless number must be introduced, that is the ratio between the convective time scale and the characteristic time of the chemical and thermodynamical processes (which is strictly connected to the characteristic time of collisions). When such dimensionless number is very large, the flow is said to be in thermo-chemical equilibrium; when the two scales are comparable, on the other hand, the regimes is referred to as non-equilibrium.

The Multi-Temperature models [7] rely on the assumption of thermo-chemical equilibrium in order to compute the energy owned by each of the internal modes of the species. For such particular regimes, the statistical mechanics contributes with an expression for characterizing how each of the quantized internal energy levels is populated [3]. Indeed, in the equilibrium regimes the fraction of the chemical species  $i$  in the quantum state  $\alpha$  takes the form of the Maxwell-Boltzmann distribution:

$$f_i^\alpha = \frac{n_i^\alpha}{n_i} = \frac{g_i^\alpha}{Q_{int_i}} \exp\left(-\frac{\epsilon_{int}^\alpha}{K_b T_{int}}\right), \quad (2.1)$$

where  $n_i$  is the number density of the species  $i$ ,  $n_i^\alpha$  is the number density of the species  $i$  in the quantum state  $j$ , characterized by an internal energy  $\epsilon_{int}^\alpha$  and a degeneracy  $g_i^\alpha$ ,  $K_b$  represents the Boltzmann constant and  $T_{int}$  indicates the characteristic temperature of the internal modes.

The internal energy can be separated into the contributions of the vibrational, rotational and electronic modes; considering each of such modes in a different equilibrium condition, it is possible to express the fraction of particles in the energy levels characterized by the quantum numbers  $v$ ,  $J$  and  $e$  as:

$$f_i^{(v,J,e)} = \frac{n_i(v, J, e)}{n_i} = \frac{g_i^v g_i^J g_i^e}{Q_{V_i} Q_{R_i} Q_{E_i}} \exp\left(-\frac{\epsilon_v}{K_b T_V}\right) \exp\left(-\frac{\epsilon_J}{K_b T_R}\right) \exp\left(-\frac{\epsilon_e}{K_b T_E}\right). \quad (2.2)$$

Once the temperatures  $T_R$ ,  $T_V$  and  $T_E$  are known, this equation allows to compute the physico-chemical properties of the flow. In order to obtain such temperatures, some conservation equations for the internal energy modes are added to the classical Navier-Stokes equations.

In a first approximation, the temperature of the rotational modes almost equals the translational temperature, while the vibrational one is very similar to the one that characterizes the population of the electron states. For this reason, Park [7] proposed a model that relies only on two temperatures: one ( $T$ ) for translational and rotational modes, and a different one ( $T_V$ ) for the vibrational and the electronic states. Such Park's TTv model is the Multi-Temperature implemented in the flow solver used in this work.

In general, the non-equilibrium effects have strong consequences on the flow properties and the thermo-chemical equilibrium assumption is inappropriate, especially at high (re-)entry speeds and for low pressure conditions. In spite of this fact, the Multi-Temperature models have been widely used by the hypersonic community because of their computational efficiency when coupled with multidimensional CFD codes.

When the non-equilibrium processes are too strong for being neglected, a more proper way for reconstructing the populations and the energies of the internal modes is provided by the Collisional Radiative models, originally proposed by Bates et al. [12]. Differently from MT models, CRs treat each of the internal states as an independent pseudo-species, governed by its own kinetics; thus, these methods do not rely on a prescribed distribution for the populations of the modes and no internal temperature is required. Fig. 2.2 is an example of the CR ability in capturing the non-equilibrium effects in a shock-tube problem (that is, the deviation from the Boltzmann distribution in the flow regions close to the shock).

Such physically based description of the dynamics of each of the levels permits a more correct representation of the overall collisional and radiative mechanisms and, as a consequence, the most accurate modeling of chemical and energy transfer processes. The

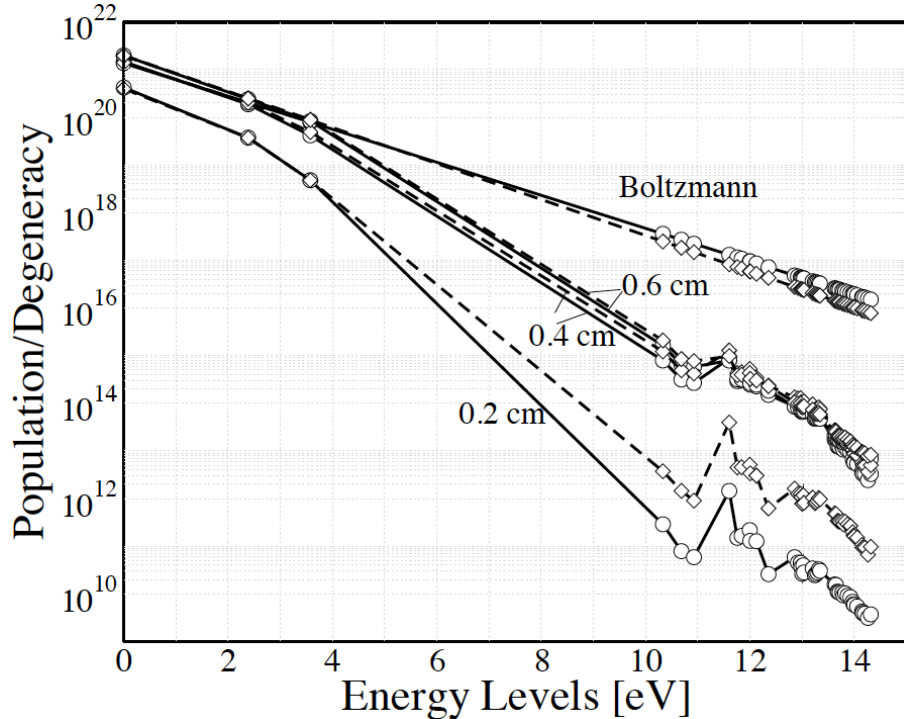


FIGURE 2.2: “Electronic energy level population for atomic nitrogen. CR model at 0.2 cm, 0.4 cm and 0.6 cm” [8].

Free stream characteristic quantities:  $P_1 = 2.0\text{Pa}$ ,  $T_1 = 195\text{K}$ ,  $u_1 = 11360\text{m/s}$ .  
Post-shock characteristic quantities:  $P_2 = 3827\text{Pa}$ ,  $T_2 = 62377$ ,  $u_2 = 1899\text{m/s}$

predictions of the non-equilibrium flow quantities obtained by means of CR models, then, are by far more reliable than the outcomes of the MT models. However, the price that one has to pay in order to obtain such improvement is a relevant increment of the computational cost. Although different hybrid models have been developed by the hypersonic community for reducing such computational effort (by increasing order of complexity and computational time: Electronic State to State models, which prescribe equilibrium distribution at temperature  $T_R$  and  $T_V$  for the rotational and vibrational modes and, at the same time, use a CR approach for computing the electronic levels populations; Vibrational State to State models, in which the rotational mode is the only one assumed to be in equilibrium), MT models still are the method of choice when the flow solver has to be coupled with a CFD codes. Nonetheless, CR simulations are a useful basis for comparison when the accuracy of some simplified model has to be attested for a particular scenario. For this reason the collisional radiative models will be extensively used in this thesis work.

In the following Subsec., the flow governing equations will be presented in a general way that allows the description of the internal states through both a Multi-Temperature model and a Collisional Radiative model.

### 2.2.2 Species continuity equations

In formulating the conservation of mass, the reacting behavior of the gas mixture must be taken into account; this is made possible by the species continuity equations, that can be written as:

$$\frac{\partial \rho_i}{\partial t} + \frac{\partial(\rho_i u)}{\partial x} = \dot{\omega}_i, \quad i \in S. \quad (2.3)$$

Here  $\rho_i$  represents the mass density of one of the  $S$  species,  $u$  is the speed of the mixture and  $\dot{\omega}_i$  is a species source term that takes into account the effects of the chemical reactions as production or depletion of the  $i$ -th species and that will be analyzed in detail in Sec. 2.3.

The classical mass conservation equation,

$$\frac{\partial \rho}{\partial t} + \frac{\partial(\rho u)}{\partial x} = 0, \quad (2.4)$$

is obtained ones that all the  $S$  equations for the species continuity are summed up, since the global mass density  $\rho$  is given by

$$\rho = \sum_{i \in S} \rho_i, \quad (2.5)$$

and the sum of the  $S$  mass productions is zero:

$$\sum_{i \in S} \dot{\omega}_i = 0. \quad (2.6)$$

### 2.2.3 Momentum equation

Under the assumption of a quasi-neutral flow, there is no net electrostatic force acting on the flow and the momentum conservation equation for the mixture can be stated as:

$$\frac{\partial(\rho u)}{\partial t} + \frac{\partial(\rho u^2 + p)}{\partial x} = 0, \quad (2.7)$$

where  $p$  represents the pressure of the mixture and it results as the sum of the partial pressures from Dalton's law:

$$p = \sum_{i \in S} p_i. \quad (2.8)$$

Due to the high temperature and the low pressure that characterize the (re-)entry process, each component of the mixture can be described with good approximation as a

perfect gas. We can thus write:

$$p = \sum_{j \in H} \rho_j \frac{\mathcal{R}}{M_j} T + \rho_e \frac{\mathcal{R}}{M_e} T_V, \quad (2.9)$$

where  $\mathcal{R}$  represents the universal gas constant,  $M_i$  indicates the species molar mass and the subscript  $e$  marks the free electrons, which are assumed to be out of the equilibrium with regard to the  $H$  heavy particles (atoms, molecules and ions) and for this reason they are characterized by the different temperature  $T_V$ .

## 2.2.4 Total energy equation

The total energy conservation equation can be stated as:

$$\frac{\partial(\rho E)}{\partial t} + \frac{\partial(\rho u H)}{\partial x} = -\frac{\partial q_{rad}}{\partial x}, \quad (2.10)$$

where  $E$  is the total energy per unit of mass ( $E = e + u^2/2$ ),  $H$  is the total enthalpy per unit of mass ( $H = E + p/\rho$ ), and the heat flux  $q_{rad}$  accounts for the energy losses due to radiation emission. In this work, the plasma will be considered as not influenced by radiation effects and thus  $q_{rad}$  will be assumed to be zero.

Given the mass fraction  $y_i = \rho_i/\rho$ , the mixture energy per unit of mass is obtained as  $e = \sum_{i \in S} y_i e_i$ ; based on the type of the particle, the species energy  $e_i$  can be expressed as:

- The sum of translational and formation contributions for electrons:  $e_e = e_e^T(T_V) + e_e^F$ .
- The sum of translational, electronic and formation contributions for the atoms:  $e_i = e_i^T(T) + e_i^E(T_V) + e_i^F$ .
- The sum of translational, electronic, vibrational, rotational and the formation contributions for the molecules:  $e_i = e_i^T(T) + e_i^R(T) + e_i^V(T_V) + e_i^E(T_V) + e_i^F$ .

All the formation energies are computed from the heat of formation at 0K. The terms  $e_i^T$ ,  $e_i^R$ ,  $e_i^V$  and  $e_i^E$  will be examined in Sec. 2.4.

### 2.2.5 Vibrational-electronic energy relaxation equation

An additional equation is added for expressing the conservation of both the free-electron translational energy and the vibrational-electronic energy of the  $M$  molecules:

$$\frac{\partial(\rho E_V)}{\partial t} + \frac{\partial(\rho u E_V)}{\partial x} = -p_e \frac{\partial u}{\partial x} + \dot{\Omega}^V, \quad (2.11)$$

where  $E_V = y_e e_e + \sum_{i \in M} y_i [e_i^V(T_V) + e_i^E(T_V)]$  and  $\dot{\Omega}^V$  represents the production and the destruction of the vibrational-electronic energy and of the free-electron energy due to collisions between particles. This term will be discussed in detail in Sec. 2.5.

## 2.3 Chemical reactions and species productions

Each of the reactions taking place in the gas mixture can be stated as:



where  $\nu'_{i_r}$  and  $\nu''_{i_r}$  represent respectively the reactants stoichiometric coefficients and the products stoichiometric coefficients for the  $i$ -th of the  $N_s$  species,  $X_i$ .

With this in mind, the Law of Mass Action [3] allows to compute the global production for the  $i$ -th species (that is, the source term in Eq. 2.3) as:

$$\dot{\omega}_i = \sum_{r=1}^{N_r} \dot{\omega}_{i_r} = \sum_{r=1}^{N_r} M_i (\nu''_{i_r} - \nu'_{i_r}) \left\{ k_{f_r} \prod_{j=1}^{N_s} \left( \frac{\rho_j}{M_j} \right)^{\nu'_{j_r}} - k_{b_r} \prod_{j=1}^{N_s} \left( \frac{\rho_j}{M_j} \right)^{\nu''_{j_r}} \right\}, \quad (2.13)$$

where  $\dot{\omega}_{i_r}$  is the  $i$ -th species production term generated by the  $r$ -th elementary reaction; such reaction is characterized by the forward rate constant  $k_{f_r}$  and by the backward rate constant  $k_{b_r}$ .

A semi-empirical Arrhenius Law [6] permits to compute the forward reaction rate as function of the temperature:

$$k_{f_r} = A_r T^{\eta_r} \exp \left( -\frac{\Theta_r}{T} \right), \quad (2.14)$$

where  $\Theta_r$  is the activation temperature and  $A_r$  and  $\eta_r$  are model parameters. In literature, the most common way for obtaining such reaction rates is fitting the experimental data and their values are then often affected by large uncertainty [8].

Eq. 2.14 is not taking into account the effects of the vibrational thermal non-equilibrium

on the reaction phenomena. The endothermic processes, for example, are faster for the vibrationally excited states; as a consequence, a smaller roto-translational temperature  $T$  is required in order to have such vibrationally excited particles dissociating. In the aim of capturing the peculiarities of non-equilibrium dissociation, the two temperature Park's model replaces the temperature in Eq. 2.14 with an average temperature  $T_{ave} = T^q T_V^{1-q}$ , where  $q = 0.5$  or  $q = 0.3$ . The forward dissociation rate then becomes:

$$k_{f_d} = A_r (T^q T_V^{1-q})^{\eta_r} \exp\left(-\frac{\Theta_d}{T^q T_V^{1-q}}\right), \quad (2.15)$$

Such approximation produces reasonable results except for conditions of strong non-equilibrium in which the translational temperature  $T$  is strongly different from the vibrational temperature  $T_V$ .

The principle of detailed balance [3] requires that the production term in Eq. 2.13 must be zero in equilibrium conditions. From this fact, it is possible to define the equilibrium constant for the  $r$ -th reaction as:

$$K_{c_r} = \frac{k_{f_r}}{k_{b_r}} = \prod_{j=1}^{N_s} \left( \frac{\rho_j}{M_j} \right)^{\nu''_{i_r} - \nu'_{i_r}}. \quad (2.16)$$

Once the Gibbs free energy  $\hat{g}_i(T)$  is computed through the statistical mechanics methods detailed in [3], it is possible to obtain the

$$\log K_{c_r}(T) = - \sum_{i=1}^{N_S} \frac{(\nu''_{i_r} - \nu'_{i_r}) \hat{g}_i(T)}{RT} - \log(RT) \sum_{i=1}^{N_S} (\nu''_{i_r} - \nu'_{i_r}). \quad (2.17)$$

At this point, through Eq. 2.16 one can obtain  $K_{b_r}$  combining  $K_{c_r}$  with the  $K_{f_r}$  that results from Eq. 2.14; the species source term can be finally computed by Eq. 2.13.

## 2.4 Thermodynamic properties of the gas and energy of the modes

Subsec. 2.2.4 pointed out that a characterization of the thermodynamic properties of the gas is required in order to make the set of equation presented in Sec. 2.2 resolvable. This goal can be achieved by approaching the problem from a statistical mechanics point of view.

As it was previously mentioned, the internal modes relax to the equilibrium conditions with different time scales; for allowing the description of this important behavior, the

internal contributions to the global energy are found to be separated in most of the widely used non-equilibrium models [7]. These are mere approximations that result from “the extrapolation of microscopic partitioning ... originated from a re-interpretation of the Born-Oppenheimer approximation” [8].

For example, the rotational and the vibrational modes are intrinsically coupled together, due to the effects that the relative positions of the nuclei has on the inertia of the molecule [13]; however, the rigid rotor and the harmonic oscillator approximations are commonly made in literature in order to separate the contribution of these two degrees of freedom. Under these two assumptions, the expressions for the energies of the modes per unit of mass of the i-th of the  $S$  species become [13]:

$$e_i^T = \frac{3}{2} R_i T \quad (2.18)$$

$$e_i^R = R_i T \quad (2.19)$$

$$e_i^V = \frac{R_i \theta_i^V}{\exp\left(\frac{\theta_i^V}{T_V}\right) - 1} \quad (2.20)$$

$$e_i^E = R_i \frac{\sum_e g_{ie} \theta_{ie}^E \exp\left(-\frac{\theta_{ie}^E}{T_V}\right)}{\sum_e g_{ie} \exp\left(-\frac{\theta_{ie}^E}{T_V}\right)} \quad (2.21)$$

where  $R_i = \mathcal{R}/M_I$  represents the specific gas constant for the i-th species,  $g_{ie}$  indicates the degeneracy of the species electronic level  $e$ ,  $\theta_i^V$  and  $\theta_{ie}^E$  are respectively the characteristic temperatures of the species vibrational and electronic modes.

The series in Eq. 2.21 diverge; thus, “the total number of electron levels is adjusted to yield the best agreement between values of the computed energies and those in the reference tables” [14].

## 2.5 Energy exchanges between modes and relaxation energy sources

A proper characterization of the source term in Eq. 2.11 is particularly important; such equation, indeed, allows to compute the vibrational energy and, thus, to obtain the vibrational temperature. In turn, this last quantity is necessary for modeling the

reaction rates, as Eq. 2.15 pointed out. The production (or depletion) of the vibrational-electronic energy is ascribable to four different source (or sink) terms:

$$\dot{\Omega}^V = \dot{\Omega}^V + \dot{\Omega}^{ET} + \dot{\Omega}^{CV} + \dot{\Omega}^I. \quad (2.22)$$

The first contribution in the right-hand side of Eq. 2.22 is due to the exchange of energy between the translational and the vibrational modes; under the following four assumptions:

- harmonic oscillator model,
- the levels are populated according to the Maxwell-Boltzmann distribution,
- transition occurring only among neighboring states,
- rate constants for the transitions are proportional to the quantum number,

such term can be expressed through the Landau Teller formula [7], [15]:

$$\dot{\Omega}^{VT} = \sum_{m \in \mathcal{V}} \frac{e_m^V(T) - e_m^V(T_{Vm})}{\tau_m^{VT}(T)}, \quad m \in \mathcal{V}, \quad (2.23)$$

where the subscript  $m$  indicates the generic molecules in the mixture. Here, the species relaxation time  $\tau_m^{VT}$  is based on the Millikan-White's formulation and includes Park's correction [19]:

$$\tau_m^{VT} = \tau_m^{MW} + \tau_m^P. \quad (2.24)$$

The additive term  $\tau_m^P$  has been proposed by Park for avoiding that the relaxation time becomes smaller than the time required for a collision to take place [16] and it can be written as:

$$\tau_m^P = \frac{U_\infty}{R_N} \frac{1}{\sigma_m \bar{C}_m n_{tot}}, \quad (2.25)$$

where  $U_\infty$  is the free-stream velocity,  $R_N$  is the dimensional nose radius of the vehicle,  $\bar{C}_m$  is the average velocity of the molecule,  $n_{tot}$  is the total number density of the gas and  $\sigma_m$  is Park's limiting cross section, that he estimated as:

$$\sigma_m = \sigma_C \left( \frac{50000}{T} \right)^2. \quad (2.26)$$

The value of the constant  $\sigma_C$  is generally assumed  $10^{-21}$ , but it is affected by strong uncertainty.

The second contribution to  $\dot{\Omega}^V$  is due to the collision between free electrons and heavy particles and it can be represented as:

$$\dot{\Omega}^{ET} = \frac{\frac{3}{2}n_e k_B(T - T_V)}{\tau_e^{ET}(T_V)}, \quad (2.27)$$

where the relaxation time comes from the kinetic theory:

$$\tau_e^{ET} = \frac{1}{\sum_{j \neq e} \frac{m_e}{m_j} \nu_{ej}}; \quad (2.28)$$

the collision frequency  $\nu_{ej} = (8/3)v_e n_j \bar{\Omega}_{ej}^{11}$ . Here,  $v_e$  represent the electron thermal velocity and  $\bar{\Omega}_{ej}^{11}$  indicates the collision cross-section for the electron impacting against a species j.

The third term in Eq. 2.22 is produced by the vibrational energy lost through dissociation:

$$\dot{\Omega}^{CV} = \sum_{m \in \mathcal{V}} C_m \left( \sum_{r \in \mathcal{R}^m} \dot{\omega}_{mr} \right) \mathcal{D}^m, \quad (2.29)$$

where  $\mathcal{R}$  is the set of reactions that involve the molecule m,  $\mathcal{D}$  indicates the dissociation energy per unit of mass of the diatomic molecules involved in the dissociation reaction r and  $C_m$  is the dissociation energy removal parameter, which characterizes the fraction of vibrational energy removed by the dissociation of the m-th molecule. From literature, the most common value for  $C_m$  is 0.3. However, this parameter is affected by uncertainty and even values of about 0.8 can be found [17], [18].

The last source terms is due to the ionization of the species caused by their impacts with free electrons. A model for such production is given by Johnston [19]

$$\dot{\Omega}^I = - \sum_{r \in \mathcal{R}^I} \dot{\omega}_{er} I_{er}, \quad (2.30)$$

where  $\dot{\omega}_{er}$  is the electron production term due to the ionization of the  $r - th$  particle and  $I_{er}$  is the related electron energy removal constant.

## 2.6 Radiation Model

As it has been already mentioned presenting the total energy equation, for the sake of this thesis the radiation model is decoupled from the plasma flow solver described above. Following the work of Miki et al. [14], radiation is only accounted for simulating the role of the shock-tube spectrometer. With the aim of validating the models that have

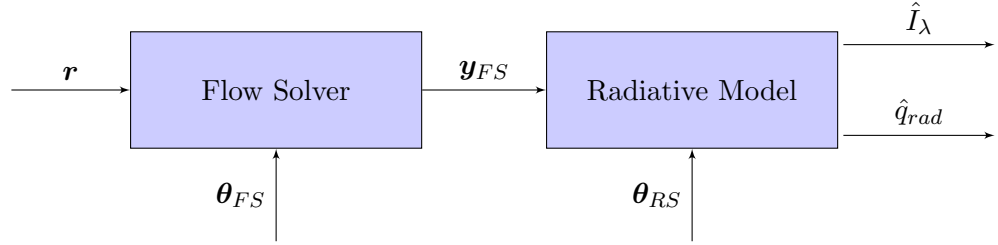


FIGURE 2.3: The radiative intensity  $\hat{I}_\lambda$  and the radiative heat flux  $\hat{q}_{rad}$  are computed by the Flow Solver and the Radiative Model in series.  $\mathbf{u}$  represents the set of the scenario inputs (e.g., free stream pressure, temperature and shock speed),  $\boldsymbol{\theta}_{FS}$  and  $\boldsymbol{\theta}_{RS}$  indicate the sets of model parameters respectively of the flow solver and of the radiative model, and  $\mathbf{y}_{FS}$  are the outputs of the flow solver (e.g., populations of the energy levels)

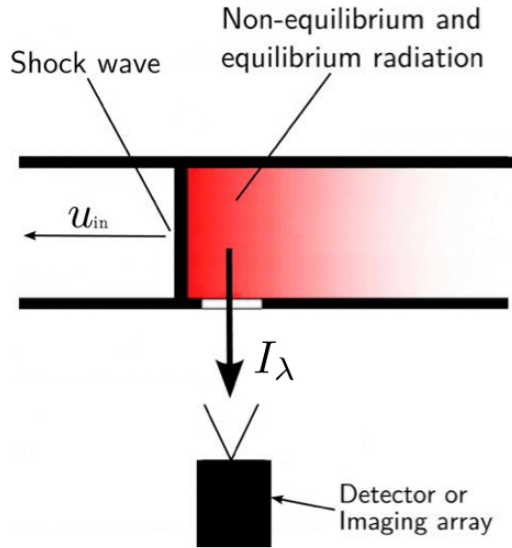


FIGURE 2.4: “Schematic description of shock-tube measurements” [14]

been used for computing the main quantities of the plasma flow, such approach permits a comparison between the numerical simulations (the computed value of the radiative intensity,  $\hat{I}_\lambda$ , Fig. 2.3) and the experimental data acquired through the arc-jet facilities (the measured value of the radiative intensity,  $I_\lambda$ , Fig. 2.4)

Previous works found that the atomic line radiation dominates the heat flux to the heat shield ([19], [20]); for this reason, the specific radiative intensity generated by the transitions between two electronic energy levels has been chosen as measured quantity (referred to as observable quantity in the following part of this thesis). Choose an arbitrary point inside a radiating gas and an arbitrary surface of area  $dA$  centered in such point and normal to a direction  $r$ ; let represent with  $dE$  the radiative energy in

the wavelength interval between  $\lambda$  and  $\lambda + d\lambda$  emitted by  $dA$  in a time interval  $dt$  along all the directions within the solid angle about  $r$ ,  $d\Omega$ . The specific radiative intensity is then defined as:

$$I_\lambda = \lim_{dA, d\Omega, d\lambda, dt \rightarrow 0} \left[ \frac{dE}{dA \ d\Omega \ d\lambda \ dt} \right]. \quad (2.31)$$

This quantity is intrinsically directional; different directions of the solid angle (identified by the spherical coordinates  $\theta$  and  $\phi$ ), thus, can be characterized by different  $I_\lambda$ . However, the specific radiative intensity related to the transitions between the couples of energy levels of interest is measured by the spectrometer only along a direction perpendicular to the shock-tube (Fig. 2.4). One can refer to [14] and to [21] for the details about how the radiation solver computes  $I_\lambda$ . What must be pointed out in this last part of the Chapter, is the key idea of this thesis work: for the reasons explained in Chap. 1, the real quantity of interest for an atmospheric (re-)entry problem is the heat flux and, in particular, the radiative contribution to such term is vitally important for a (re-)entering manned vehicle. The radiative heat flux can be computed by integrating the specific radiation intensity over all the directions and over the entire range of wavelengths [7]:

$$q_{rad} = \int_0^\infty \int_0^{2\pi} \int_0^\pi I_\lambda(\theta, \phi) \cos(\theta) \sin(\theta) \ d\theta \ d\phi \ d\lambda. \quad (2.32)$$

Let assume that the specific radiation intensity produced by the flow solver and the radiation solver coupled together matches well the shock-tube experiment. The radiative heat flux is not measurable in the facility; thus, the chance that the numerical model predicted a realistic value also for this quantity is not straightforward. The solvers, indeed, could have produced outcomes acceptable only for few directions. It is clear that a different strategy for assessing the validity of the non-equilibrium model is required. A new approach will be presented in Chap. 4 and 5.

# **Chapter 3**

## **Uncertainty Quantification of the Atmospheric Reentry and Non-Equilibrium Flow Quantities**

### **3.1 Introduction**

For particular scenarios in which experimental measures are either not feasible or too expensive, computational models are vitally important in solving problems that are at the same time crucial and complex. Here, the adjective “crucial” is a synonym for “essential in the decision-making process”; predicting the system response in order to inform some decision regarding the system itself, can be defined as a crucial problem. On the other hand, “complex” stands for “made up of several different phenomena, most of which are hard to be mathematically and physically described”; a direct consequence of this complexity is the fact that errors are unavoidable when one tries to model such phenomena.

For the reasons explained in the previous chapter, the designing process of the heat shield is a case in point of a crucial and complex problem and, at the same time, the radiative heat flux is an excellent example of a non-measurable quantity that has to be predicted through numerical simulations. All in all, these two characteristics are peculiarities of most of the problems that engineers have to face everyday and they motivate the necessity of a strategy for assessing the reliability of computational models. After having delineated a more rigorous definition of the main stages which such strategy is composed by (Sec. 3.2), Sec. 3.3 reviews the inherent literature looking for the approaches that have been used by the hypersonic community for quantifying the uncertainty in the atmospheric reentry and non-equilibrium fundamental quantities. Then, Sec. 3.4 will point out the unexplored area of research related to such problem.

## 3.2 Verification, Uncertainty Quantification and Validation

The process of assessing the reliability of computational models is usually divided into three different steps: verification, uncertainty quantification and validation [22].

Verifying a computational model means establishing its consistency with the mathematical model it is based on, or, in other words, assessing that the computational model is well implemented. It is possible to find in literature a lot of well developed techniques for ensuring that the numerical errors are small compared to other source of uncertainty [23] [22]. Therefore, the rest of this thesis will rely on the assumption that model verification can always be guaranteed.

Uncertainty quantification (UQ) is the process of estimating the error that affects the computational prediction and that is due to an inaccurate choice of the model parameters values and to a misconstrue representation of the model functional form.

Lastly, Validation is the step of “determining whether a mathematical model is a sufficient representation of reality for the purposes for which the model will be used; that is, for predicting specified QoIs (Quantities of Interest) to inform a specific decision”[24]. It is important to point out that validating a computational model is different from validating a scientific theory; indeed, while for the latter any disagreement between predictions and experiments causes the falsification of the entire theory, it is not possible to speak in absolute terms of the validity of a computational model. A valid simulation could bring to reliable predictions only for some quantities and in particular scenarios; therefore, the ultimate goal of Validation is to explicitly define which are such quantities and which are such scenarios.

## 3.3 Literature Review

- The paper of Miki *et al.* [14] can be considered one of the seminal works in the view of this thesis. The article delineates a proper procedure for the validation of the radiation intensity predictions in Hypersonic air mixtures. By means of a sensitivity analysis, the authors mathematically proved that the Nitrogen ionization rate has a vital role in the description of the non equilibrium phenomena due to a strong shock-wave. Then, they proceeded to calibrate such parameter through a Bayesian approach and to verify the values found with this process by propagating them to the observable quantities. The radiation intensities so obtained shown excellent agreement with the experiments conducted at NASA EAST shock tube.

The procedure for the sensitivity analysis adopted in the article will be used also in this thesis. The results in Chap. 6 of this manuscript will be presented for the same scenario conditions analyzed by Miki *et al.*. The code SMUQ that has been developed for obtaining such results (see next chapter) relies on the same Delayed Rejection Adaptive Method implemented in QUESO [25], the UQ solver that has been used in the paper.

- Another seminal work comes also from Miki *et al.* [26] and assesses the validity of the one temperature and two-temperatures models proposed by Park. While the observable quantity is considered to be the radiative intensity also in this paper, here the quantity of interest is the radiative heat flux. The procedure that the authors proposed is based on two different steps: calibration and propagation, that are respectively inverse and forward problems. From this work, both the one temperature and two-temperatures models result invalidated. The former because of its inadequacy in reproducing the physical phenomenon, while the latter due to the unacceptable uncertainties that it commits in predicting. However, for the reasons that will be pointed out in Sec. 4.2 of this manuscript, the strategy adopted for the validation of the prediction of the radiative heat flux is not appropriate and a different approach will be presented in the next chapter.
- Angelikopoulos *et al.* [27] applied the Bayesian Inference to the quantification of the uncertainty in Molecular Dynamics simulations and to the propagation of such discrepancies. In this work, the authors presented several strategies for reducing the computational cost of such process, like parallelization, adaptive surrogate models and efficient schedule algorithms. The improvements that the proposed methodologies permit to be achieved are shown through a simple case of study that involves liquid and gaseous argon. This article presents two main contributions to the application of the uncertainty quantification to hypersonic flows. First, a strategy for the parallelization of the Markov Chain (TMCMC) has been proposed and justified. Second, a particular approach for the propagation of the parameter uncertainty to the observable quantities has been shown; such procedure will be also adopted in this thesis work and it will be discussed in detail in the next chapter.
- In a Bayesian approach to uncertainty quantification, the inadequacy of the model in reproducing the reality is computed by means of the solution to an inverse problem; then, the way that one uses for extrapolating informations from the available data has a key role. With this in mind, Miki *et al.* [28] presented in their paper different options for taking into account the spatial correlation of the data in the uncertainty quantification of the most important parameters of the hypersonic

flows. The results proposed in their article shown that the best description of such correlation is achievable through the identification of two different characteristic lengths. However, the the results obtained through such description do not deviate too much from the outcomes of the model under the assumption of uncorrelated data as long as the error on the outputs has a multiplicative character. For this reason, the error on the observable quantities is assumed to be multiplicative and all the data points in this thesis work are considered to be uncorrelated; as we will see in the next chapter, this last approximation allows an important simplification in the implementation of the inverse problem solution, since it motivates the use of a diagonal covariance matrix in representing the likelihood function.

- In their work of 2011, Stogner *et al.* [53], focused their efforts on providing a methodology for analyzing the problem sensitivity to the heating and ablation rate and for forward propagating their uncertainty. In doing that, the convective heat flux has been treated as one of the quantity of interest. Due to the large number of dimensions of the parameter space that the authors have faced, a Latin Hypercube Sampling method has been used for the propagating. The results of such analysis has shown a strong correlation between the ablation rate and the turbulence multiplier. While this paper is intensively focused on the convective heat flux estimation, it does not take into account the radiative contribution.
- Dutta *et al.* [29] proposed to use of an adaptive filtering approach based on a covariance matching technique for calibrating the aerodynamic and atmospheric parameters involved in a spaceship entering the Martian atmosphere. While such parameters have a vital role in the computation of the capsules trajectory, the characterization of their proper values has not been intensively investigated in the past. The results presented in the paper demonstrated that the proposed method has advanced capabilities of predicting the parameters and quantifying the related uncertainty when compared to different filtering approaches. However, the work is not directly focused on the estimation of the uncertainty in hypersonic flows.

## 3.4 Unexplored Areas

The previous section has shown that a common feature of the current methods of choice for the representation of the prediction uncertainty is the addition (or the multiplication) of the model observable quantities to (by) a stochastic error. Such discrepancy is due to both the lack of knowledge about the correct values of the model parameters and to the

model structural inadequacy, as we will see in the next chapter. However, the approaches that has been found in literature do not allow to separate these two contributions. Moreover, as it will be justified in the next chapter, none of the papers that has been analyzed presents an appropriate strategy for validating the numerical models for the computation of unobservable quantities, such as the radiative heat flux.



# **Chapter 4**

## **SMUQ: A tool for quantifying the uncertainties of the unobservable quantities**

### **4.1 Introduction**

It is common practice in engineering to attest the validity of a computational model by merely comparing its outputs with the experiments. Such process has evident shortcomings; it relegates, indeed, the possibility of establishing the consistency between simulations and the real world only to cases in which an observable data is available. The different and more general approach to validation that will be presented in the first part of this chapter (Sec. 4.2) is based on a proper representation of the model uncertainty that follows the recent paper [24] by Oliver *et al.* The methods that have been used in order to solve the related calibration problem are based on the Bayesian Inference and, in particular, on a Delayed Rejection Adaptive Method applied to the Metropolis-Hasting Algorithm. All the adopted methodologies are illustrated in the second part of this unit (Sec.s 6.2, 4.4 and 4.5). Lastly (Sec. 4.6), the FORTRAN code SMUQ (Stochastic Modeling for Uncertainty Quantification) developed by the author of this thesis in order to implement the new strategy is presented in Sec. 4.6.

### **4.2 Predictive Problem Statement**

In engineering, a solution to a problem is usually obtained by means of a model that is based on various physical, mathematical or empirical theories. Some of these theories are reliable within a domain of applicability, while others, even if known to be less accurate, are the best choice in the description of a part of the phenomenon we are

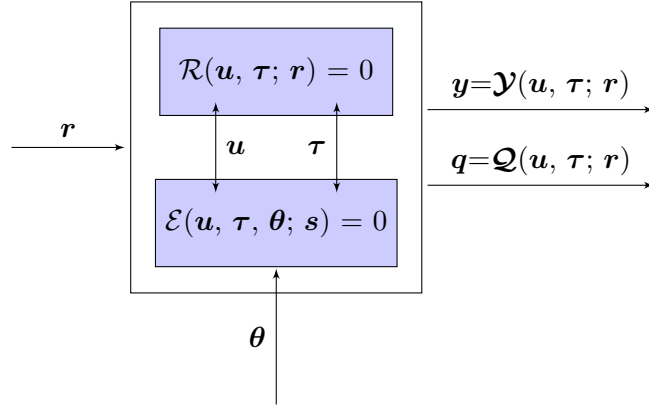


FIGURE 4.1: *Abstract problem without any model imperfection.*

interested into; this could be due, for example, either to the fact that more rigorous models are not available or to the fact that the computational cost of such meticulous models is not affordable. For this reason a generic prediction could be seen as the result of some reliable theories augmented with “embedded” models [24].

A generic reliable theory can be formulated as:

$$\mathcal{R}(\mathbf{u}, \tau; \mathbf{r}) = 0. \quad (4.1)$$

where  $\mathbf{u}$  is the state of the model,  $\mathbf{r}$  is a set of scenario variables,  $\mathcal{R}$  is the operator related to the theory and  $\tau$  represents a quantity that needs to be specified in order to solve the problem.

In most of the practical cases, a biunivocal correspondence between  $\tau$  and  $(\mathbf{r}, \mathbf{u})$  either does not exist or is very hard to be expressed. Therefore, the problem is not closed and the dependence of  $\tau$  on other variables need to be made explicit through an embedded model:

$$\mathcal{E}(\mathbf{u}, \tau, \theta; \mathbf{s}) = 0, \quad (4.2)$$

where  $\theta$  is a set of model parameters and  $\mathbf{s}$  represent the set of scenario variables, which is either a subset of  $\mathbf{r}$  ( $\mathbf{s} \subseteq \mathbf{r}$ ) or an empty set.

Fig. 4.1 shows schematically such composite feature of the model. In spite the fact the observable quantities  $\mathbf{y}$  and the Quantities of Interest  $\mathbf{q}$  have all the same characteristic of being the model outputs, in the Figure they are clearly distinguished. This is because the observable quantities are defined to be all the outputs of the model that can be compared with some available data, while no data is accessible for directly inspecting the QoI. The consequences of this difference will be analyzed later in this Section. In any case,  $\mathbf{y}$  and  $\mathbf{q}$  are all univocally determined by the model states  $\mathbf{u}$ , the scenario parameters  $\mathbf{r}$  and the embedded model quantities  $\tau$ .

### 4.2.1 Kennedy and O'Hagan's approach to model validation

The description of the abstract problem discussed above relies on the assumption that the prediction made through the embedded model is not affected by any error. This condition is hard to satisfy. Indeed, failure of the model in delivering an accurate prediction can be due to, firstly, the lack of knowledge on the parameters  $\boldsymbol{\theta}$ ; secondly, the model could be affected by a structural inadequacy, namely its functional form could be not correct. This results in the generation of approximate values for the embedded model variables,  $\boldsymbol{\tau}_m \approx \boldsymbol{\tau}$ , and the error so created will be propagated to the observable quantities and to the QoIs.

Kennedy and O'Hagan proposed a solution for taking into account “the difference between the true value of the real world process and the code output at the true values of the inputs” [30]; they opted for adding the outputs of some stochastic models to the computational results, as in Fig. 4.2:

$$\mathbf{y} = \mathcal{Y}(\mathbf{u}, \boldsymbol{\tau}_m; \mathbf{r}) + \boldsymbol{\delta}_y(\boldsymbol{\alpha}; \mathbf{r}), \quad (4.3)$$

where  $\boldsymbol{\alpha}$  is a set of hyperparameters and  $\boldsymbol{\delta}_y$  is the output of a stochastic model ( $SM_1$ ), created to represent the error in predicting the observable quantities due to the structural uncertainty. The usefulness of such stochastic description will be clarified later in this chapter.

What needs to be underlined in this context, however, is the fact that such characterization of the model error is unable to propagate the structural uncertainty to the quantities of interest. In fact, while it is possible to take advantage of the data for “tuning” the hyperparameters  $\boldsymbol{\alpha}$  so that  $\mathbf{y} \sim \mathbf{D}$ , it is not possible to do the same for  $\boldsymbol{\beta}$ ; there is no available data, indeed, for comparing the QoIs.

For this reason, we need a second stochastic model ( $SM_2$ ) in representing the consequences of the model inconsistency on the QoI:

$$\mathbf{q} = \mathcal{Q}(\mathbf{u}, \boldsymbol{\tau}_m; \mathbf{r}) + \boldsymbol{\delta}_q(\boldsymbol{\beta}; \mathbf{r}). \quad (4.4)$$

### 4.2.2 Oliver's approach to model validation

Kennedy and O'Hagan's approach clearly has some limitations. First,  $\boldsymbol{\beta}$  is a set of hyperparameters that needs to be calibrated together with  $\boldsymbol{\alpha}$  and  $\boldsymbol{\theta}$ , but, differently from the latter, no data is accessible for such operation. Second, even assuming that

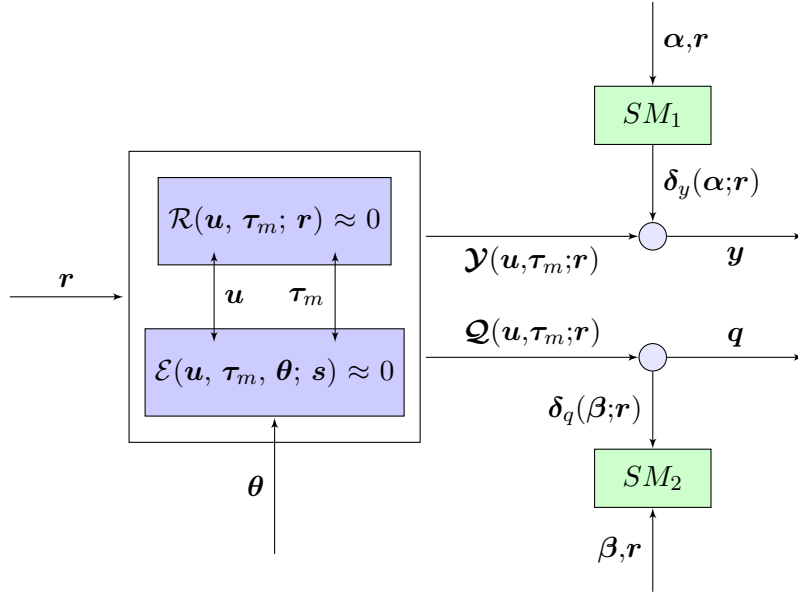


FIGURE 4.2: *Kennedy-O'Hagan's representation of the model uncertainty.*

some strategy for obtaining  $\beta$  can be implemented, there is no way for testing  $\delta_q(\beta; \mathbf{r})$ ; in order to validate the model, in fact, only the observable quantities  $\mathbf{y}$  are compared to data and  $\beta$  does not affect  $\mathbf{y}$  in any way. Thus, a different approach is required.

Oliver *et al.* proposed in their paper “to take advantage of the structure of the composite model to introduce model uncertainty representation that can be informed and tested using data” [24]. The key point of such approach is to represent the structural error at its actual source, so that the uncertainty modeling can influence both the observed quantity and the QoI simultaneously (Fig. 4.3). The composite structure of the model allows to attribute the structural discrepancy only to  $\tau_m$ ; if some of the origins of such discrepancy (e.g., the physical and mathematical approximations and phenomena lack of knowledge) are known, one can represent the recognize sources of uncertainty through a stochastic model characterized by some hyperparameters  $\alpha$ . In this way, the error that in Kennedy and O'Hagan's approach has been simply added to the output can be now partially moved upstream to augment the embedded physical model:

$$\tau \approx \tau_m(\mathbf{u}, \theta; \mathbf{s}) + \epsilon_m(\mathbf{u}, \alpha; \mathbf{s}). \quad (4.5)$$

The method for obtaining  $\epsilon_m$  is problem-dependent and “is driven by physical knowledge about the nature of error as well as practical considerations necessary to make computations with the model tractable” [24]. Anyway, such stochastic contribution will be propagated downstream to both  $\mathbf{y}$  and  $\mathbf{q}$ ; because of that, one can acquire information about  $\alpha$  from data and then transfer that knowledge directly to the QoI through the prediction. The only contribution that does not affect the Quantity of Interest is  $\epsilon_r$ , the residual part of the error, generated through the Kennedy and O'Hagan's stochastic

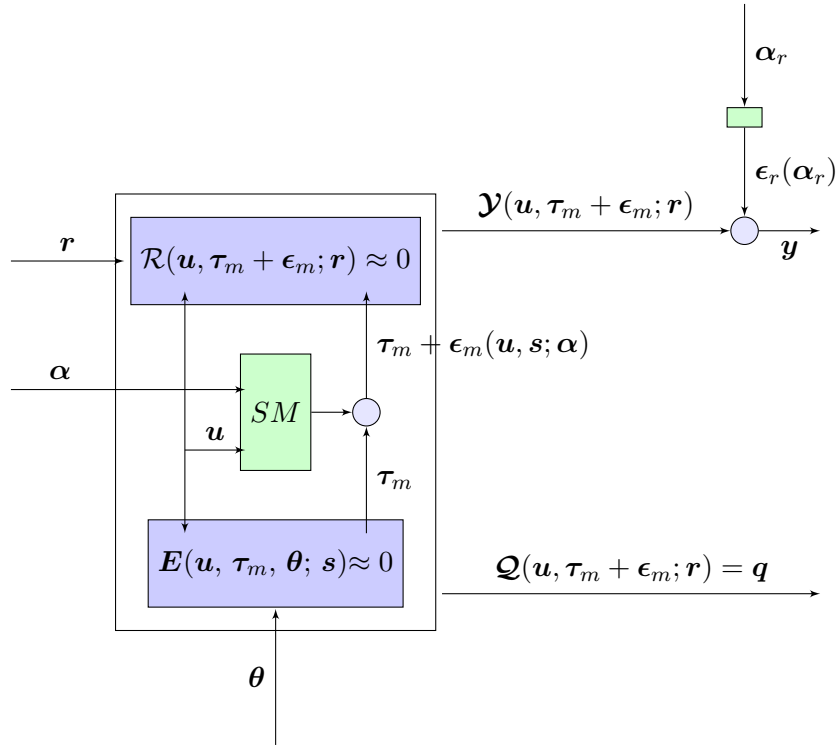


FIGURE 4.3: *Representation of the model uncertainty proposed by Oliver et al.*

term added to the output, governed by the hyperparameters  $\alpha_r$ . Such uncertainty takes into account the physical and mathematical aspects of the phenomena of interest that we have not been able to capture through the stochastic model used for augmenting the embedded model. The more this last stochastic model is physically-based, the more the Kennedy and O'Hagan's is reduced, the more the prediction of the QoI is reliable.

At this point, it is important to motivate the choice of a stochastic representation for the model inadequacy even if the physical phenomenon being described is deterministic. We should start with underlying the different nature of the hyperparameters  $\alpha$  and the parameters  $\theta$ , which is consequence of the different hierarchical levels which they belong to. In the most simple terms, while a single set of  $\theta$  truly represent the parameters of a particular model, a set of  $\alpha$  can be used to generate  $n$  different sets of parameters.

For example, assuming that a particular parameter  $\gamma$  appears in our model, we can decide to characterize it in a deterministic way; this would bring us to calibrate directly the value of  $\gamma$  (that is,  $\gamma \in \theta$ ). On the other hand, we could represent  $\gamma$  in a stochastic way by means of a normal distribution:  $\gamma = \mathcal{N}(\mu_\gamma, \sigma_\gamma)$ . In such case, we must calibrate the hyperparameters  $\mu_\gamma$  and  $\sigma_\gamma$  instead of calibrating directly  $\gamma$  (that is,  $\mu_\gamma, \sigma_\gamma \in \alpha$ ); it is clear that from a single couple of values of such mean and such standard deviation one can generate  $n$  different values for the parameter  $\gamma$ . Thus, the operation of tuning used for computing  $\gamma$  has a different meaning compared to the connotation of calibrating the hyperparameters  $\mu_\gamma$  and  $\sigma_\gamma$ ; this is because the former case is based on the assumption

that a unique true value of the parameters set has to be determined.

In the approach that we are considering for representing the model error, we are separating the contribution due to the uncertainty on the parameters from the the contribution that comes from the structural inadequacy; such goal is achieved by considering  $\theta$  and  $\alpha$  on different hierarchical levels. The stochastic model  $\epsilon_m$  represents the connection between such levels, and it is what allows a proper representation of the structural inadequacy: even in the hypothetical situation where we know the best values for all  $\theta$ , we would still be able to describe the uncertain nature of the QoIs thanks to the several values of parameters that have been generated by the stochastic model from a single set of  $\alpha$ .

In this paragraph it has been pointed out that a proper representation of the structural error as in Fig. 4.3 is worthy in order to make a reliable prediction. The next two Sections, therefore, will be focused on providing a methodology that takes advantage on such representation for quantifying the uncertainty in the prediction of the Quantities of interest.

## 4.3 Parameters Sensitivity Analysis and Parameters Calibration

As mentioned before, the available data plays an essential role in the model validation; indeed, the comparison of such experimental results with the different outcomes of the model allows to extrapolate information about the uncertainty on the QoIs.

Fig. 4.3 highlighted all the factors that could affect the computational output: the scenarios variables  $r$ , the embedded model parameters  $\theta$  and the stochastic model hyperparameters  $\alpha$ . That means that, once the functional forms are defined for the embedded and the stochastic models, there is no way for obtaining different outcomes  $y$  but changing at least one of the values of  $r$ ,  $\theta$ ,  $\alpha$ . Moreover,  $r$  is dictated by the scenario that one is interested into and it is assumed to be known without any error; that means that our degrees of freedom are restricted to parameters and hyperparameters. The computational model, therefore, can have different outcomes only varying  $\theta$ ,  $\alpha$ .

With this in mind, the problem of making reliable predictions could be seen as the problem of finding the proper ranges in which each one of the parameters / hyperparameters can vary without generating outputs  $y$  that are too different from the data values  $D$ . Problems of this type are called calibration problems.

When an output should be considered too different from the data will be clarified in the following Sections; what should pointed out here, anyway, is the basic assumption

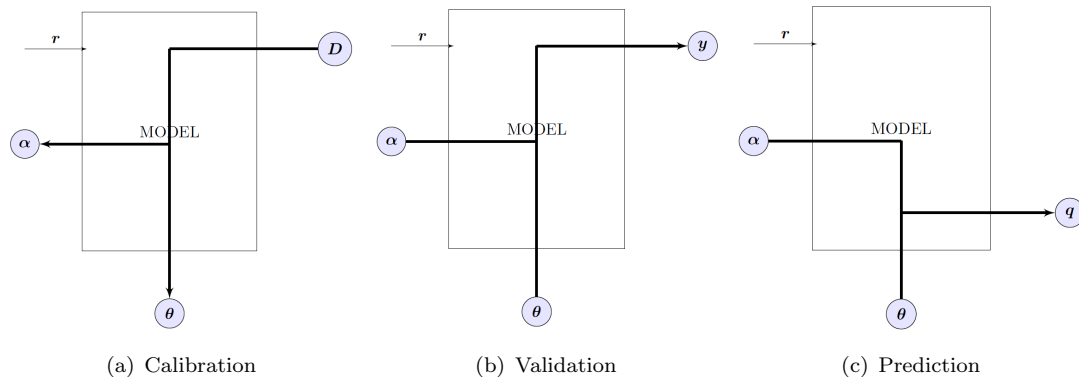


FIGURE 4.4: *The process of making reliable predictions for unobservable quantities.*

that has been made: if  $\mathbf{y}$  is the output of the model that has a particular set of  $\boldsymbol{\theta}, \boldsymbol{\alpha}$  as inputs and  $\mathbf{y}$  is “comparable” to  $\mathbf{D}$ , then the QoIs  $\mathbf{q}$  obtained with the same set of parameters will be “similar” to their true values for the same scenario conditions, and the prediction must be considered reliable. Such statement relies on the hypothesis that through the creation of the stochastic model we encapsulated all the main sources of uncertainty that can affect  $\mathbf{y}$  and  $\mathbf{q}$ .

The model parameters, thus, can be seen a sort of “accumulators of information” that can be “charged” by the data during the calibration process; such accumulators can then “release” all the information that they stored to both the observable quantities (for validating the model) and to the Quantities of Interest (for making predictions) (Fig. 4.4).

This analogy is also useful for underlining that different parameters could be equipped with different “capacities” of accumulating the information that comes from the data. The model, in fact, could be more sensitive to a particular  $\theta_i$  (or to a  $\alpha_i$ ) than to a different  $\theta_j$  ( $\alpha_j$ ); moreover, it could happen that a generic  $\theta_i$ , even if good for storing the information that comes from the data, is not capable to transmit such knowledge to any of the  $q$ . Sensitivity analysis is the proper tool for assessing which subset of the available  $\boldsymbol{\theta}$  and  $\boldsymbol{\alpha}$  has an active role in making a reliable prediction and it can be of vital importance in the first part of the validation process. Indeed, solving an inverse problem is generally complicated and a minimization of the dimensions of the space, where one is looking for a possible solution would consequently reduce such complexity. Model reduction can be achieved by means of ranking  $\boldsymbol{\theta}$  and  $\boldsymbol{\alpha}$  based on their correlation with the QoIs and subsequently discarding the unessential parameters and hyperparameters [14].

## 4.4 Calibration and Uncertainty Quantification by means of Bayesian Inference

Calibration belongs to a broader category of problems, the so called inverse problems, that aim at determining the model inputs from which the known observable quantities have been generated. In the last century, different approaches has been developed for solving the inverse problems [31]; one of the most efficient method is the Bayesian Inference, that relies on Bayes' theorem.

### 4.4.1 Bayes' Theorem

Bayes' Theorem can easily be explained starting from the two assumptions that Cox pointed out in 1946 with the purpose of “providing a basis for the principles of probable inference” [32]. The starting point of his paper is the consideration that, in order to have a logical reasoning, the truth of a statement requires an explicit quantification. This can be guaranteed, at least in a transitive manner, by ranking with a real number each of the propositions, so that the most reliable one is associated with the highest value. Consequently, Cox started to investigate what mathematical rules such real numbers must respect; by means of Boolean logic and algebra, he came to the conclusion that the consistency of reasoning can be satisfied only if all the propositions obey the two fundamental laws of the probability theory, that are the *sum rule* and the *product rule*. The former states that, if one specifies how much a hypothesis X could be true, then he is implicitly defining how much the same hypothesis X could be false. This rule can be expressed mathematically as:

$$p(X|M) + p(\bar{X}|M) = 1, \quad (4.6)$$

where  $p( )$  is a generic Probability Density Function (PDF), the  $\bar{X}$  represents the statement that X is false and M denotes the background information; it is fundamental to explicitly define M because probabilities are never absolute quantities and they always have to be related to the information at hand.

The second rule asserts that: when one specifies how much the proposition Y could be believed to be true and how much the proposition X could be believed to be true given that Y is true, he is also implicitly quantifying how much he believes that both X and Y are true:

$$p(X, Y|M) = p(X|Y, M) p(Y|M). \quad (4.7)$$

This two simple but effective rules have a number of different consequences, one of which is Bayes' theorem:

$$p(X|Y, M) = \frac{p(Y|X, M) \times p(X|M)}{p(Y|M)}. \quad (4.8)$$

This equation comes directly from the product rule, simply interchanging X with Y taking into account that  $p(X, Y|M)$  can be commutated in  $p(Y, X|M)$ . Even if it is quite straightforward, this theorem is incredibly powerful: as stated by Sivia [33], “the importance of this property to data analysis becomes apparent if we replace X and Y by hypothesis and data”:

$$p(\text{hypothesis} | \text{data}, M)p(\text{data} | \text{hypothesis}, M) \times p(\text{hypothesis} | M). \quad (4.9)$$

The strength of Bayes' theorem, indeed, is the fact that it permits to compute the probability that a hypothesis is correct given the data simply taking advantage of the probability that we would have observed the data if such hypothesis was true; this last quantity is definitely easier to determine.

It is important to note that the inequality in Eq. 4.8 has been replaced with a proportionality in Eq. 4.9. That is motivated by the fact that in a lot of practical applications (e.g., calibration) the omission of  $p(\text{data}|M)$  does not represent a big issue, as it will be explained better in the next paragraph.

With the aim of showing the potential of Bayes' theorem in solving a generic inverse problem, we apply Eq. 4.9 to an abstract problem represented as in Subs. 4.2.2 and sketched as in Fig. 4.3.

The hypothesis that must be considered in this context is the fact that, if we prescribe a particular set of values  $\boldsymbol{\theta}, \boldsymbol{\alpha}$  to the parameters and to the hyperparameters, the model outcome would be exactly the data ( $\mathbf{y} = \mathbf{D}$ ). If we want to establish the truth of such hypothesis given the data, we can write:

$$\Pi(\boldsymbol{\theta}, \boldsymbol{\alpha} | \mathbf{D}, M) \propto L(\mathbf{y} = \mathbf{D} | \boldsymbol{\theta}, \boldsymbol{\alpha}, M) \times p(\boldsymbol{\theta}, \boldsymbol{\alpha} | M). \quad (4.10)$$

$p(\boldsymbol{\theta}, \boldsymbol{\alpha} | M)$  represents the probability of finding the proper set of values of parameters and hyperparameters taking advantage only of the knowledge antecedent to the new data acquisition (e.g., literature, old experiments, common sense, ...); for this reason this PDF is called prior distribution. If for each of the  $\theta$  parameters and each of the  $\alpha$  hyperparameters such information is supposed to be independent from the knowledge available for the other  $\boldsymbol{\theta}, \boldsymbol{\alpha}$ , the total prior can be computed by:

$$p(\boldsymbol{\theta}, \boldsymbol{\alpha} | T) = \prod_{i=1}^T p(\theta_i | M) \times \prod_{j=1}^A p(\alpha_j | M). \quad (4.11)$$

The importance of the prior is in the fact that it makes the inverse problem being a process of uploading preexisting information instead of a mere creation of knowledge *ex novo*.

The other PDF on the right-hand side,  $L(\mathbf{y} = \mathbf{D} | \boldsymbol{\theta}, \boldsymbol{\alpha}, \mathbf{M})$ , is called likelihood distribution and it represents the probability of obtaining an output equal to the data ( $\mathbf{y} = \mathbf{D}$ ), given the model and its uncertainty.

We motivated in the last part of Sec. 4.2, that a stochastic representation must be coupled to the embedded model in order to make reliable predictions; thus, the presence of a second hierarchical level has to be taken into account when we want to compute the likelihood. If  $\gamma_k$  is one parameter that originates from  $\alpha_{1_k}, \alpha_{2_k}, \dots, \alpha_{n_k}$  through the stochastic models  $\epsilon_{m_k}(\mathbf{u}, \mathbf{s}; \alpha_{1_k}, \alpha_{2_k}, \dots, \alpha_{n_k})$ , a particular value of such  $\gamma_k$  has a probability  $p(\gamma_k | \alpha_r, \dots, \alpha_s, \mathbf{M})$  of being generated. We can then rewrite the Likelihood in Eq. 4.10 as:

$$L(\mathbf{y} = \mathbf{D} | \boldsymbol{\theta}, \boldsymbol{\alpha}, \mathbf{M}) = \int_{\mathbf{I}_{\boldsymbol{\gamma}}} l(\mathbf{y} = \mathbf{D} | \boldsymbol{\theta}, \boldsymbol{\gamma}, \mathbf{M}) \times \prod_{k=1}^p p(\gamma_k | \alpha_{1_k}, \dots, \alpha_{n_k}, \mathbf{M}) d\boldsymbol{\gamma} \quad (4.12)$$

where  $l(\mathbf{y} = \mathbf{D} | \boldsymbol{\theta}, \boldsymbol{\gamma}, \mathbf{M})$  represents the probability of obtaining an output  $\mathbf{y}$  such that  $\mathbf{D} = \mathbf{y}$  when the values of  $\boldsymbol{\theta}, \boldsymbol{\gamma}$  and  $\mathbf{M}$  are prescribed. The assumption made here is that the intersection of the various sets of hyperparameters that generate each  $\gamma_k$  is an empty set, and this results in the probabilities  $p(\gamma_k | \alpha_{1_k}, \dots, \alpha_{n_k}, \mathbf{M})$  being independent of each other.

Eq. 4.10 allows to conclude that Bayes' Theorem allows to solve the calibration problems in a probabilistic way that relies on the combination of two different states of information: the first state is a priori and independent of the measurements, while the second state is based on some observable quantities. Because of such probabilistic approach, the solution will be a Probability Density Function over the parameter space.

#### 4.4.2 Markov Chain Monte Carlo

An analytical characterization of the PDF in Eq. 4.10 is possible only in the case in which the distribution has a very simple shape. Moreover, central estimators (e.g., mean and median) and estimators of dispersion (e.g., standard deviation) cannot be useful tools when the PDF is far from being unimodal. “For more general probability distributions, one needs to perform an extensive exploration of the model space. Except for problems with a very small number of dimensions, this exploration cannot be systematic as the number of required points grows too rapidly with the dimension of the space” (Tarantola [31]).

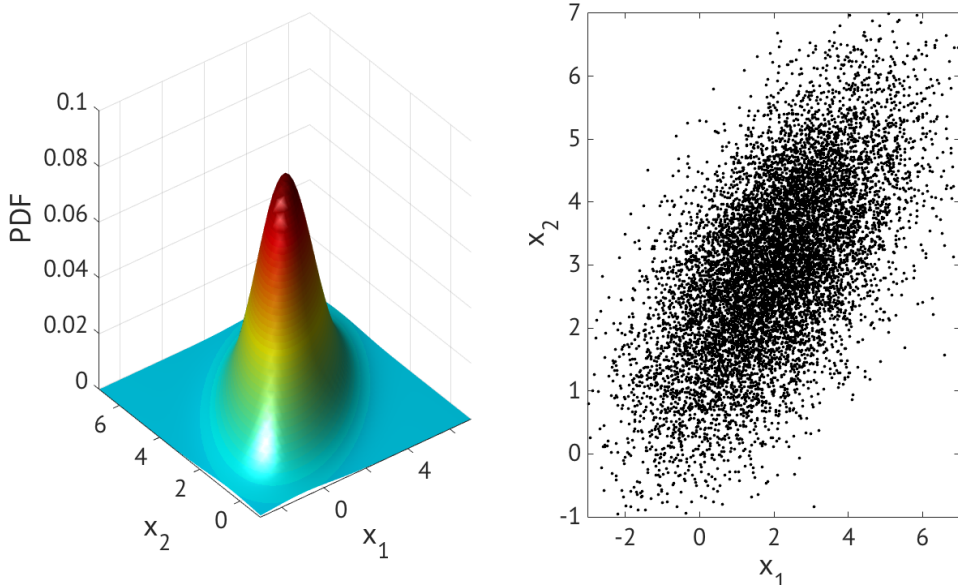


FIGURE 4.5: 10000 uncorrelated points obtained from sampling a multivariate normal distribution with  $\mu = [2, 3]$  and  $\sigma = [3, 1.5; 1.5, 2]$ .

Sampling the posterior overcomes the limitations due to the complexity of such distribution when solving the inverse problem. Sampling a generic PDF  $p$  (Fig. 4.5) means obtaining from  $p$  a set of independent points such that the probability of finding a point inside any domain  $\mathcal{D}$  is equal to the probability of the domain  $\mathcal{D}$  itself. In the last seventy years several random methods have been developed for efficiently characterizing a generic PDF by means of samples. A broad category of such methodology is the Monte Carlo (MC) sampling methods [34]; these approaches are based on the remark that high-dimensional spaces are inclined to be very empty; this fact has huge consequences on the effort that one has to address into obtaining some property of the distribution function. For example, computing the area of a circle by means of randomly throwing “darts” in points uniformly distributed over the cartesian plane is much simpler than retrieving the volume of a sphere by the equivalent approach in three dimensions. This is because, the probability of choosing a point randomly in the space and finding such point inside the n-dimensions hypersphere tends to zero very quickly when the number  $n$  of the space dimensions increases. Due to the feature that has just been pointed out, solving such high dimensional problems on deterministic grids means wasting a lot of computational time.

The main aspects that differentiates the MC methods are the strategies that they adopt for obtaining efficient random grids.

The approach that has been extensively used in this thesis is a specific type of Monte Carlo methods, known as Markov Chain Monte Carlo (MCMC). Before introducing the

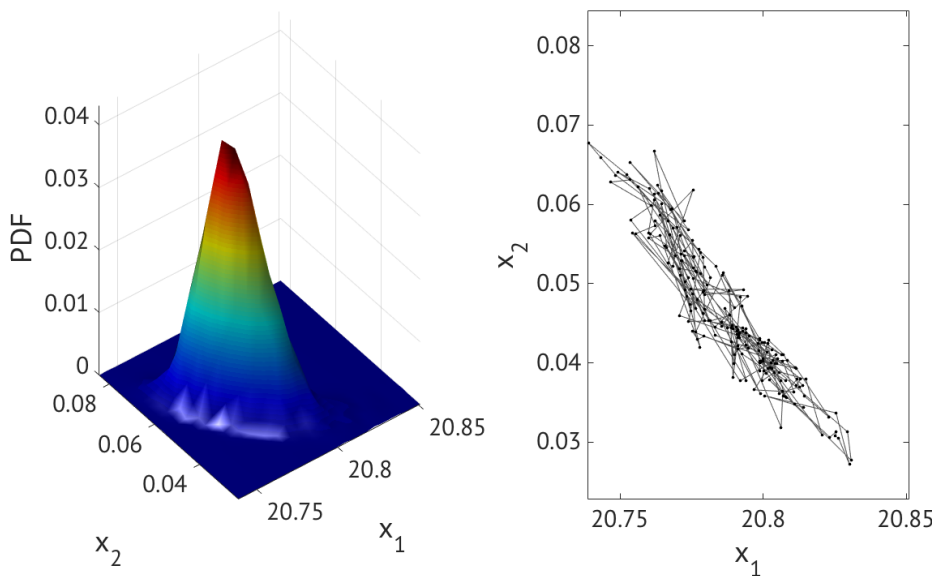


FIGURE 4.6: A Markov chain random walk (b) for sampling 200 points from a generic PDF (a).

definition of Markov chain, the notion of Markov process must be recalled. A random variables  $X$  is a Markov process if at each generic time instant  $t$  the probability of a transition to a new state  $s_j$  depends only on the current state  $s_i = X_t$ :

$$P(i \rightarrow j) = p(X_{t+1} = s_j \mid X_0 = s_0, \dots, X_t = s_i) = p(X_{t+1} = s_j \mid X_t = s_i) \quad (4.13)$$

A Markov chain is then a sequence of random draws  $X_0, \dots, X_n$  generated by a Markov process and characterized by a transition probability  $P(i \rightarrow j)$ .

Fig. 4.6 shows a Markov chain created in order to sample a particular PDF. It is possible to notice that such succession of points explores the space by means of a random walk, something similar to a Brownian motion.

#### 4.4.3 Metropolis-Hastings Algorithm

As it has been pointed out each point of a Markov chain does not have memory of how the previous points have been collected. Such important feature has been exploited by Metropolis and Hastings in the algorithm that bears their name.

With the aim of sampling a PDF  $p(X) = f(X)/C$ , where  $C$  is a generic normalizing constant and  $f(X)$  is another PDF, the Metropolis Algorithm produces a sequence of points with this iterative procedure:

1. Choose an initial value  $X_0$  such that:  $f(X_0) > 0$ .

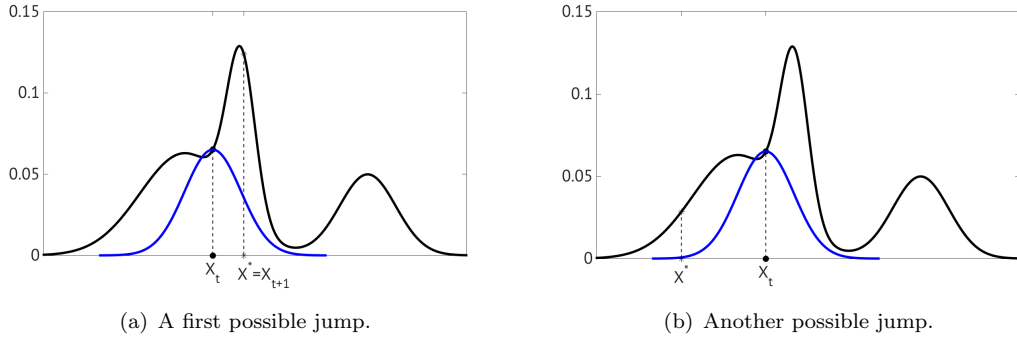


FIGURE 4.7: *Metropolis Algorithm: Two candidate jumps for the PDF  $P(X)$  (black lines) obtained from the current point  $X_t$  by means of the same proposal  $q(X_i, X_{i+1})$  (blue lines, not normalized). The  $X^*$  proposed in (a) will certainly be accepted in the ( $\alpha = 1.90$ ), while the  $X^*$  in (b) will be rejected with a probability of 56% ( $\alpha = 0.4370$ )*

2. Sample a candidate draw  $X^*$  from a proposal PDF  $q$  with the property of being symmetric (that is, a distribution such that the probability  $q(X_i, X_{i+1})$  of moving from a point  $X_i$  to a point  $X_{i+1}$  is the same of the probability  $q(X_{i+1}, X_i)$  of coming back to  $X_{i+1}$  from  $X_i$ ); then compute the probability  $f(X^*)$  (Fig. 4.7).
  3. Compute the ratio between the PDF  $p(X)$  at the proposed point  $X^*$  and at the current point  $X_t$ :
- $$\alpha = \frac{p(X^*)}{p(X_t)} = \frac{f(X^*)}{C} \frac{C}{f(X_t)} = \frac{f(X^*)}{f(X_t)} \quad (4.14)$$
4. If  $\alpha \geq 1$ , then accept the candidate point (that is, set  $X^* = X_{t+1}$ ).  
If  $\alpha < 1$ , then accept the proposed point with probability  $\alpha$  (e.g., if  $\alpha = 0.9$ , then nine times out of ten  $X^*$  must be accepted to be  $X_{t+1}$ );  
else reject  $X^*$  and keep  $X_t$  ( $X_{t+1} = X_t$ ).

The Metropolis-Hastings Algorithm is a generalized version of the Metropolis procedure that allows to use an arbitrary (i.e.: not necessarily symmetric) proposal distribution  $q(X_i, X_{i+1})$  by setting the acceptance probability for the proposed point as:

$$\alpha = \min \left( 1, \frac{f(X^*) q(X^*, X_t)}{f(X_t) q(X_t, X^*)} \right) \quad (4.15)$$

There are two key-ideas inside these algorithms: on the one hand the proposal helps to restrict the domain where to look for a candidate new point; on the other hand, the acceptance rules permits to give more importance to the regions of the space where the PDF is higher. The combination of these two features has important consequences on the performances of the Metropolis-Hastings Algorithms. In fact, it is possible to demonstrate that the Metropolis-Hastings sampling produces a Markov chain whose equilibrium

PDF is the distribution  $P(X)$  that we want to characterize. Moreover, it could be mathematically proven that, between all the acceptance-based approaches, the Metropolis-Hastings Algorithms are the most efficient way for sampling a distribution [35]. This means that they generate the highest percentage of accepted proposed values without losing uncorrelation between the points of the sampling.

Another aspect makes the Metropolis-Hastings Algorithms to be a powerful tool for solving an inverse problem: thanks to the fact that they need only the ratio between two successive values of the target distribution, such algorithms overcome the complex computation of the constant of proportionality in the case the PDF that we want to be sampled is the posterior in Eq. 4.10.

A relevant remark at this point should be made with regard to a strategy for choosing the Proposal function. The Proposals in Fig. 4.8 are represented through three normal distributions with same mean  $\mu_q$  but with three different  $\sigma_{q_1}$  (Fig. 4.8(a)),  $\sigma_{q_2} = \sigma_{q_1}/2$  (Fig. 4.8(c)) and  $\sigma_{q_3} = \sigma_{q_1}/4$  (Fig. 4.8(e)).

The consequences that such heterogeneities have on the Markov chains are shown in Fig. 4.8(b), Fig. 4.8(d) and Fig. 4.8(f). It is easy to notice how a relatively high  $\sigma_q$  causes a very poorly mixed chain (Fig. 4.8(b)); this must be related to the fact that the domain spanned by the proposal includes some widespread region in which  $P(X)$  is zero; this is particularly true when the current value  $X_t$  is at the borders of the target PDF. As consequence, several proposed draws  $X^*$  will come out with a very low probability  $\alpha$  of being accepted and the chain will spend a lot of time stuck in the current value  $X_t$ .

On the other hand, a relatively low  $\sigma_q$  (Fig. 4.8(e)) produces a very slow random walk, due to the fact that the beneficial growth of the acceptance rate is accompanied by the decrease in size of the jump between two successive points. Thus, the proposed value  $X^*$  will have a high probability of being accepted, but at the same time it will be very close to the current value  $X_t$ .

The last two examples underline that the percentage of accepted values is a good estimator for the quality of the chain mixing: low percentages are synonymous of poorly dense chain, while high percentages are symptomatic of a random motion that needs a huge amount of points for exploring the entire support of  $p(X)$ .

The best compromise for obtaining a well mixed chain (Fig. 4.8(d)) through a Metropolis-Hastings Algorithm is choosing a proposal with a medium variance, as in Fig. 4.8(c); such trade-off permits to obtain an accepting ratio of about 0.5.

Independently of how one decides to represent the proposal distribution, a poor choice of the algorithm starting point can question the fast convergence of the chain to a stationarity distribution. Moreover, in case of a multimodal target PDF (like the  $p(X)$  plotted in black in the previous figures) combined with a narrow proposal, moving from

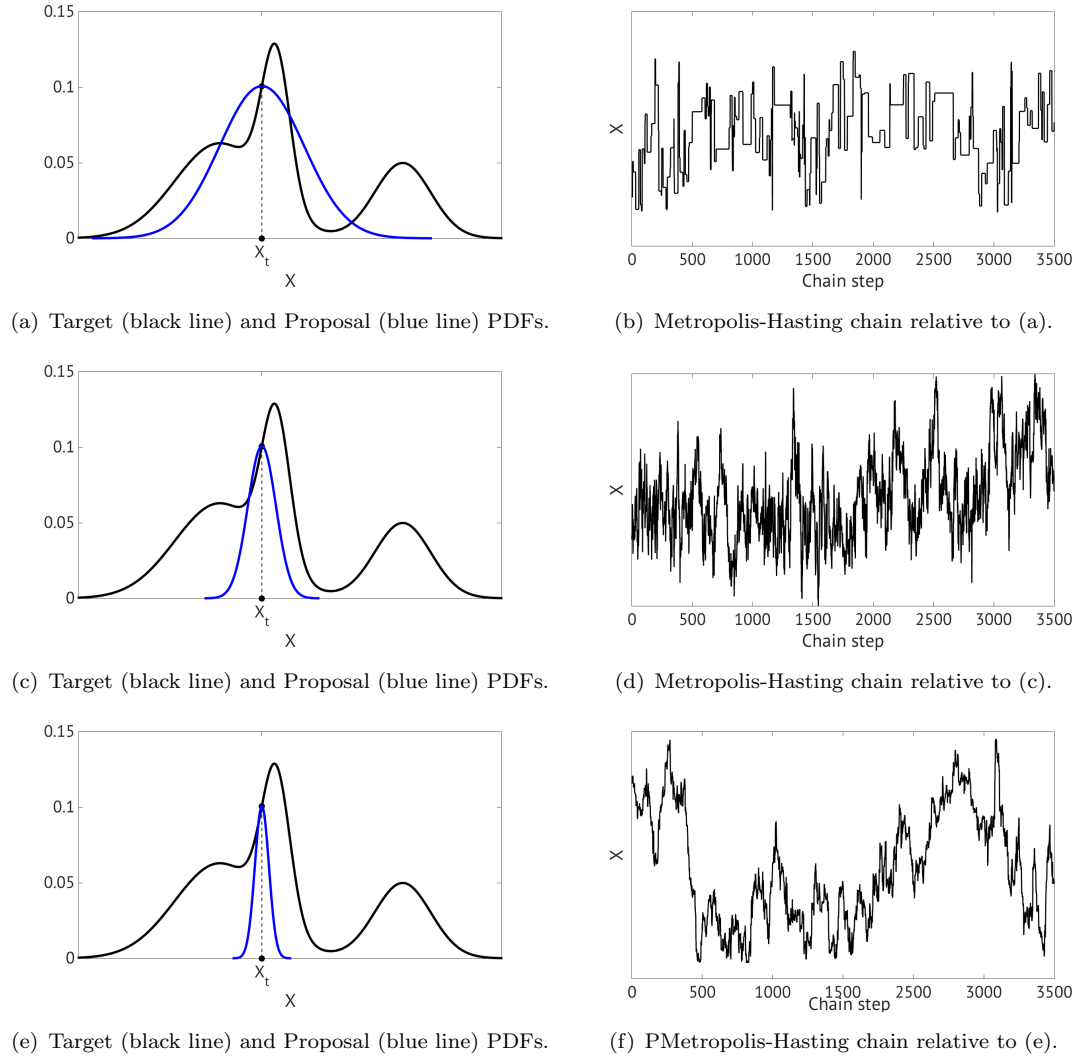


FIGURE 4.8: *Metropolis Algorithm:*  
*On the left column: three different proposal functions (blue lines):*  
 $q_1 = \mathcal{N}(\mu_q; \sigma_q = \sigma_{q_1})$  (a),  $q_2 = \mathcal{N}(\mu_q; \sigma_q = \sigma_{q_1}/2)$  (c),  
 $q_3 = \mathcal{N}(\mu_q; \sigma_q = \sigma_{q_1}/4)$  (e).

*On the right column: three different Metropolis-Hastings Markov chains produced by means of three different proposal functions, respectively: (b) from (a), (d) from (c) and (f) from (e).*

one mode region to another one becomes very hard and, as consequence, the chain could be poorly mixed.

Different solutions to such problems have been proposed in the last decades (e.g., Simulated Annealing approach [36]). However, a possible way for simply overcoming such issues is creating multiple chains that start from different highly dispersed initial values [37]. As we will see in the next Section, this technique is computationally particularly convenient when the algorithm has been parallelized on multiple processors and to each one of the cores has been assigned the realization of an independent chain.

All that has been shown in this Section for the generic variable  $X$  can be of course generalized for a vector of variables,  $\mathbf{X} = \{X_1, X_2, \dots, X_n\}$ , in case the PDF  $P(\mathbf{X})$  would be defined above a multidimensional space. For example, with the assumption of the proposal function  $q_i(X_{i_t})$  for the  $i$ -th variable at computational time instant  $t$  being independent with respect to all the other  $n-1$  proposals for the variables  $X_{j_t}$ , one can write the acceptance probability for the proposed point as:

$$\alpha = \min \left( 1, \frac{f(X^*) q_1(X_1^*, X_{1_t}) q_2(X_2^*, X_{2_t}) \dots q_n(X_n^*, X_{n_t})}{f(X_t) q_1(X_{1_t}, X_1^*) q_2(X_{2_t}, X_2^*) \dots q_n(X_{n_t}, X_n^*)} \right) \quad (4.16)$$

and the sampling assumes the form of  $n$  random walks, each one in a different dimension. However, as it will be explained in detail in the next Subsection, this could not be the best way for extending the Metropolis-Hasting Algorithms to a multidimensional space.

#### 4.4.4 The Delayed Rejection Adaptive Method for MCMC

A number of different solutions has been developed for improving the Metropolis-Hasting Algorithm. In 2001 Green and Mira presented the Delayed Rejection Method (DR) [38], an approach that particularly helps when a proper representation of the proposal distribution is hard to find. We have seen from Fig. 4.8 that a Proposal with large standard deviation causes either to be stuck in the same point or to travel a long distance in moving to the new accepted value. While the first (very likely) case has negative consequences on the chain convergence chain, the second event is beneficial in order to have a fast exploration of the parameter space. DR approach follows from such consideration. The main idea is starting to propose a candidate draw  $X_i^*$  produced by means of a distribution with a large covariance  $\mathbf{Q}$ ; then, upon rejection of such candidate point, instead of keeping  $X_{i+1} = X_i$  one should try with a new draw  $X_i^{*'}$ , obtained from a proposal with a smaller standard deviation  $\mathbf{Q}' < \mathbf{Q}$ . Green and Mira motivated this process as follows: “The advantage of DR over these alternatives is that a hierarchy between kernels can be exploited so that kernels that are easier to compute in terms of CPU time are tried first, thus saving terms on simulation time. Moves that are more “bold” are tried at earlier stages thus allowing the sampler to explore the state space more efficiently following a sort of “first bold” versus “second timid” tennis-service strategy” [39]. Also, the same authors proved in the same paper that this rejection process can be repeated for a prefixed number of stages without nullifying the Markovian property of the chain.

Fig. 4.9 gives a better picture of the DR procedure for a mono-dimensional Metropolis Algorithm. Assume that we fixed the maximum number of stages for which the DR can be repeated in case of rejections (here  $n_{DR} = 3$ ), and the constant  $\omega_{DR}$  that will divide

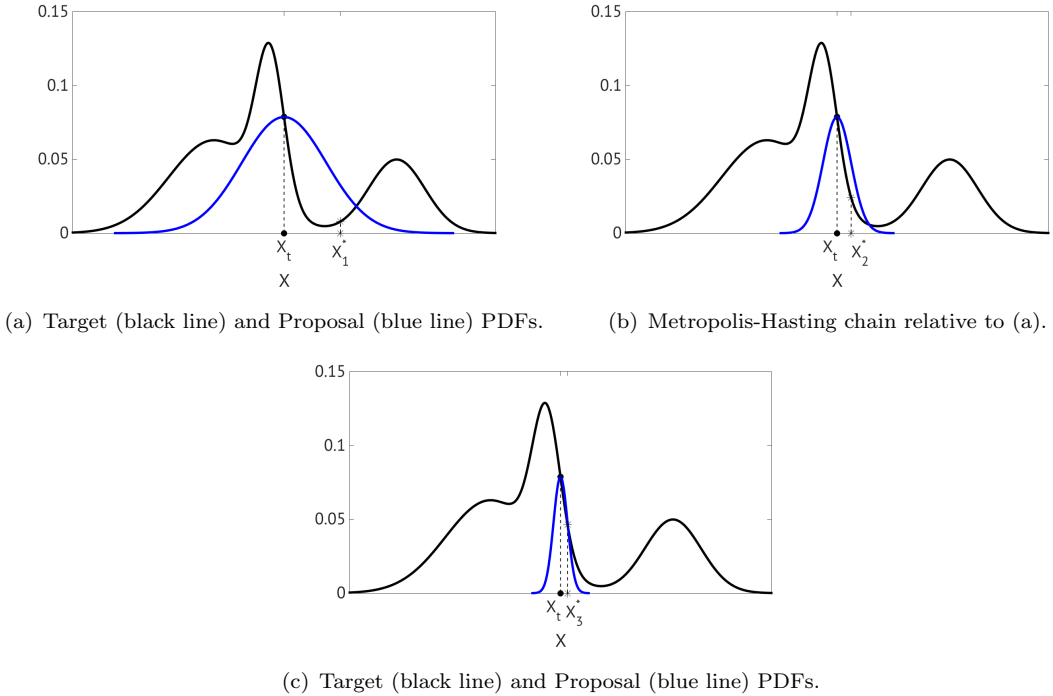


FIGURE 4.9: *Delayed Rejection Method:*

A first candidate point  $X^*$  has been obtained in (a) sampling a normal proposal distribution with  $\sigma_q$  and it has been rejected. A new proposal has then been computed with  $\sigma'_q = \sigma_q/2$  and it generated a candidate  $X^{*'}\text{ (b)}$ . This point has been rejected as well and a new point  $X^{*''}$  has been produced from a new distribution with  $\sigma''_q = \sigma_q/4$  (c).

the proposal standard deviation at each of the stages. In Fig. 4.9(a) a first candidate point  $X^*$  is obtained by a proposal with standard deviation  $\sigma_q$  and this value will give in turn an acceptance probability of 10% ( $\alpha = 0.1$ ). Then, supposing that  $X^*$  has been rejected, we try again we a new proposal created dividing the old standard deviation by the constant  $\omega_{DR}$  ( $\sigma'_q = \sigma_q/\omega_{DR}$ ) and we obtain a candidate  $X^{*'}\text{ with probability of being accepted equal to } 30\%$  (Fig. 4.9(b)). Presuming that also this point has been rejected, we will produce a last Proposal; this time ( $\sigma''_q = \sigma'_q/\omega_{DR} = \sigma_q/\omega_{DR}^2$ ). A point  $X^{*''}$  is computed from such distribution (Fig. 4.9(c)) and this draw has a probability of being accepted equal to 59%. At this point, considering that we spent all our attempts ( $i_{DR} = n_{DR} = 3$ ), there are two options: likely,  $X^{*''}$  will be confirmed and therefore  $X_{t+1} = X^{*''}$ ; in the unlucky case that also this third point is rejected, we would have to give up and keep the current value  $X_t$  as the new one.

Another improovment of the Metropolis-Hasting Algorithm is achievable through the Adaptive Method (AM) proposed by Haario *et al.* [40]. The key idea of such process is to take advantage of the previous accepted points for correcting the proposal distribution. In other words, the AM modifies the proposal's covariance matrix, so that its

principal axis could be aligned to the main directions of the random walk.

This method starts with assuming a generic proposal during an entire non-adaptation period  $n_{AM_0}$ ; this is required for letting the chain take its time with finding the preferential directions of evolution. At the first step greater than  $n_{AM_0}$ , the proposal is set to be centered at the current position of the Markov chain and to have covariance:

$$\mathbf{Q}_n = s_d (\text{Cov}(\mathbf{X}_0, \dots, \mathbf{X}_{n-1}) + \epsilon \mathbf{I}_d) \quad (4.17)$$

where  $s_d$  is a scaling parameter (that Gelman suggested to set as  $s_d = 2.4^2/d$  with  $d$  representing the number of dimensions [37]),  $\epsilon$  is a parameter that ensures that  $\mathbf{Q}_n$  will not become singular and  $\text{Cov}(\mathbf{X}_0, \dots, \mathbf{X}_{n-1})$  is the covariance matrix computed using the previous points:

$$\text{Cov}(\mathbf{X}_0, \dots, \mathbf{X}_{n-1}) = \frac{1}{k} \left( \sum_{i=0}^k \mathbf{X}_i \mathbf{X}_i^T - (K+1) \bar{\mathbf{X}}_k \bar{\mathbf{X}}_k^T \right) \quad (4.18)$$

where  $\bar{\mathbf{X}}_k = \frac{1}{k+1} \sum_{i=0}^k \mathbf{X}_i$ .

At the following steps of the chains, the matrix  $\mathbf{Q}$  will then be updated through the points collected in the meantime; the new covariance will be:

$$\mathbf{Q} = s_d (\text{Cov}(\mathbf{X}_0, \dots, \mathbf{X}_{t-1}) + \epsilon \mathbf{I}_d), \quad t > n_{AM_0}. \quad (4.19)$$

Moreover, it can be shown that  $C_t$  satisfies the more handy recursive formula:

$$\mathbf{Q}_t = \frac{t-2}{t-1} \mathbf{Q}_{t-1} + \frac{s_d}{t-1} \left( (t-1) \bar{\mathbf{X}}_{t-2} \bar{\mathbf{X}}_{t-2}^T - t \bar{\mathbf{X}}_{t-1} \bar{\mathbf{X}}_{t-1}^T + \mathbf{X}_{t-1} \mathbf{X}_{t-1}^T + \epsilon \mathbf{I}_d \right). \quad (4.20)$$

This mechanism of modifying the proposal is shown in Fig. 4.10; if the target distribution is defined above a multidimensional space, this technique allows to start the chain with an independent proposal for each of the variables (that is, with a diagonal covariance matrix for representing  $\mathbf{Q}$  for all the  $\mathbf{X}_i < n_{AM_0}$ ). Indeed, under the assumption that  $n_{AM_0}$  is large enough, the Adaptive Method itself will take into account the correlation that we are missing by means of learning from the random walk path.

Haario *et al.* proved in the same paper that such form of adaptation is an ergodic process, although it does not generate a Markov chain due to the dependence of the proposed values upon the history of the random walk. In summary, DR and AM are two approaches for adapting the proposal distribution to the target PDF  $P(\mathbf{X})$ . However, while the former aims to reach a local adaptation of  $\mathbf{Q}$  based on the shape of  $P(\mathbf{X})$  at the current point  $\mathbf{X}_i$ , the latter has the goal of globally adapting the proposal based on the chain past history.

Considering that in general the target PDF is far from being a single-mode normal

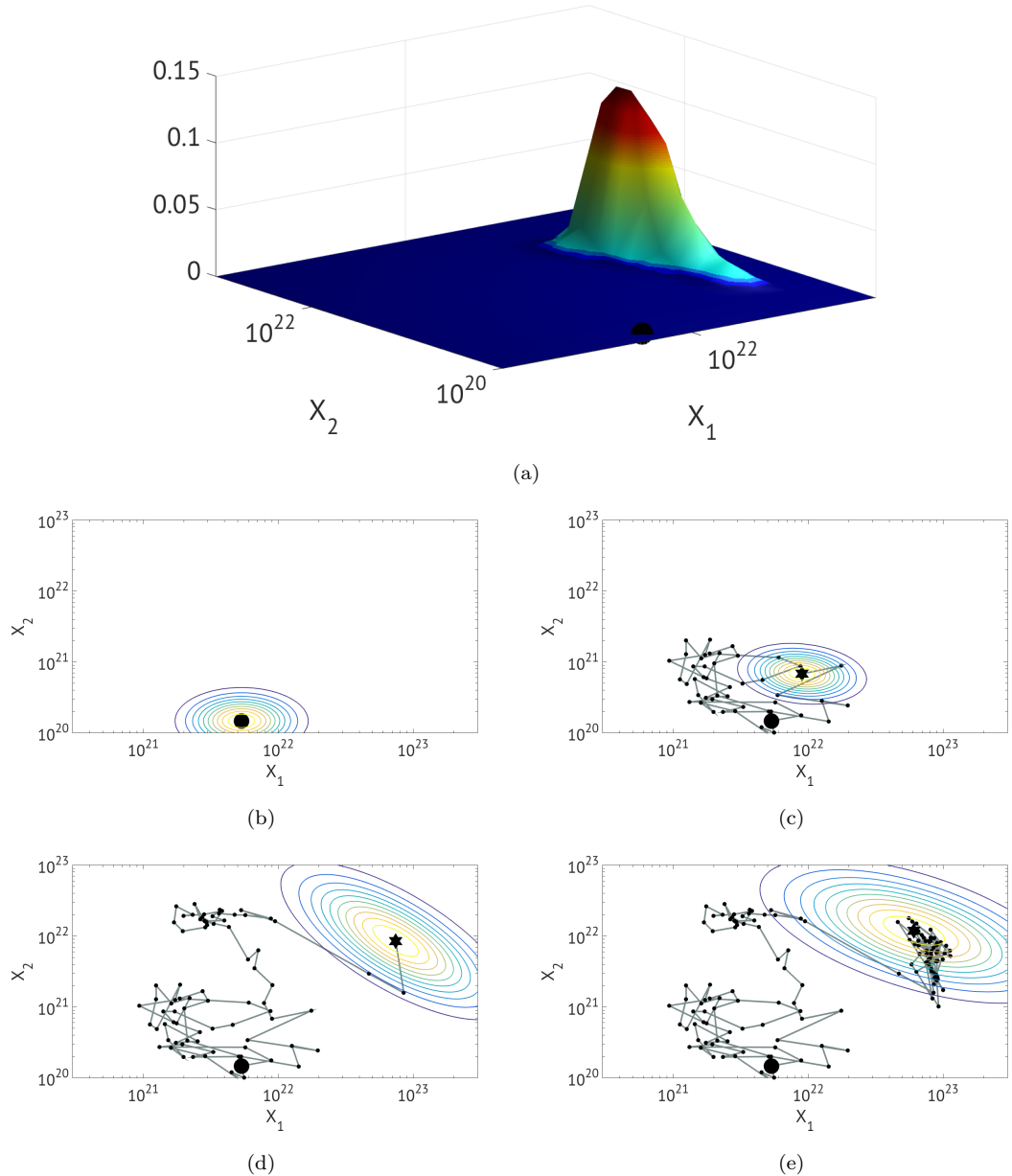


FIGURE 4.10: *Adaptive Method: A MCMC is started from the black point for sampling the target distribution in (a). The resulting chain and the current proposal distribution (level lines) are shown at four computational times: at the first point (b), at an instant right after the end of the non-adaptation period (c) (note that the covariance matrix is almost diagonal), and at two successive instants (d and e).*

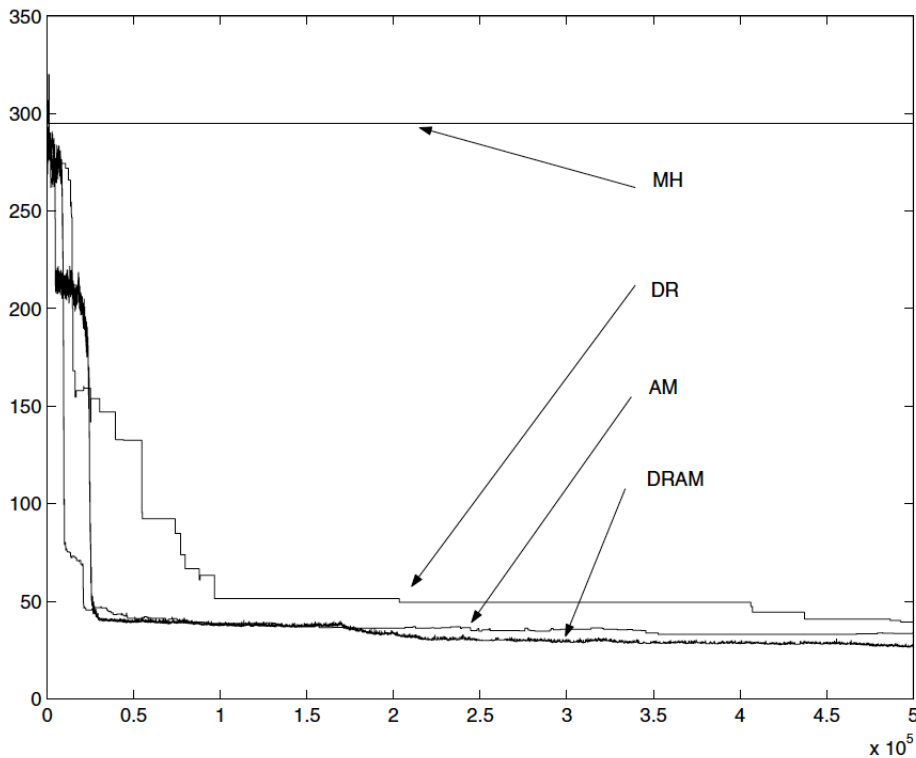


FIGURE 4.11: *Convergence of chain by MH, DR, AM and DRAM, from a case of study in Haario et al.'s paper [39]. The sum of the residual squares between data and output is plotted against simulation time*

distribution, the local shape of the distribution is different from its global aspect. The intuition of Haario *et al.*, proposed in their more recent paper [39], was to create a compromise between these two approaches by combining them into a single method, the DRAM. It is possible to couple the two Algorithms in practice through the following two steps:

- At the first stage of DR a covariance matrix  $\mathbf{Q}_t$  is generated from the previous draws of the chain.
- At the later stages of DR (in the event in which  $i_{DR} \leq n_{DR}$  and such that  $\mathbf{Q}_t^{i_{DR}-1}$  proposed some value that has not been accepted)  $\mathbf{Q}_t^{i_{DR}}$  is computed as a scaled version of the proposal at the first stage:  $\mathbf{Q}_t^{i_{DR}} = \mathbf{Q}_t / (\omega_{DR})^{i_{DR}-1}$ .

The advantages of this hybrid method compared to the single DR and AM and to the original MH is summarized in the Figure captured from Haario's paper (Fig. 4.11), that shows the convergence properties of these sampling strategies for a particular case of study proposed in the same article.

## 4.5 Validation

We have shown that a Delayed Rejection Adaptive Method applied to the Markov Chain Monte Carlo sampling can provide a solution to the Calibration inverse problem in terms of a probability distribution defined above the parameter and hyperparameter space  $S = \{\boldsymbol{\theta}; \boldsymbol{\alpha}\}$ . Through the marginalization of such PDF over each of the parameters, is then possible to find the probability that a particular value of  $\theta_i$  or  $\alpha_i$  produces an observable output  $\mathbf{y}$  equal to the data  $\mathbf{D}$ . Moreover, thanks to the stochastic representation that has been used for characterizing the structural inadequacy and thanks to the fact that such stochastic modeling has been moved upstream, we are able in this way to propagate the parameter uncertainty to the quantities of interest  $\mathbf{q}$ .

Unfortunately, the calibration process is only able to guarantee that the parameters are learning as much as possible from the data; however, this could be not enough: we have to explicitly check that the calibrated model is able to replicate the experiment with acceptable discrepancies. In case any of the available data is not a probable outcome, we can assess that such model is not capable of making reliable predictions with that particular scenario condition.

At this point, it is clearly imperative to define a proper metric for establishing when the discrepancy between output and data can be considered acceptable. For this purpose, Oliver *et al.* [24] suggested to use the Highest Posterior Density (HPD) credibility regions.

A  $\beta - HPD$  credible region is defined as “the set for which the probability of belonging to  $S$  is  $\beta$  and the probability density for each point in  $S$  is greater than that of the points outside  $S$ ”. That is:

$$\beta = \int_S p(\mathbf{y} | \mathbf{D}, \mathbf{M}) d\mathbf{y}, \quad \text{where } S = \left\{ \mathbf{y} : p(\mathbf{y} | \mathbf{D}, \mathbf{M}) \geq p(\mathbf{Y} | \mathbf{D}, \mathbf{M}) \right\}. \quad (4.21)$$

where  $\mathbf{Y}$  is a particular value from the outcomes.

For example, if we want to compute the High Density Posterior credibility regions with a  $\beta = 50\%$  for the probability density shown in Fig. 4.12, we draw an horizontal line extended for the entire domain and tangent to such PDF at its maximum. Then, we start to pull down the horizontal line until the area under the function and between the points in which it intersects the PDF is equal to  $\beta$ . The intervals  $(Y_1, Y_2)$  and  $(Y_3, Y_4)$  will be our  $50\% - HPD$  region.

Assume that we solved our calibration problem and we computed the posterior distribution for all the important parameters and hyperparameters. Moreover, say that we already propagated such uncertainty to the observable quantities by solving  $n$  direct problems using the  $n$  sets of parameters of the Markov chain that we computed during

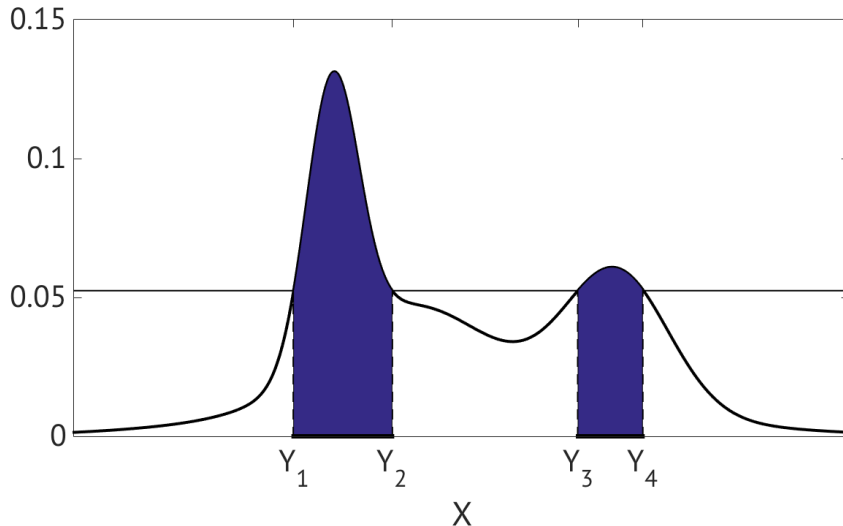


FIGURE 4.12: 50% – HPD regions (area in blue) for the PDF in black.

the calibration process. Thus, we have a posterior distribution for the observable quantities,  $\Pi(\mathbf{y})$ .

We now want to validate our model; in other words, we want to show that the  $\mathbf{y}$  that we obtained are good predictions of the data  $\mathcal{D}$ . We can thus use the Highest Posterior Density credibility region in their reverse sense: instead of fixing  $\beta$  and computing the HPD intervals, we can fix the intervals to contain the data and to be at the same time as smallest as possible and we can than compute the interval probability  $\beta$ .

If we define a parameter  $\chi$  to be:

$$\chi = 1 - \beta, \quad (4.22)$$

when  $\chi = 1$  the most probable model output coincides with the data. On the other hand,  $\chi = 0$  means that the model is unable to produce the data as outcome. Thus we can set a reasonable tolerance  $\bar{\chi}$ , so that if  $\chi < \bar{\chi}$  the data cannot be considered a probable outcome and the model is invalidated.

The fact that the model has not failed the validation process does not guarantee by itself that such model is capable of making reliable prediction. For example, as already mentioned in the previous Sections, one has to be sure that the stochastic model that has been created for representing the structural inadequacy is upstream enough and that it is capable of affecting the QoIs' computation. Such dependency can easily be proven assessing the sensitivity of the quantity of interest with respect to the hyperparameters.

## 4.6 SMUQ: Stochastic Modeling for Uncertainty Quantification

Reached the stage of delineating a proper way for quantifying the uncertainty and validating the model, the author of this thesis implemented all the methodology described in this chapter in a single FORTRAN library, that at a later time has been named Stochastic Modeling Uncertainty Quantification (SMUQ).

Initially, writing *ex novo* a UQ code was merely for educational purposes. Indeed, a significant number of UQ softwares has been released in the last years by authoritative Departments, Institutions and Agencies (e.g., DAKOTA by Sandia National Laboratories [41] and UQTools by NASA [42]). Moreover, some of them (e.g., QUESO by the PECOS Center, University of Texas at Austin [25]) are based on methodologies similar to the ones that has been presented in this chapter. On the other hand, a mechanical use of an already packed tool would have likely meant losing sight at the physical essence of the problem to solve. This could have been particularly dangerous for the approach to the validation problem that we are going to use, due to the fact that the stochastic representation of the model inadequacy has to be based on strong physical reasons.

Once that the first results started to come out, however, SMUQ showed to perform well, also compared to the other softwares: it has been able to reproduce the results obtained through different UQ codes and it also turned out to be very user-friendly in solving a wide range of UQ problems. This is due to the fact that SMUQ treats the external model as a black box, as it will be explained in the next lines.

Although a complete description of the implemented code's operating principles is not one of the aims of this thesis, it is useful to point out some of its key-ideas and features, in order to give a better understanding of the results proposed in the next chapters.

The main goal of such code is to compute the necessary quantities for quantifying the uncertainty and validating the model. Whith this ambition, one should have in mind what suggested by Tarantola in his book: “This is essentially what must be proposed: to look at a large number of randomly generated models (first, of the prior distribution, and then, of the posterior distribution) in order to intuitevely apprend the basic properties of the probability distribution, followed by calculation of the probabilities of all interesting events. Sometimes, it may nevertheless be necessary to estimate some moments (mean, covariance, etc.) of distribution. Of course, they can also be evaluated using the samples.” [31]. For this reason, SMUQ provides in outputs quantities like the posterior distribution of the parameters and hyperparameters  $\Pi(\boldsymbol{\theta}, \boldsymbol{\alpha} | \mathcal{D}, \mathcal{M})$ , the posterior distribution of the observable quantities  $\Pi(\mathbf{y} | \mathcal{D}, \mathcal{M})$  and the probabilties connected to the High Posterior Density regions  $\chi$ .

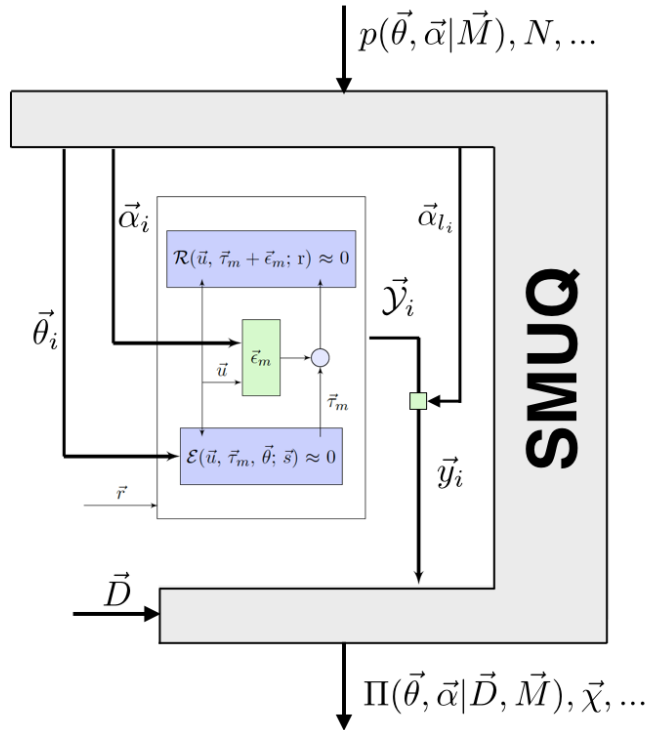


FIGURE 4.13: *Schematic representation of SMUQ’s working strategy in solving the Calibration and Validation processes: once the input parameters for the Bayesian Inference, for the Markov Chain and for the Delayed Rejection Adaptive Method are specified, SMUQ is able to quantify the model uncertainty and to establish the reliability of the model predictions taking advantage of the available data  $\mathbf{D}$ .*

As it has already been explained, the code is based on Bayesian Inference for solving the inverse problem and it generates a Markov chain by means of a Delayed Rejection Adaptive Method applied to the Metropolis-Hasting Algorithm. Therefore, SMUQ requires that all the functions and all the parameters associated with such composition of methodologies have been specified. These functions and parameters will thus represent the inputs of the code.

For this to be clarified, we will briefly describe SMUQ’s working strategy, that is represented schematically in Fig. 4.13. Assuming that a data  $\mathbf{D}$  is available and the scenario inputs  $r$  for the external model have been specified, SMUQ computes recursively the observable quantities  $\mathbf{y}_i$  through the external model; at each of the iterations, however, the values of the parameters  $\boldsymbol{\theta}_i$  and of the hyperparameters  $\boldsymbol{\alpha}_i$  have been properly changed by the DRAM process. This repeated mechanism produces a Markov chain  $\{(\boldsymbol{\theta}, \boldsymbol{\alpha})_1, (\boldsymbol{\theta}, \boldsymbol{\alpha})_2, \dots, (\boldsymbol{\theta}, \boldsymbol{\alpha})_{N_{MC}}\}$ , where the length of chain  $n_{MC}$  must have been specified in the SMUQ’s input, and such succession is a set of samples of the parameters posteriors.

SMUQ is capable of running in parallel on different processors and this is made possible

by creating a different recursive process on each of the computer cores. Each of this processes generates a different chain and the final total set of samplings, then, will be a collage of such successions. The advantages of this feature are crucial: the parallelization reduces considerably the computational time, permits to reduce the autocorrelation of the total chain and allows to explore deeply and faster the entire parameters space. This last point is due to the fact that all the processors receive the same initial inputs, except for the chain initial points (Subsec. 4.4.3); each of the processors, indeed, produces a first draw by means of an independent sample of the prior distribution. This requires to provide a proper representation of such PDF, based on the knowledge available about the parameters.

For example, if the only information that we have about a particular  $\theta_i$  (or about a particular  $\alpha_j$ ) is the range in which it is restricted to vary, then the box function can be a good description of the prior:

$$p(\theta_i | \mathbf{M}) = \begin{cases} 1, & \text{if } \theta_i \in (\theta_{\min_i}, \theta_{\max_i}), \\ 0, & \text{otherwise} \end{cases} \quad \forall i \leq T \quad (4.23)$$

or

$$p(\alpha_j | \mathbf{M}) = \begin{cases} 1, & \text{if } \alpha_j \in (\alpha_{\min_j}, \alpha_{\max_j}), \\ 0, & \text{otherwise.} \end{cases} \quad \forall j \leq A \quad (4.24)$$

In other cases, a normal distribution can be more appropriate:

$$p(\theta_i | \mathbf{M}) \propto \exp \left( -\frac{1}{2} \left( \frac{\theta_i - \mu_{\theta_i}}{\sigma_{\theta_i}} \right)^2 \right) \quad (4.25)$$

or

$$p(\alpha_j | \mathbf{M}) \propto \exp \left( -\frac{1}{2} \left( \frac{\alpha_j - \mu_{\alpha_j}}{\sigma_{\alpha_j}} \right)^2 \right) \quad (4.26)$$

Sometimes, nonetheless, a combination of the former and the latter PDFs is the best choice and the prior must be chosen to be a Gaussian function in which the tails are cut off.

All these probability distributions have been implemented in SMUQ. Once one specifies for each of the parameters and hyperparameters the shape of the distribution, the ranges of variation in case of box function and the mean and the standard the distribution in case of a Gaussian, SMUQ samples the priors and produces the initial point for each of the processors. Moreover, under the assumption of uncorrelation between the PDFs in Eq.s 4.23 - 4.26, the code computes the values of the joint priors at such starting points, as in Eq. 4.11.

The next step is obtaining the posterior at  $(\boldsymbol{\theta}_1 \text{ and } \boldsymbol{\alpha}_1)$ . In order to do that, we have to define the proper representations for the likelihood. Following what suggested by

different autors [33] [35], a Gaussian function is an appropriate representation of the likelihood for a wide range of problems. Assume now that the data is available in  $N_D$  different points and that, in the same nodes, we computed the model outputs; we can write:

$$l(\mathbf{y} = \mathbf{D} \mid \boldsymbol{\theta}, \boldsymbol{\gamma}, \mathbf{M}) = \frac{1}{\sqrt{2\pi\sigma_l^2}} \exp\left(-\frac{1}{2} \sum_{k=1}^{N_D} \left(\frac{y_k - D_k}{\sigma_l}\right)^2\right) \quad (4.27)$$

At this point, it is possible to compute the likelihood  $L(\mathbf{y} = \mathbf{D} \mid \boldsymbol{\theta}, \boldsymbol{\alpha}, \mathbf{M})$  as shown in Eq. 4.12; the integration can be realized by means of a Montecarlo integration [43]:

$$\begin{aligned} L(\mathbf{y} = \mathbf{D} \mid \boldsymbol{\theta}, \boldsymbol{\alpha}, \mathbf{M}) &= \int_{-\infty}^{+\infty} l(\mathbf{y} = \mathbf{D} \mid \boldsymbol{\theta}, \boldsymbol{\gamma}, \mathbf{M}) \times \prod_{k=1}^p f(\gamma_k \mid \alpha_{1k}, \dots, \alpha_{nk}, \mathbf{M}) d\boldsymbol{\gamma} = \\ &= \int_{-\infty}^{+\infty} l(\mathbf{y} = \mathbf{D} \mid \boldsymbol{\theta}, \boldsymbol{\gamma}, \mathbf{M}) g(\boldsymbol{\gamma}) d\boldsymbol{\gamma} = \\ &= \mathbf{E}_{g(\boldsymbol{\gamma})} \left[ l(\mathbf{y} = \mathbf{D} \mid \boldsymbol{\theta}, \boldsymbol{\gamma}, \mathbf{M}) \right] = \\ &\approx \sum_{z=1}^G \frac{l(\mathbf{y} = \mathbf{D} \mid \boldsymbol{\theta}, \bar{\boldsymbol{\gamma}}_z \mathbf{M})}{N_\gamma} \end{aligned}$$

where  $\bar{\boldsymbol{\gamma}}_z$  represent a value of the vector  $\boldsymbol{\gamma}$  obtained by sampling the probability distribution  $g(\boldsymbol{\gamma}) = \prod_{k=1}^p f(\gamma_k \mid \alpha_{1k}, \dots, \alpha_{nk}, \mathbf{M})$  with one of the G different draws. From such equation it is clear that SMUQ needs the standard deviation  $\sigma_l$ , the probability  $g(\boldsymbol{\gamma})$  and the number of draws G to be specified in order to compute the value of likelihood at some generic  $\boldsymbol{\theta}_i$  and  $\boldsymbol{\alpha}_i$ , given a data  $\mathbf{D}$ .

Once the values of the prior and of the likelihood have been obtained, with a simple multiplication it is possible to find the posterior distribution  $\Pi(\boldsymbol{\theta}_1, \boldsymbol{\alpha}_1 \mid \mathbf{D}, \mathbf{M})$ .

At this point, a candidate set of values for the parameters and for the hyperparameters is computed by means of a proposal PDF. Such distribution can be represented at this step by a multi-dimensional Gaussian function with a mean  $\boldsymbol{\mu}_q$  and a diagonal covariance matrix  $\mathbf{Q} = \text{diag}(\sigma_{q1}, \sigma_{q2}, \dots, \sigma_{qT}, \sigma_{qT+1}, \dots, \sigma_{qT+A})$ . With the same procedure explained above, it is possible to determine the value of the posterior at  $\boldsymbol{\theta}^*, \boldsymbol{\alpha}^*$ .

Following the steps of the Metropolis-Hasting Algorithm, the ratio

$$\alpha_1 = \frac{\Pi(\boldsymbol{\theta}^*, \boldsymbol{\alpha}^* \mid \mathbf{D}, \mathbf{M})}{\Pi(\boldsymbol{\theta}_1, \boldsymbol{\alpha}_1 \mid \mathbf{D}, \mathbf{M})} \quad (4.28)$$

will establish if the set  $\boldsymbol{\theta}^*, \boldsymbol{\alpha}^*$  will be a new point of the Markov chain. In the case such set is rejected there are two possibilities: if SMUQ is set to use a DR method (i.e: if  $n_{DR} > 1$ ), new  $\boldsymbol{\theta}^*, \boldsymbol{\alpha}^*$  will be generated by a  $\mathbf{Q}' = \mathbf{Q}/\omega_{DR}$ ; otherwise, the chain will not move from the first point and  $\boldsymbol{\theta}_2 = \boldsymbol{\theta}_1, \boldsymbol{\alpha}_2 = \boldsymbol{\alpha}_1$ .

If one defined  $n_{MC}$  to be the length of the Markov chain, SMUQ will repeat the process

described above  $n_{MC}$  times in order to sample the posterior distribution of the parameters. In other words, the software will run the external code in a loop of  $(n_{MC} \times G)$  repetitions, changing every time the model parameters and hyperparameters and eventually modifying the proposal covariance matrix  $\mathbf{Q}$  by means of the Adaptive Method. Once the posterior distribution of the parameters has been defined, the model uncertainty is quantified. Moreover, while SMUQ repeats such process, it also stores the outputs  $\mathbf{y}_i$ . Such vectors represent a sample of the observable quantities' posterior distribution and they are used to compute the probabilities  $\chi$  connected to the High Posterior Density regions by means of Eq.s 4.21 and 4.22.

Chap. 6 will present the results of the application of SMUQ to a particular uncertainty quantification problem and that will be useful for better clarifying the code working strategy and its potential.



# Chapter 5

## Stochastic Modeling of the Electronic States Populations

The aim of this chapter is to present a strategy for the application of the validation approach proposed by Oliver *et al* (see Subsec. 4.2.2 of the previous chapter) to the problem of the radiative quantities computation. As discussed in the paper of Miki *et al* [14], considering the error generated by the Radiative Model being relatively small compared to the uncertainties produced by the flow solver and affecting the plasma quantities (e.g., Temperatures and Populations of the Energy States) is a reasonable assumption; such approximation is justified by the upstream collocation of the flow solver and by the simplified character of the Multi-Temperature description, which such numerical model relies on. With this in mind, one can see a strong connection between the flow solver in Fig. 2.3, Sec. 2.6, and the embedded model in Fig. 4.3, Subsec. 4.2.2, as well as between the radiative solver and the reliable model, respectively in the same two pictures. The idea of adding a stochastic source term of uncertainty in between the two solvers comes then straightforward (Fig. 5.1).

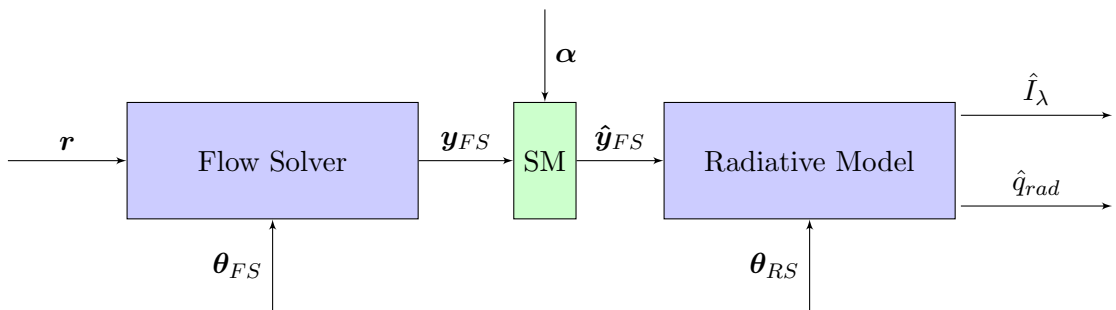


FIGURE 5.1: *Introduction of a stochastic model between the Flow Solver and the Radiative Model. Such term upgrades 2.3 in order to apply the approach discussed in Subsec. 4.2.2 to a reliable prediction of the radiative heat flux  $\hat{q}_{rad}$ .*

For the reasons pointed out in the previous chapter, a physically based attribute is a

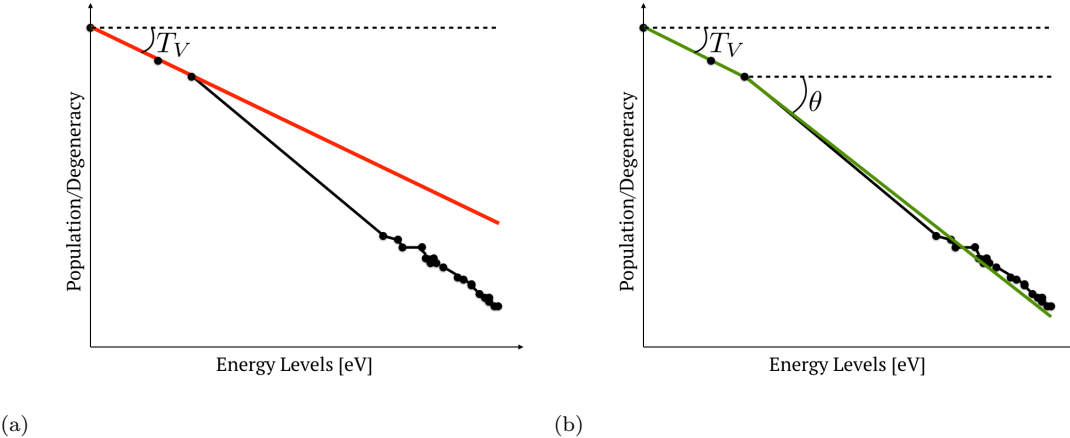


FIGURE 5.2: *Comparison between the Populations of the Electronic States obtained in a region close to the shock by means of a Collisional Radiative model (black points), a Multi-Temperature model (red line) (a) and a Stochastic Multi-Temperature (blue lines) (b).*

required feature for such stochastic representation in order to assure the consistency of the validation process. The approach proposed here, thus, formulates the uncertainty source upon the intuition that the discrepancy between predictions and experimental data is due to the assumption of equilibrium for the population of the energy levels when computing the radiation emitted by the gas; indeed, as it has already been discussed, the Multi-Temperature model under analysis separates the total energy of the particles into the contributions of each of the modes, which are assumed to be distributed according to the Maxwell-Boltzmann equation (Eq. 2.2) with different characteristic temperatures: one,  $T$ , for the translational and rotational states, and another,  $T_V$  for the vibrational and electronic levels. The vibrational-electronic temperature, after having been strongly perturbed by the bow shock, eventually adjusts to the roto-translational value following a thermo-relaxation process described by the Landau-Teller model (Eq. 2.23); in this way, all the modes will be in equilibrium at the same temperature  $T$  at a certain distance from the shock. The slower the chemical processes (compared to the fluid characteristic time), the greater the distance.

However, in strong non-equilibrium scenarios the populations of the high-energy levels are generally characterized by higher frequency dynamics compared to the low-energy ones; for this reason, they easily depart from the equilibrium distributions (Fig. 5.2(a)) and in such case the Boltzmann-based Multi-Temperature fails in capturing their spatial evolutions. In turn, inaccurate computations of the electronic energy states populations will generate erroneous estimates of the number of transitions between the levels and, lastly, not reliable predictions of the heat flux, due to the fact that this last quantity is dominated by the atomic line radiation (see Sec. 2.6). A more realistic functional form for representing the transient response of the high-energy electronic populations to the

perturbation induced by the bow shock is thus required.

One of the simplest ways for describing such non-equilibrium effect is considering the high-energy levels in equilibrium with each other at a temperature  $\theta$ , different from  $T_V$ . One can express the dynamic of also this new variable through a Landau-Teller relaxation; differently from the first order equation used for describing the evolution of the vibrational energy mode, however, this one will present the vibrational-electronic temperature as the reference quantity:

$$\dot{\theta} = \frac{T_V - \theta}{\tau}. \quad (5.1)$$

Here,  $\tau$  is a new stochastic constant and its values are normally distributed,  $\tau = \mathcal{N}(\mu_\tau, \sigma_\tau)$ ; the hyperparameters  $\mu_\tau$  and  $\sigma_\tau$  correspond to  $\alpha$  in Fig. 5.1 and can be calibrated through the procedure presented in the previous chapter.

From a couple of values of  $\mu_\tau$  and  $\sigma_\tau$  one can generate a time constant  $\tau$ , solve the Ordinary Differential Equation 5.1 and with the temperature  $\theta$  so found compute the populations of the high-energy electronic states through the Maxwell-Boltzmann equation.



# Chapter 6

## Results

### 6.1 Introduction

By means of the code SMUQ, both the approaches discussed in Sec. 4.2 have been applied to the validation of Park’s TTv model, as represented in Fig. 6.1(a) for Kennedy and O’Hagan’s strategy and in Fig. 6.1(b) for the method of Olivier *et al.*; the terms that appear in such figures will be outlined in this introduction, while the results of the validation process be presented in the rest of the chapter.

The plasma under analysis is *Nitrogen5*, a mixture made up of five chemical components:  $N$ ,  $N^+$ ,  $N_2$ ,  $N_{2+}$  and  $e^-$ ; the related reactions that will occur in the plasma are listed in 6.1. The choice of such mixture allows to deal with few species and, at the same time, to capture some features of more complex set of species, such as *Air11*. For example, Miki *et al.* have shown that the nitrogen ionization process is one of the key phenomena also in the air thermal-relaxation [14].

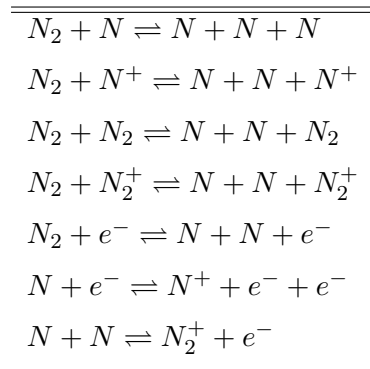


TABLE 6.1: *Occurring Reactions*.

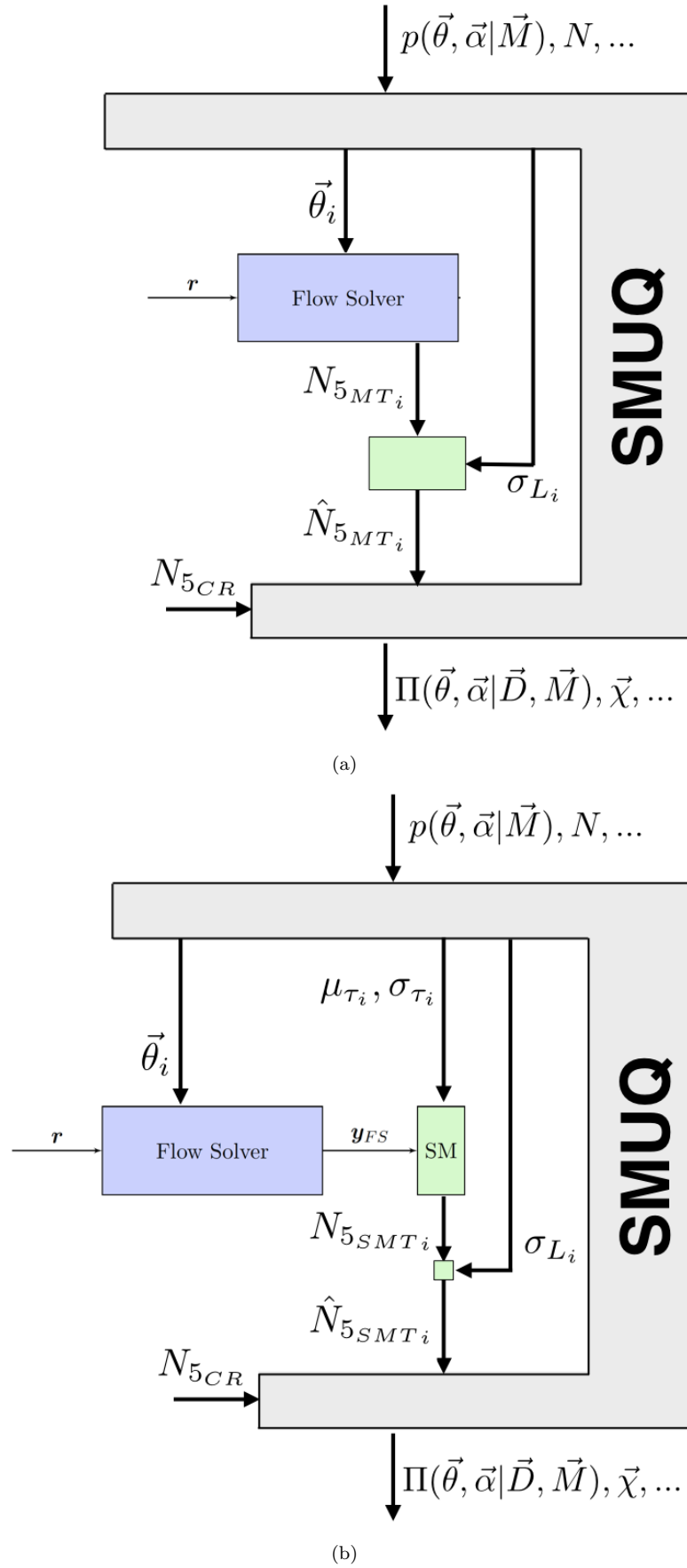


FIGURE 6.1: Application of the two approaches discussed in Sec. 4.2 (Kennedy and O'Hagan's strategy (a) and the method of Olivier et al. (b)) to the problem of validating the Park's TTv model predictions of the Population of the Nitrogen 5th Electronic Level.

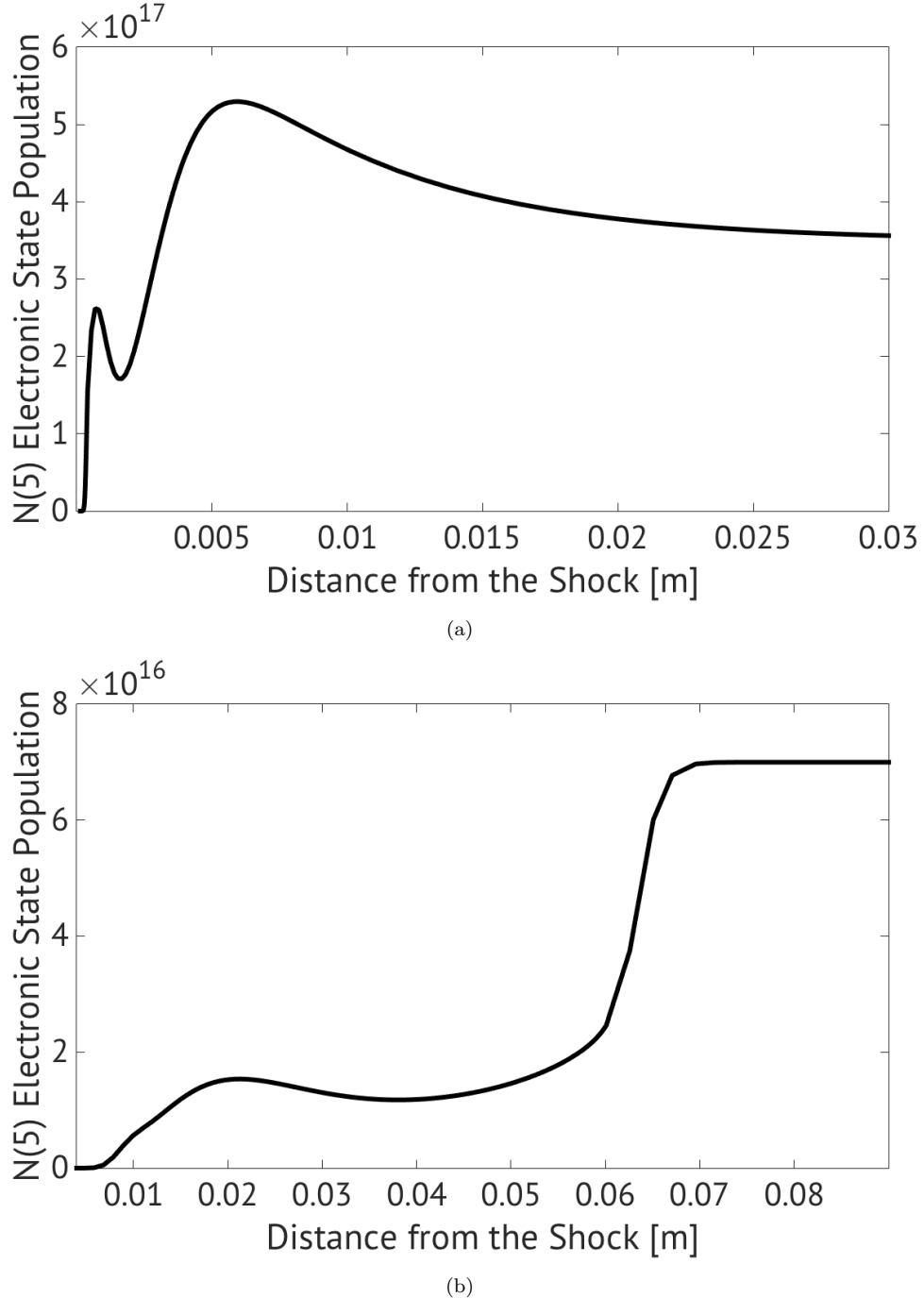


FIGURE 6.2: *Collisional Radiative Solution for the Population of Nitrogen 5th Electronic State in the first scenario,  $P_0 = 39.9\text{Pa}$ ,  $T_0 = 195\text{K}$  and  $u_0 = 10340\text{m/s}$  (a), and in the second one,  $P_0 = 2\text{Pa}$ ,  $T_0 = 195\text{K}$  and  $u_0 = 13360\text{m/s}$  (b).*

As it has been pointed out in Sec. 4.6, the UQ solver working strategy is based on iterated calls of the numerical model under investigation; its computational cost, therefore, grows almost linearly with the computational time required by the sum of the flow solver, the stochastic model and the radiative solver. This last one, in particular, is by far

	Scenario 1	Scenario 2
Pressure	$39.9 Pa$	$2.0 Pa$
Temperature	$195.0 K$	$195.0 K$
Velocity	$10340 m/s$	$13360 m/s$

TABLE 6.2: *Inflow Conditions.*

the most expensive of the three steps. In order to attest the validity of the Multi-Temperature model avoiding, at the same time, such computational effort, the author of this work decided to treat as observable quantity directly the population of the 5th of the Nitrogen electronic levels ( $N_{5_{MT}}$  or  $N_{5_{SMT}}$ ), instead of the radiative intensity as Miki *et al.* have done in their paper [14]. Indeed, even if direct measures of such populations are not realistic, one can always compare such outcomes with the values predicted by the Collisional Radiative model ( $N_{5_{CR}}$ ), which are by far more realistic [8]. The choice of the 5th of the electronic levels is related to the fact that the transition between such state and the ground state generates the atomic line that influences most the radiation experienced by a non-equilibrium air mixture [14]. Therefore, a good prediction of the 5th electronic level is eventually required if one wants to compute the heat flux for earth atmospheric re-entry. Thanks to this simplification, the radiative model can be neglected from the problem.

The green rectangles in Fig. 6.1 represent the stochastic models. The “SM” in (b) is the one physics-based and characterized by the hyperparameters  $\mu_{\tau_i}$  and  $\sigma_{\tau_i}$ , that SMUQ will calibrate; on the other hand, the two nameless rectangles in (a) and in (b) indicate the multiplicative error formulated through the Gaussian form of the likelihood. Their standard deviations  $\sigma_{L_i}$  will be calibrated by the code as well. Due to the fact that the approach (b) moved the most part of the model inadequacy to the “SM” contribute, we should expect from Kennedy and O’Hagan’s likelihood a larger calibrated standard deviation; for this reason the corresponding rectangle appears bigger than the nameless one in (b).

The two scenario conditions analyzed in this work present the same inflow characteristic quantities (i.e., vectors  $\mathbf{r}$  in Fig. 6.1) that characterized two of the trajectory points of the FIRE II test-case, a flight experiment from the 1960s that had the objective of determining the radiative heating environment experienced by a large-scale Apollo vehicle during high speed re-entry. The same scenarios have been also studied by Miki *et al.* for validating the non-equilibrium flow model [14]; thus, even if they accomplished this goal for a Air11 mixture, such parallelism will permit to compare some of the results of this work with the outcomes of their paper. The inflow pressure, temperature and velocity are listed in Tab. 6.2, while the Populations of the Nitrogen 5th Electronic Level computed by means of the Collisional Radiative model are shown Fig. 6.2 for

Model Parameter		Model	Reference Value	Variability
Arrhenius Pre-exponential Coefficient	$A_{N_2+N}$	Arrhenius	$3 \cdot 10^{22}$	$\pm 1$ order
Arrhenius Pre-exponential Coefficient	$A_{N_2+N^+}$	Arrhenius	$3 \cdot 10^{22}$	$\pm 1$ order
Arrhenius Pre-exponential Coefficient	$A_{N_2+N_2}$	Arrhenius	$7 \cdot 10^{22}$	$\pm 1$ order
Arrhenius Pre-exponential Coefficient	$A_{N_2+N_2^+}$	Arrhenius	$7 \cdot 10^{22}$	$\pm 1$ order
Arrhenius Pre-exponential Coefficient	$A_{N_2+e^-}$	Arrhenius	$1.2 \cdot 10^{25}$	$\pm 1$ order
Arrhenius Pre-exponential Coefficient	$A_{N+e^-}$	Arrhenius	$2.5 \cdot 10^{34}$	$\pm 1$ order
Arrhenius Pre-exponential Coefficient	$A_{N+N}$	Arrhenius	$4.4 \cdot 10^7$	$\pm 1$ order
Limiting Cross Section VT	$\sigma_C$	Park [7]	$3 \cdot 10^{-21}$	$\pm 1$ order
Dissociation Energy Removal	$C_{N_2}$	Gnoffo [4]	0.3	[0, 1]
Electron Energy Removal	$I_e$	Johston [19]	$4.05 \cdot 10^8$	$\pm 1$ order

TABLE 6.3: *Model Parameters and their variabilities.*

Stochastic Model Hyperparameter		Reference Value	Variability
Mean of the Relaxation Time Constant Exponent	$-\mu_{\log(\tau)}$	-	[6, 13]
SD of the Relaxation Time Constant Exponent	$\sigma_{\log(\tau)}$	-	$[10^{-4}, 10^{-1}]$

TABLE 6.4: *Stochastic Model Hyperparameters and their variabilities.*

both these two scenario cases.

Based on previous studies [28] [26] [14], the model parameters reported in Tab. 6.3 are, at the same time, vitally important for the computation of the electronic levels populations and strongly affected by uncertainty; for this reason they have been selected for the calibration process also in this work. Tab. 6.3 also reports the parameters reference values from literature and the related ranges of uncertainties. On the other hand, in Tab. 6.4 the reasonable ranges for the stochastic model hyperparameters have been reported. Due to the lack of knowledge in regard to their true values, such intervals have been chosen to be less conservative as possible. It should be noticed from the table that the actual parameter that has been stochastically represented is the absolute value of the time constant for the relaxation of the high-energy electronic states, instead of the time constant itself.

## 6.2 Sensitivity Analysis and Models Reductions

Before starting the process of calibration, the sensitivity of the quantity of interest has been investigated with respect to the model parameters (and to the hyperparameters in the case of stochastic Multi-Temperature). This has been done with the aim of reducing the complexity of the problem by discarding the unessential parameters, as Sec. 6.2 motivated.

Through the sensitivity analysis library implemented in SMUQ, the parameters and hyperparameters space (represented in Tab.s 6.3 and 6.4 by the variability intervals) has been swept: 100000 drawings have been sampled by means of a Monte Carlo method. These sets of parameters have been propagated through both the Multi-Temperature and the Stochastic Multi-Temperature Models; in this way, the population of the Nitrogen 5th electronic level has been computed for each of the spatial points in front of shock. Such punctual outputs have been then related to the parameters they were generated from and the Pearson correlation coefficients have been computed:

$$\rho_{N_{5_j}, \theta_k} = \frac{E[(N_{5_j} - \mu_{N_{5_j}})(\theta_k - \mu_{\theta_k})]}{\sigma_{N_{5_j}} \sigma_{\theta_k}} \quad (6.1)$$

where  $N_{5_j}$  are all the values of the population computed at the j-th spatial point, characterized by a mean  $\mu_{N_{5_j}}$  and a standard deviation  $\sigma_{N_{5_j}}$ , and  $\theta_k$  are all the sampled values of the k-th parameter, characterized by a mean  $\mu_{\theta_k}$  and a standard deviation  $\sigma_{\theta_k}$ . In Subsec. 6.2.1, the correlation coefficients obtained from the Multi-Temperature model are plotted as function of the distance from the shock; in Subsec. 6.2.2 the same has been done for the Stochastic Multi-Temperature (SMT).

### 6.2.1 Multi-Temperature Model Sensitivity Analysis:

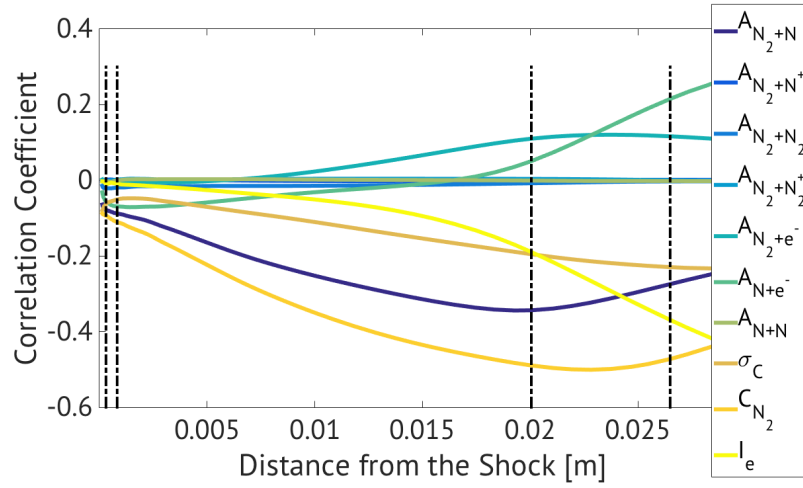
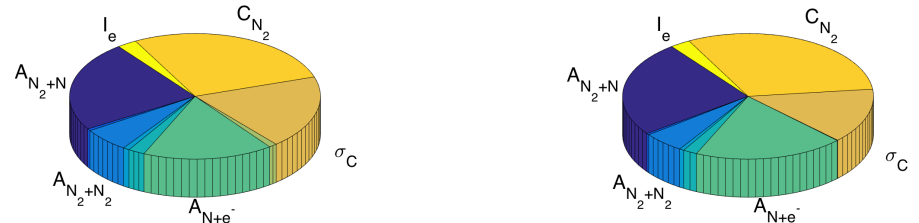
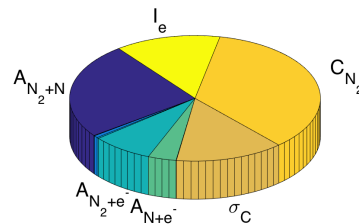


FIGURE 6.3: Scenario 1: Sensitivity of the Nitrogen 5th Electronic State Population to each of the MT Parameters in function of the distance from the shock.

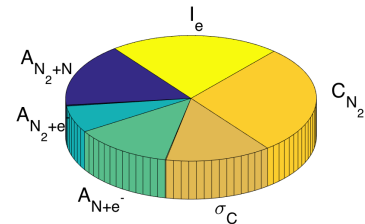


(a) Distance from the shock = 0.03cm

(b) Distance from the shock = 0.07cm



(c) Distance from the shock = 2cm



(d) Distance from the shock = 2.6cm

FIGURE 6.4: Scenario 1: Contribution of each of the MT Parameters to the Population of the Nitrogen 5th Electronic State. Sensitivity analyzed at three distances from the shock: 0.03cm (a), 0.07cm (b), 2cm (c) and 2.6cm (d).

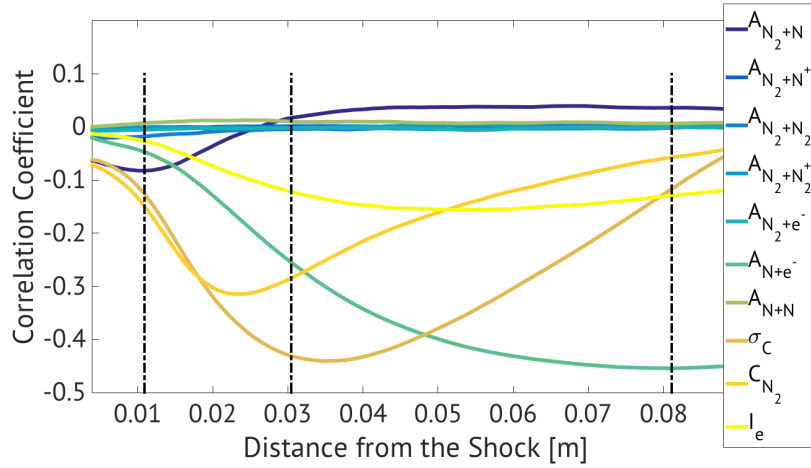


FIGURE 6.5: Scenario 2: Sensitivity of the Nitrogen 5th Electronic State Population to each of the MT Parameters in function of the distance from the shock.

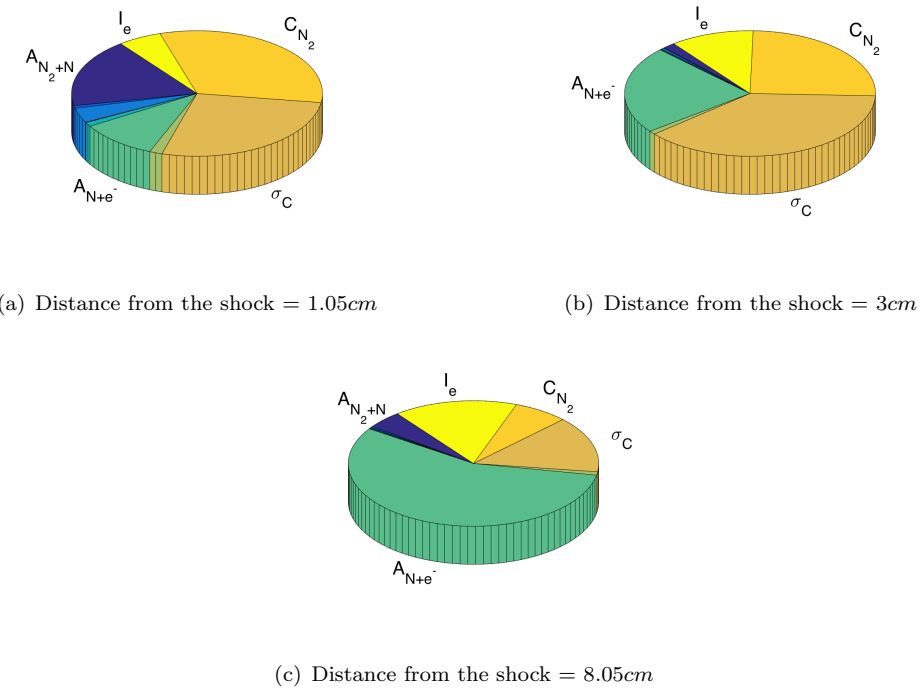


FIGURE 6.6: Scenario 2: Contribution of each of the MT Parameters to the Population of the Nitrogen 5th Electronic State. Sensitivity analyzed at three distances from the shock: 1.05cm (a), 3cm (b) and 8.05cm (c).

### 6.2.2 Stochastic MT Sensitivity Analysis:

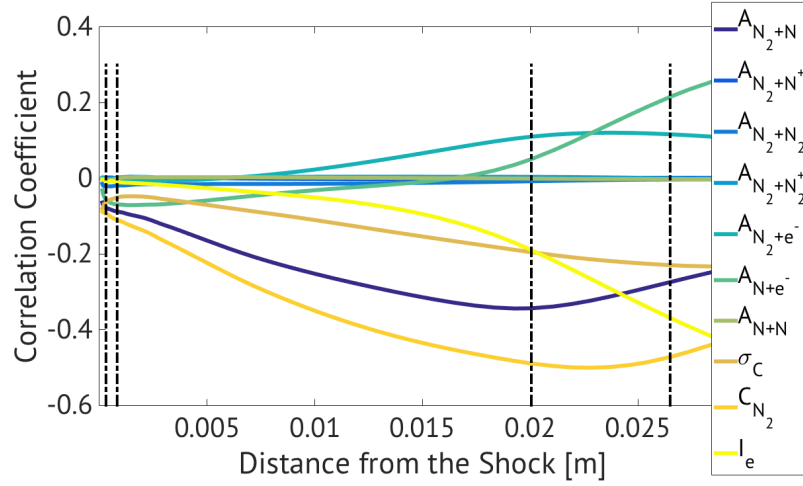


FIGURE 6.7: *Scenario 1: Sensitivity of the Nitrogen 5th Electronic Population to each of the Stochastic MT Parameters in function of the shock distance.*

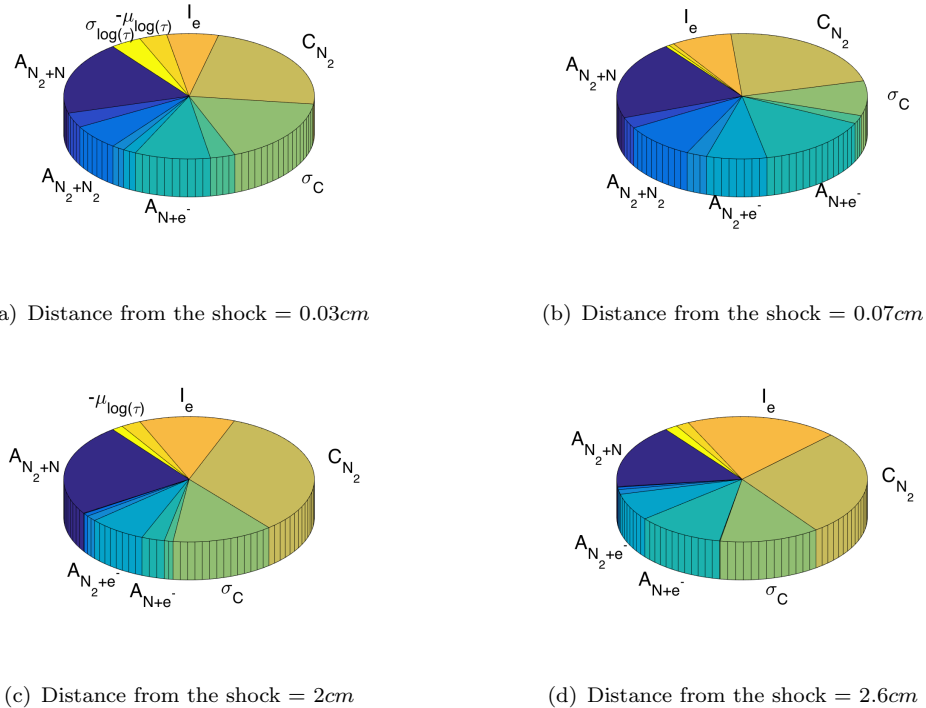


FIGURE 6.8: *Scenario 1: Contribution of each of the Stochastic MT Parameters to the Population of the Nitrogen 5th Electronic State. Sensitivity analyzed at three distances from the shock: 0.03cm (a), 0.07cm (b), 2cm (c) and 2.6cm (d).*

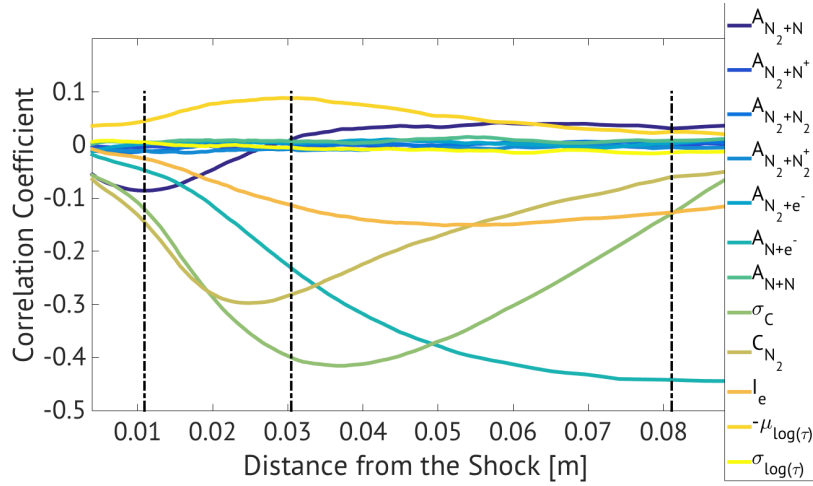


FIGURE 6.9: Scenario 2: Sensitivity of the Nitrogen 5th Electronic State Population to each of the Stochastic MT Parameters in function of the distance from the shock.

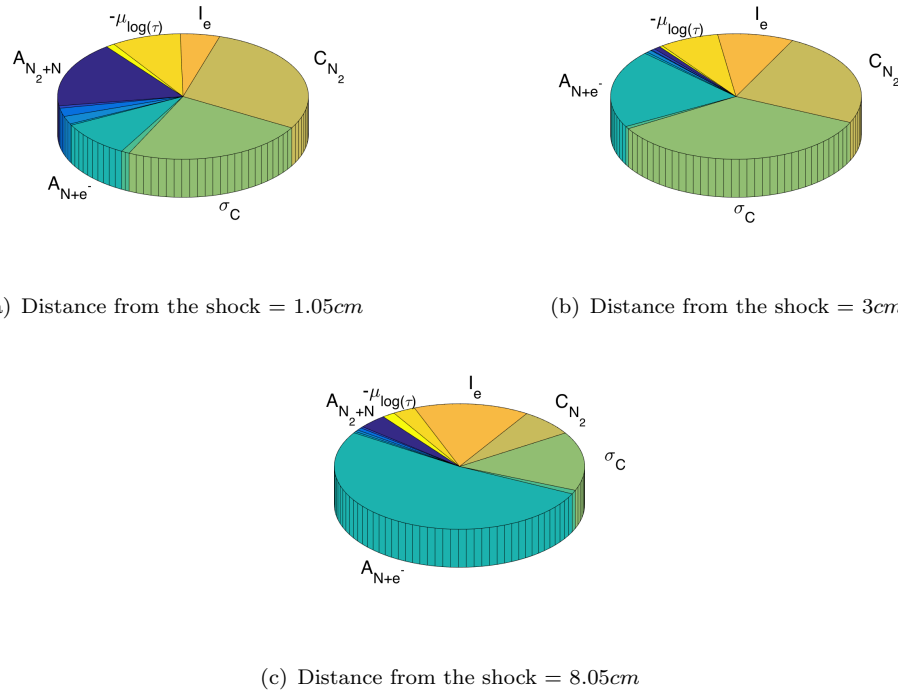


FIGURE 6.10: Scenario 2: Contribution of each of the Stochastic MT Parameters to the Population of the Nitrogen 5th Electronic Level. Sensitivity analyzed at three distances from the shock: 1.05cm (a), 3cm (b) and 8.05cm (c).

### 6.2.3 Model Reduction

The sensitivity analysis led to rank the parameters by importance as in Tab. 6.5. The results have shown good agreement with what found by Miki *et al.* The populations of the Nitrogen 5th Electronic State appear strongly dependent on the Nitrogen atoms ionization process and on the dissociation of  $N_2$  due to the collision with  $N$  and electrons, even if the magnitude of such feature is scenario dependent. Also the relaxation coefficients has primary importance in the QoI prediction.

On the other hand, the sensitivity analysis suggests that the hyperparameters have a secondary role. For the first scenario, in particular, the QoI seems to be depending on  $-\mu_{\log(\tau)}$  and  $\sigma_{\log(\tau)}$  only in the region very close to the shock. This fact could be related to the presence of strong non-equilibrium only in such area or to the extremely large interval that has been chosen for the hyperparameters variability. The calibration process will better clarify this aspect.

Based on this analysis, the Arrhenius pre-exponential coefficients  $A_{N_2+N^+}$ ,  $A_{N_2+N_2^+}$  and  $A_{N+N}$  are not taken into account in the rest of this work.

Scenario 1, MT	Scenario 2, MT	Scenario 1, SMT	Scenario 2, SMT
$C_{N_2}$	$A_{N+e^-}$	$C_{N_2}$	$A_{N+e^-}$
$A_{N_2+N}$	$\sigma_C$	$A_{N_2+N}$	$\sigma_C$
$\sigma_C$	$C_{N_2}$	$\sigma_C$	$C_{N_2}$
$I_e$	$I_e$	$I_e$	$I_e$
$A_{N+e^-}$	$A_{N_2+N}$	$A_{N+e^-}$	$-\mu_{\log(\tau)}$
$A_{N_2+N_2}$		$A_{N_2+N_2}$	$A_{N_2+N}$
$A_{N_2+e^-}$		$A_{N_2+e^-}$	
		$-\mu_{\log(\tau)}$	
		$\sigma_{\log(\tau)}$	

TABLE 6.5: *Ranking of Multi-Temperature and the Stochastic Multi-Temperature Model Parameters by Importance*

## 6.3 Parameters and Hyperparameters Uncertainty Quantification

At this point, the problem of quantifying the uncertainty for the parameters and hyperparameters that the sensitivity analysis ranked as important has been faced following the Bayesian approach proposed in Chap. 4.

The priors that have been chosen for this process are listed in Tab. 6.6. For all the parameters and hyperparameters, such distributions are chosen as uniform [14].

It must be underlined that the standard deviation of the likelihood distribution has been considered as an hyperparameter and calibrated as well for both the Multi-Temperature and the Stochastic Multi-Temperature models. In this way, we are entrusting SMUQ with the task of determining the magnitude of the error that affects the prediction of the QoI and that is originated from some unknown (or simply not captured) physical sources.

Model Parameter		Prior	MT	SMT
Arrhenius Pre-Exp.	$A_{N_2+N}$	$\mathcal{U}[8 \cdot 10^{20}, 8 \cdot 10^{23}]$	✓	✓
Arrhenius Pre-Exp.	$A_{N_2+N_2}$	$\mathcal{U}[8 \cdot 10^{19}, 8 \cdot 10^{22}]$	✓	✓
Arrhenius Pre-Exp.	$A_{N_2+e^-}$	$\mathcal{U}[6.2 \cdot 10^{23}, 6.2 \cdot 10^{26}]$	✓	✓
Arrhenius Pre-Exp.	$A_{N+e^-}$	$\mathcal{U}[7.5 \cdot 10^{32}, 7.5 \cdot 10^{35}]$	✓	✓
Limiting Cross Section VT	$\sigma_C$	$\mathcal{U}[3.15 \cdot 10^{-22}, 1 \cdot 10^{-20}]$	✓	✓
Dissociation En. Removal	$C_{N_2}$	$\mathcal{U}[0, 1]$	✓	✓
Electron En. Removal	$I_e$	$\mathcal{U}[9.05 \cdot 10^6, 9.05 \cdot 10^9]$	✓	✓
Relaxation Time Const. Exp. Mean	$-\mu_{\log(\tau)}$	$\mathcal{U}[5, 13]$		✓
Relaxation Time Const. Exp. SD	$\sigma_{\log(\tau)}$	$\mathcal{U}[0.0001, 0.1]$		✓
Likelihood SD	$\sigma_L$	$\mathcal{U}[0.0001, 0.03]$	✓	✓

TABLE 6.6: *Prior Distributions for the Parameters and Hyperparameters.*

Tab. 6.7 lists SMUQ input parameters. With the aim of reducing the autocorrelation of the sampled parameters, each of the chains has been cleaned by removing its first (non stationary) part [31]; moreover, from the remaining length, 9 draws out of 10 points have been discarded [33]. The parameters  $n_{\%}$  and  $n_{/}$  in the table characterize such process. The posterior distributions for the parameters and hyperparameters which

SMUQ input		Value
Chains:		
Number of Chains	$n_{proc}$	16
Length of the Chain	$n_{MCMC}$	100000
Percentage of Burn-in	$n\%$	10%
Discarded values	$n_{/}$	9/10
II Hierarchical Level Sampled Points	$G$	1000
Delayed Rejection Method:		
Number of steps	$n_{DR}$	3
Proposal scaling factor	$\omega_{DR}$	0.009
Adaptive Method:		
AM Burn-in	$n_{AM_0}$	2000

TABLE 6.7: *SMUQ Inputs.*

result from the calibration process are shown in the next figures together with the related correlations.

### 6.3.1 Scenario 1:

#### 6.3.1.1 Scenario 1: Multi-Temperature Model

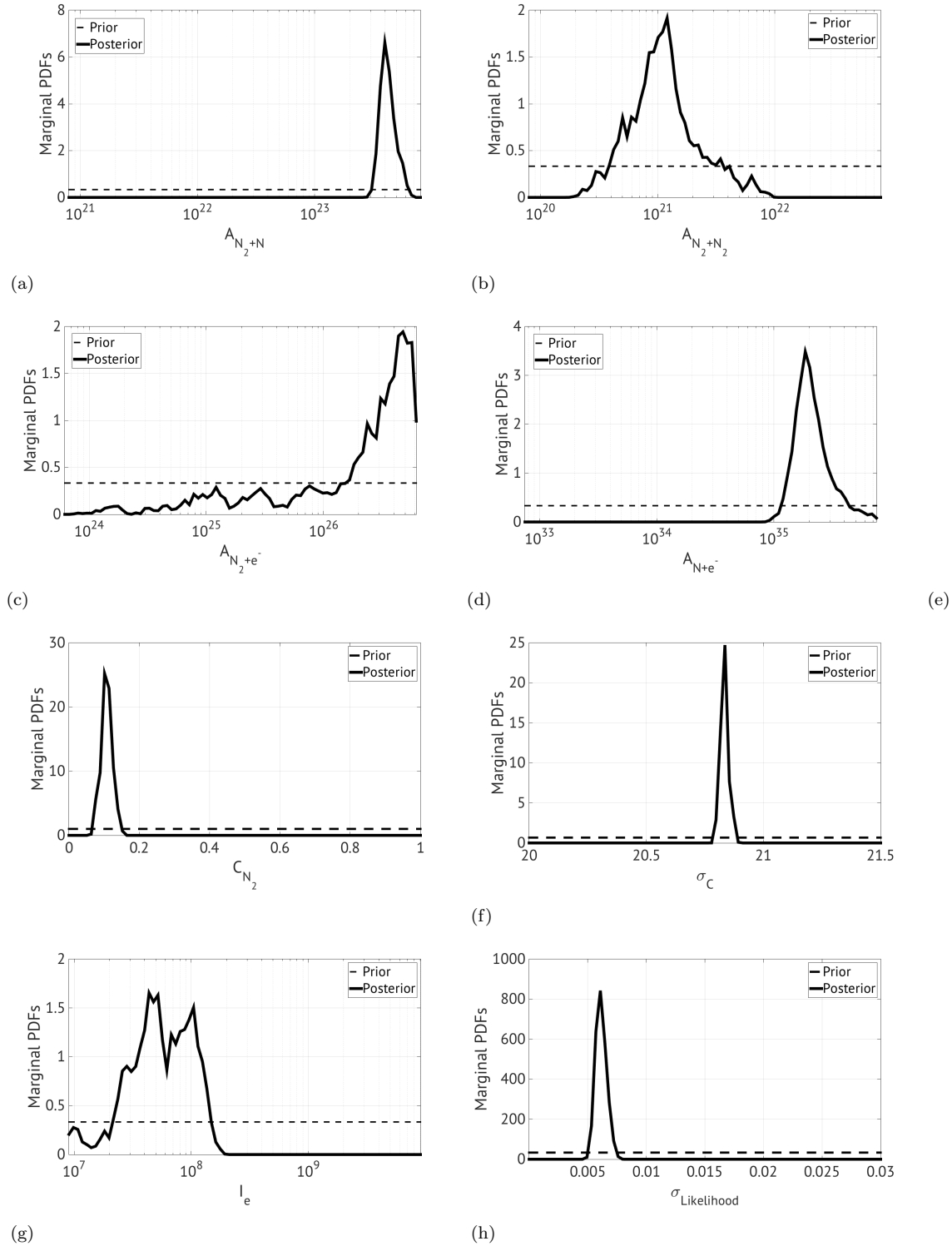


FIGURE 6.11: Posterior Distributions of the Calibrated MT Parameters.

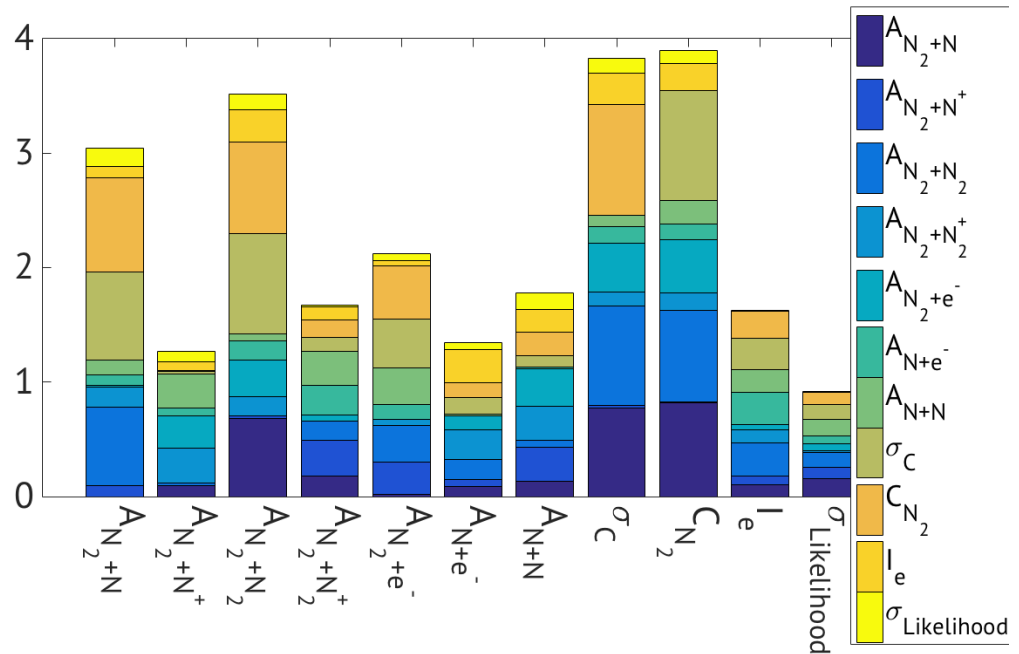


FIGURE 6.12: Correlation between the Calibrated MT Parameters.

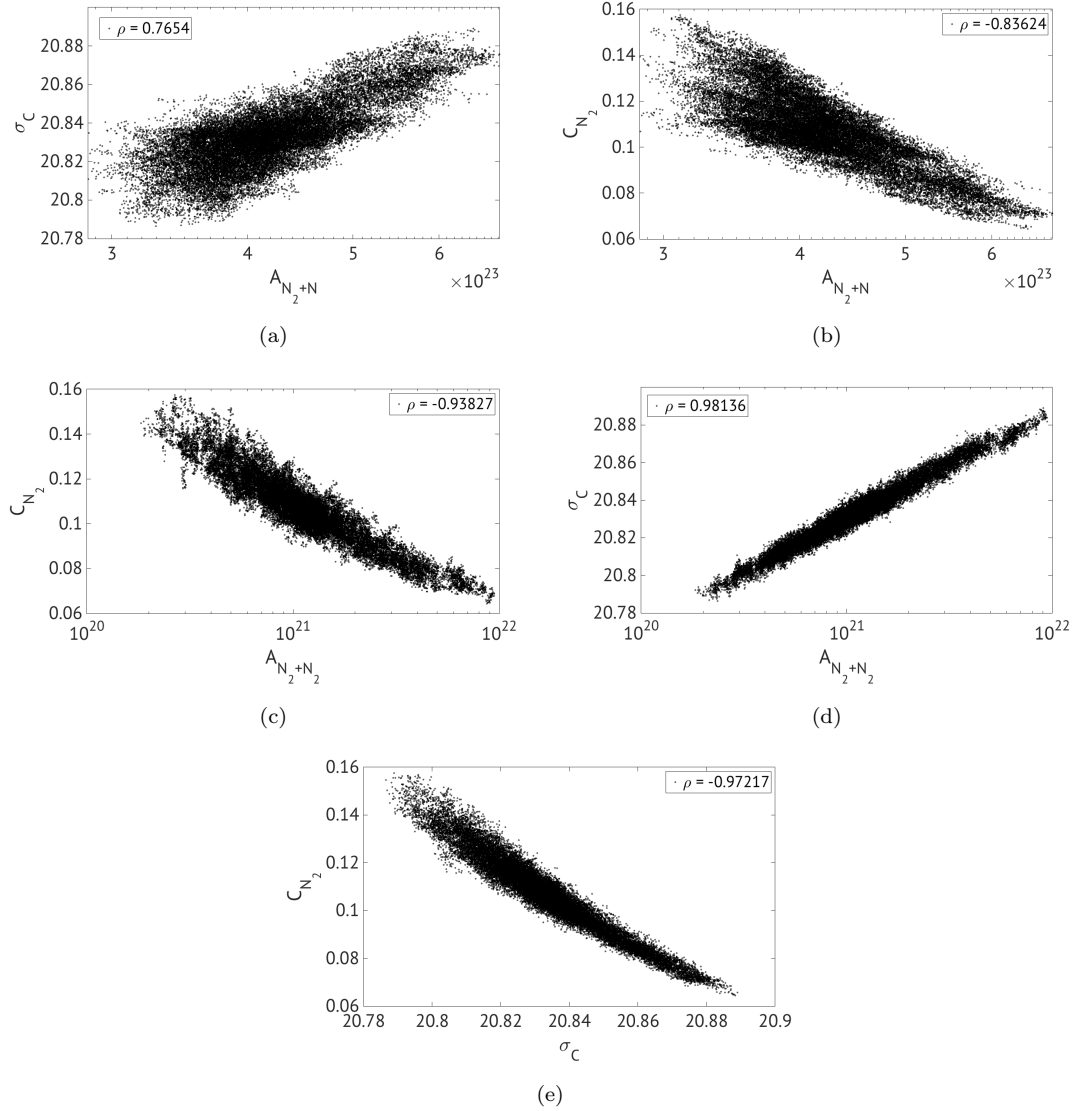


FIGURE 6.13: Correlation between the MT Calibrated Parameters  $A_{N_2+N}$ ,  $A_{N_2+N_2}$ ,  $\sigma_C$  and  $C_{N_2}$

### 6.3.1.2 Scenario 1: Stochastic Multi-Temperature Model

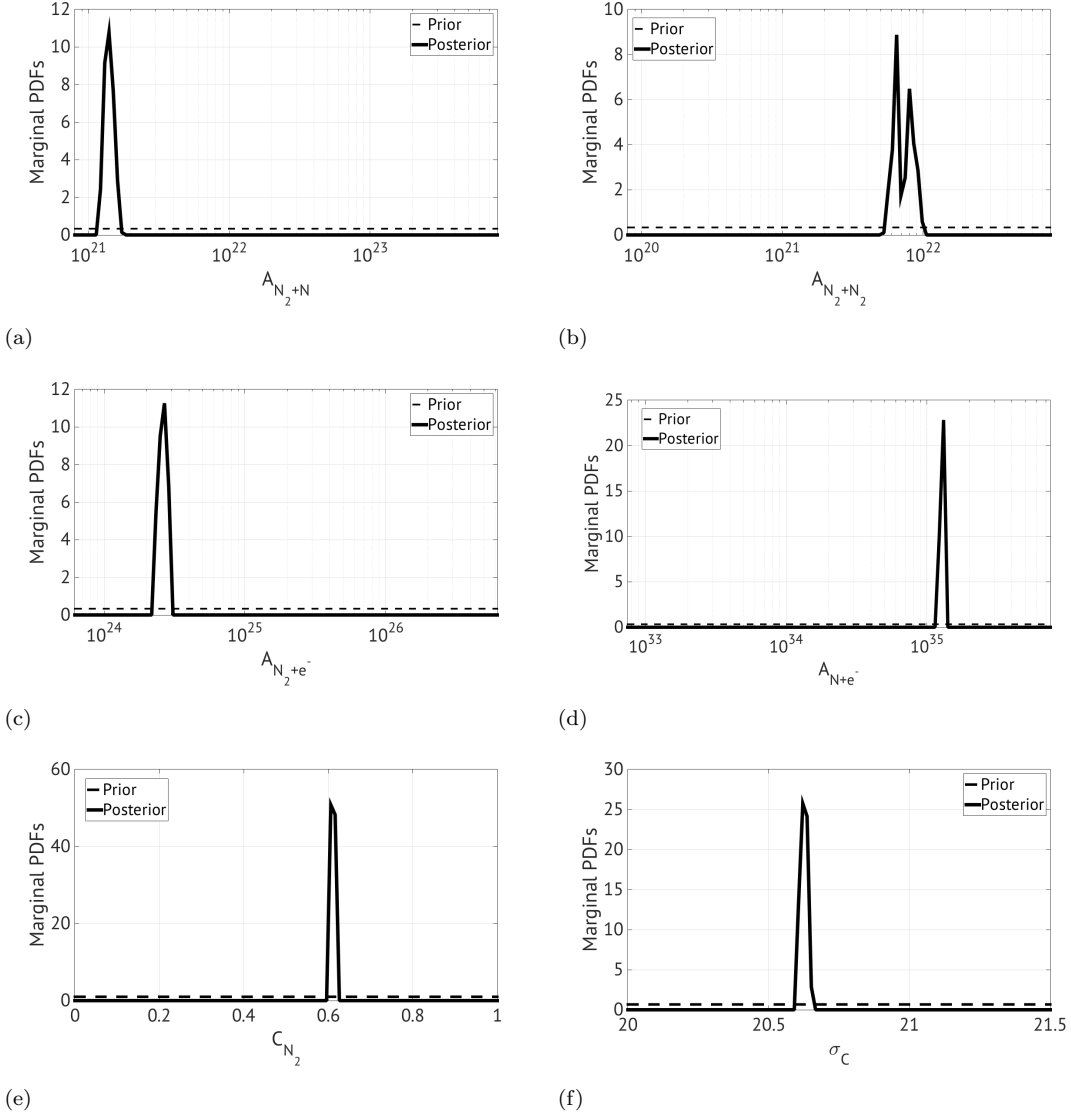


FIGURE 6.14: *Posteriors Distributions of the Calibrated Parameters of the Stochastic MT.*

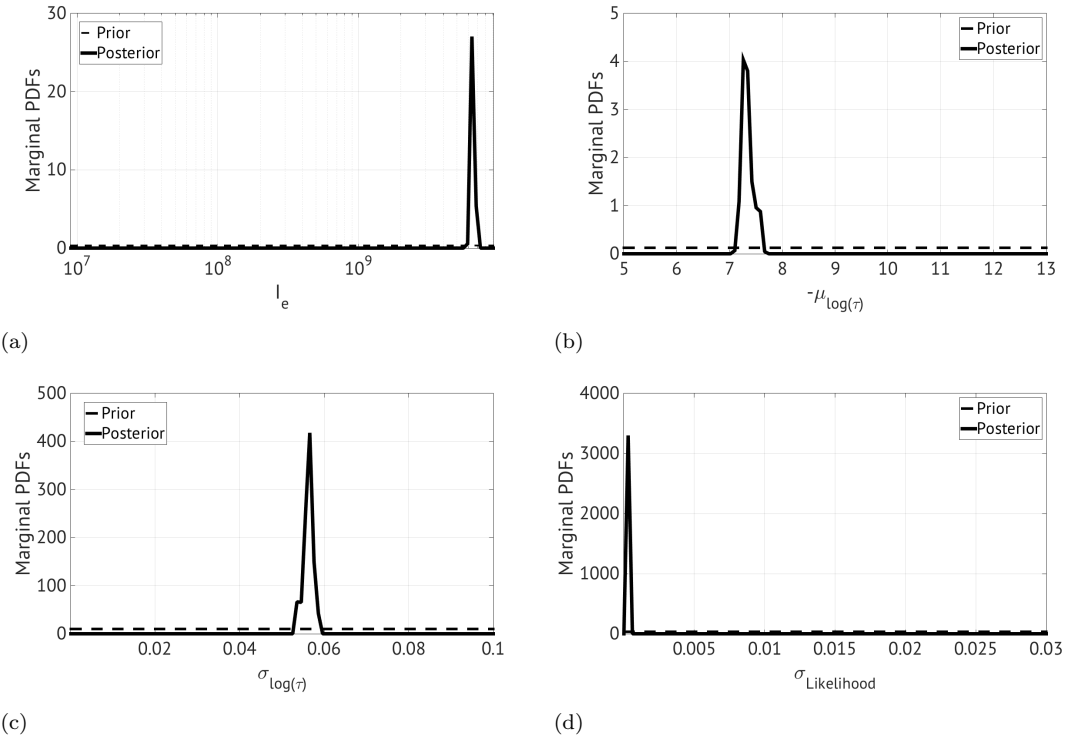


FIGURE 6.15: *Posterior Distributions of the Calibrated Parameters of the Stochastic MT.*

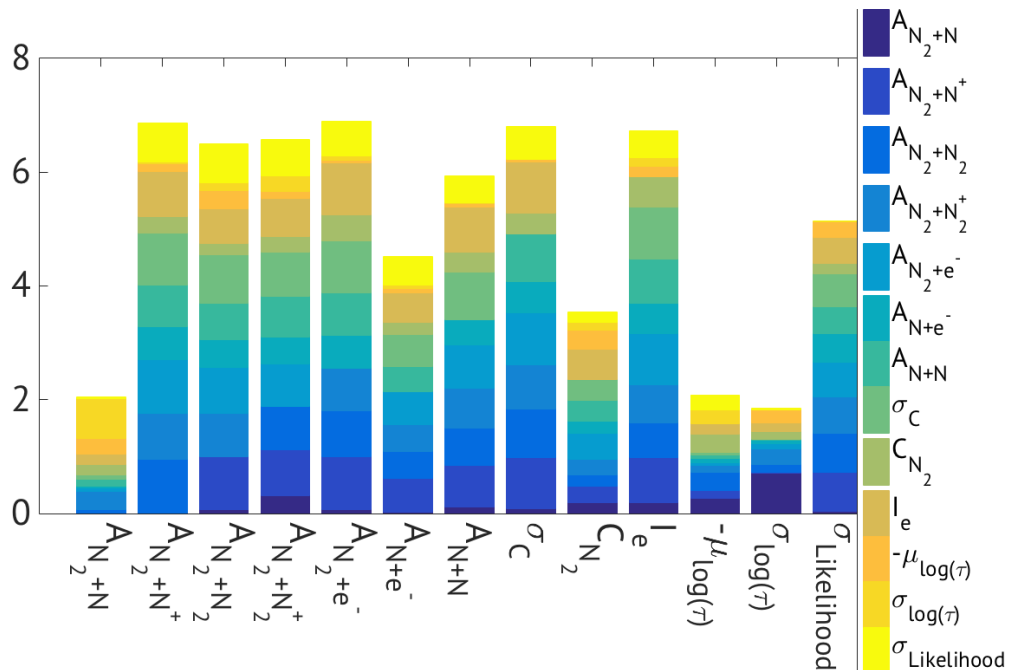


FIGURE 6.16: *Correlation between the Calibrated Parameters of the Stochastic MT.*

### 6.3.2 Scenario 2:

#### 6.3.2.1 Scenario 2: Multi-Temperature Model

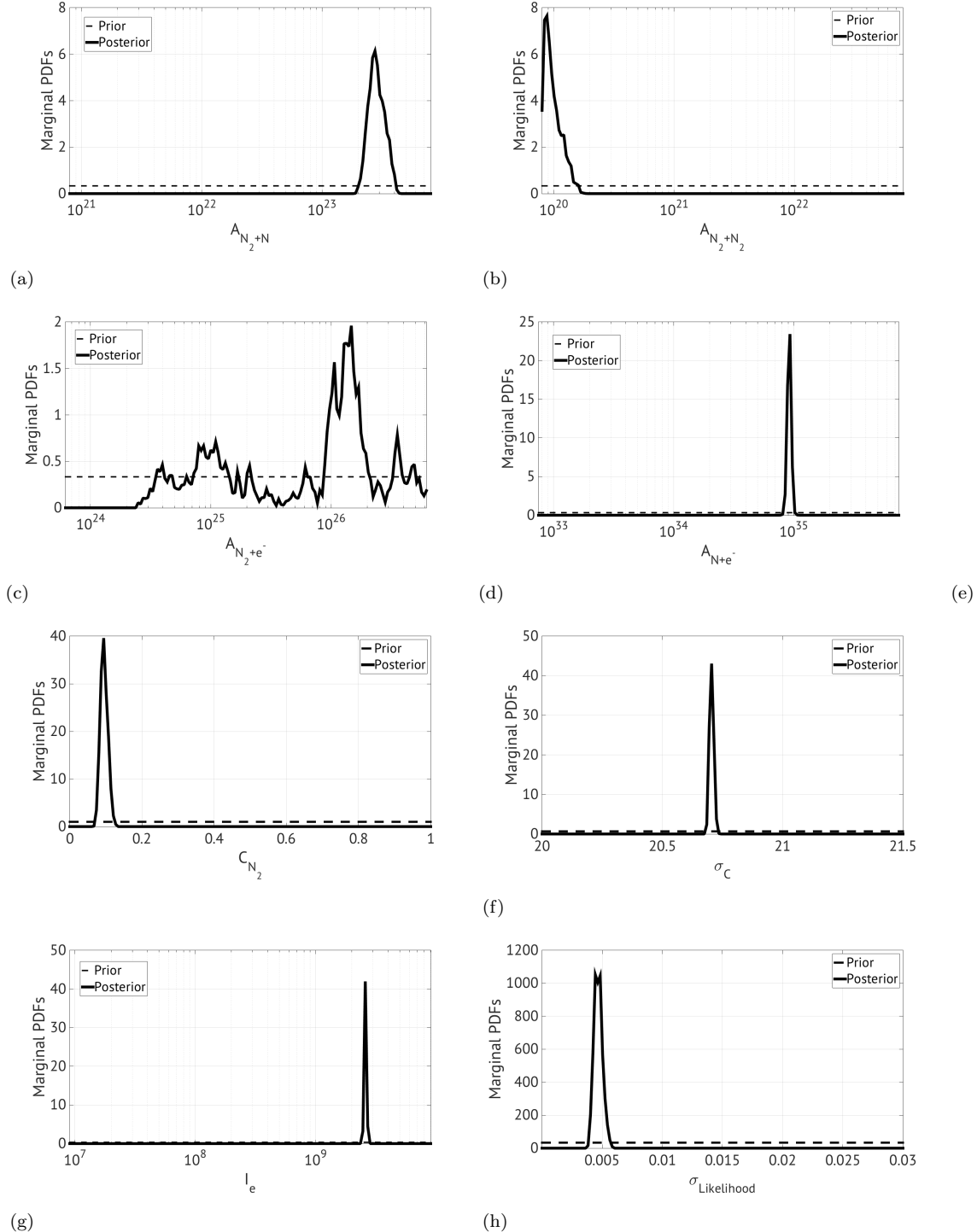


FIGURE 6.17: Posterior Distribution of the Calibrated MT Parameters.

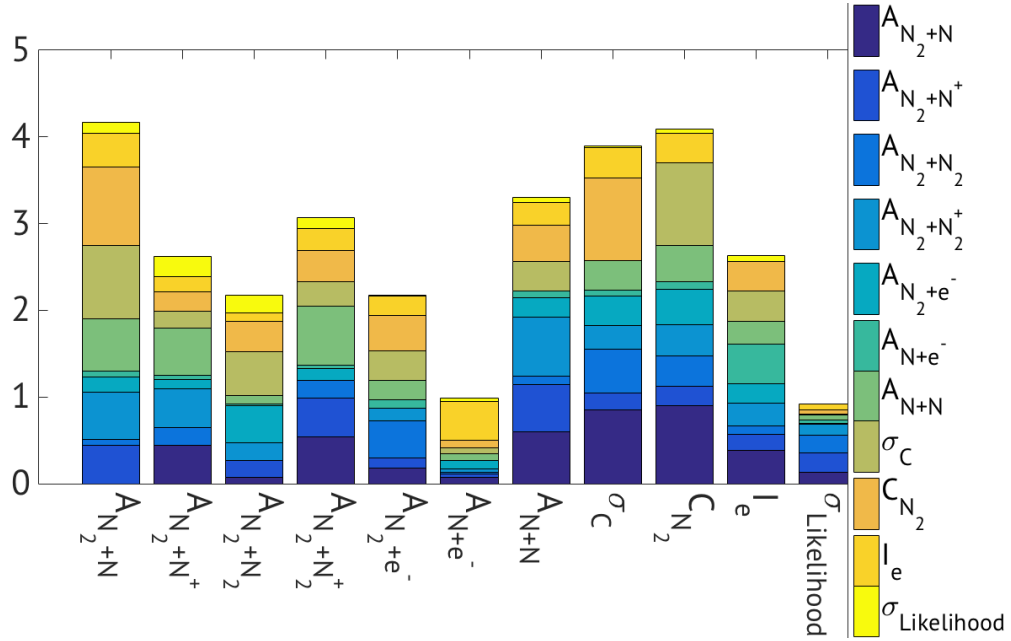
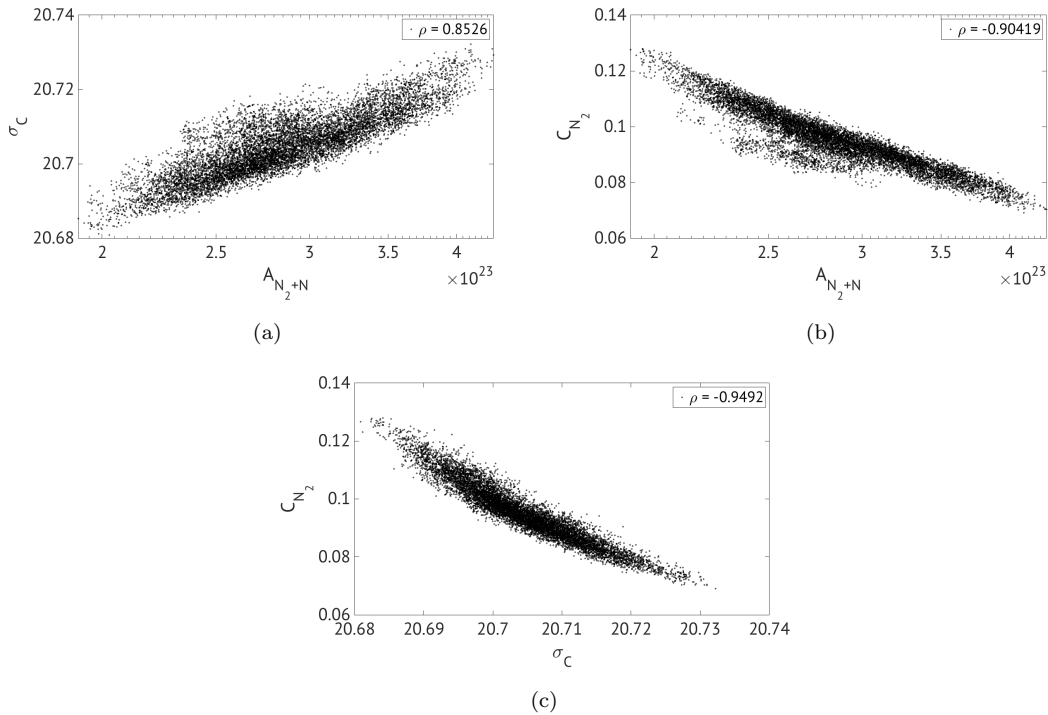


FIGURE 6.18: Correlation between the Calibrated MT Parameters.

FIGURE 6.19: Correlation between the MT  $A_{N_2+N}$ ,  $C_{N_2}$  and  $\sigma_C$ .

### 6.3.2.2 Scenario 2: Stochastic Multi-Temperature Model

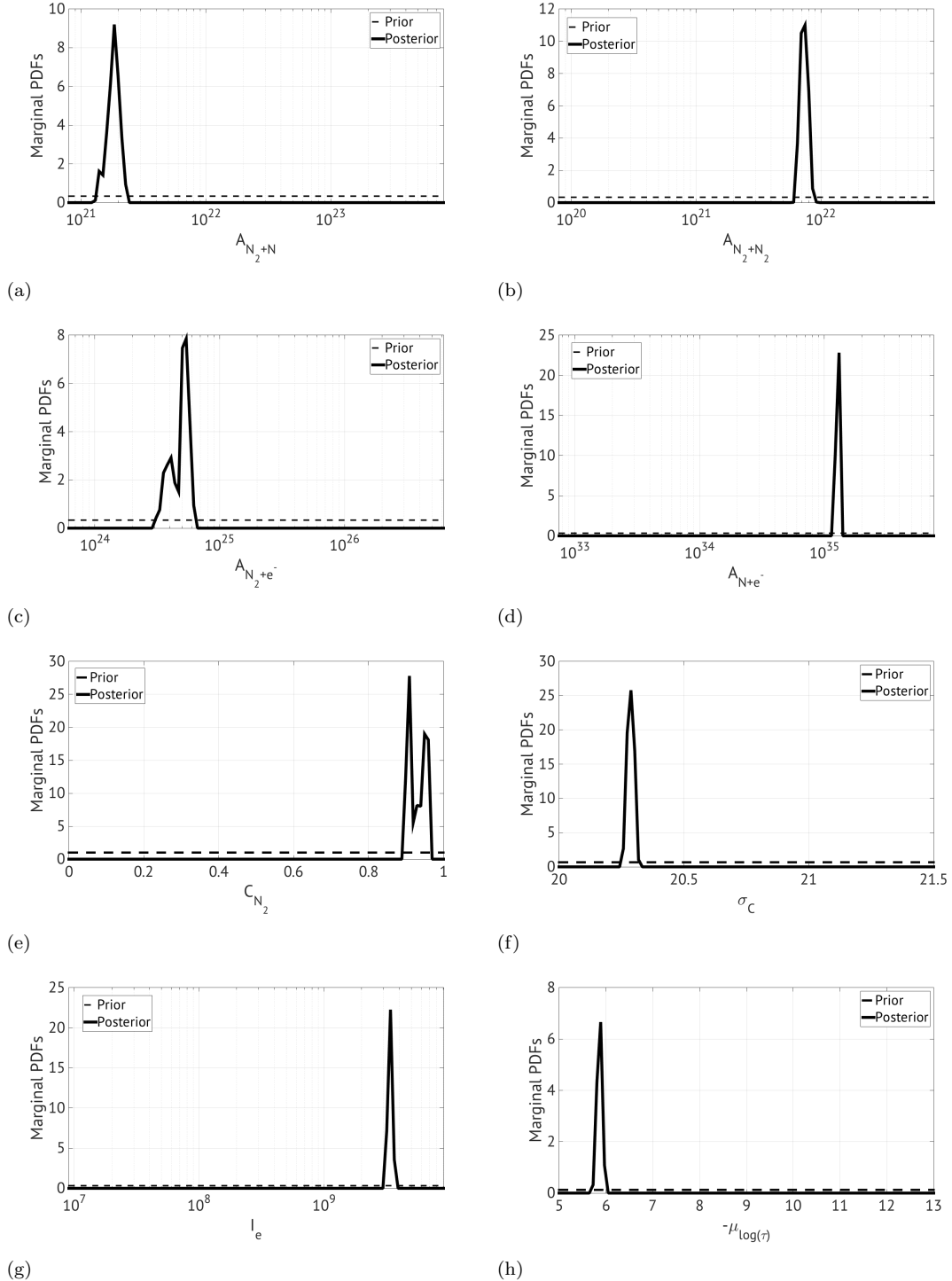


FIGURE 6.20: *Posteriors Distributions of the Calibrated Parameters of the Stochastic MT.*

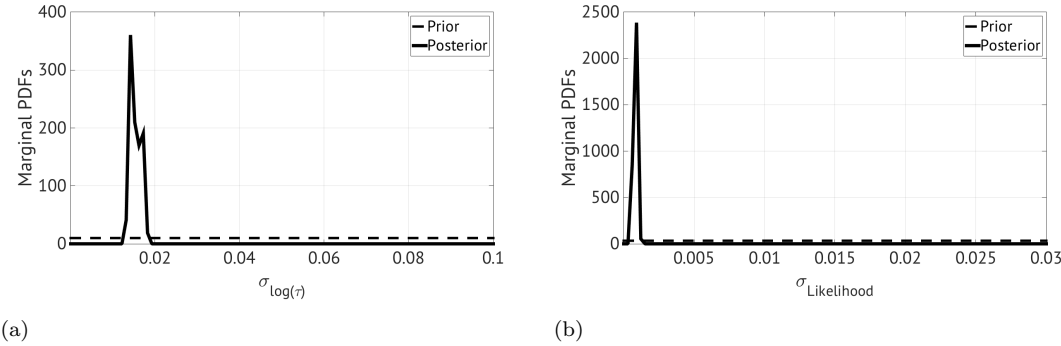


FIGURE 6.21: *Posteriors Distributions of the Calibrated Parameters of the Stochastic MT.*

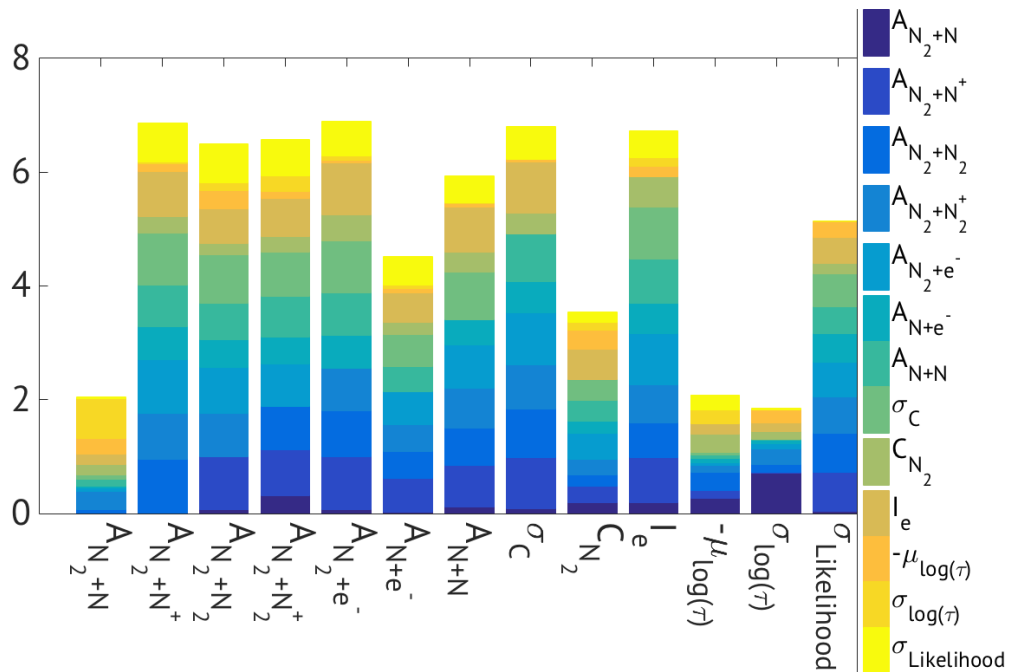


FIGURE 6.22: *Correlation between the Calibrated Parameters of the Stochastic MT.*

### 6.3.2.3 Considerations

The calibration results are in well agreement with the sensitivity analysis outcomes: the more important the parameter (Tab. 6.5), the narrower its posterior.

Moreover, a closer comparison between such distributions (Fig. 6.23) points out that the parameters of the Stochastic Multi-Temperature (solid lines in the figure) are less scenario dependent compared to the ones of the classic Multi-Temperature. A possible explanation is that such dependence on the non-equilibrium magnitude has been absorbed by the stochastic hyperparameters.

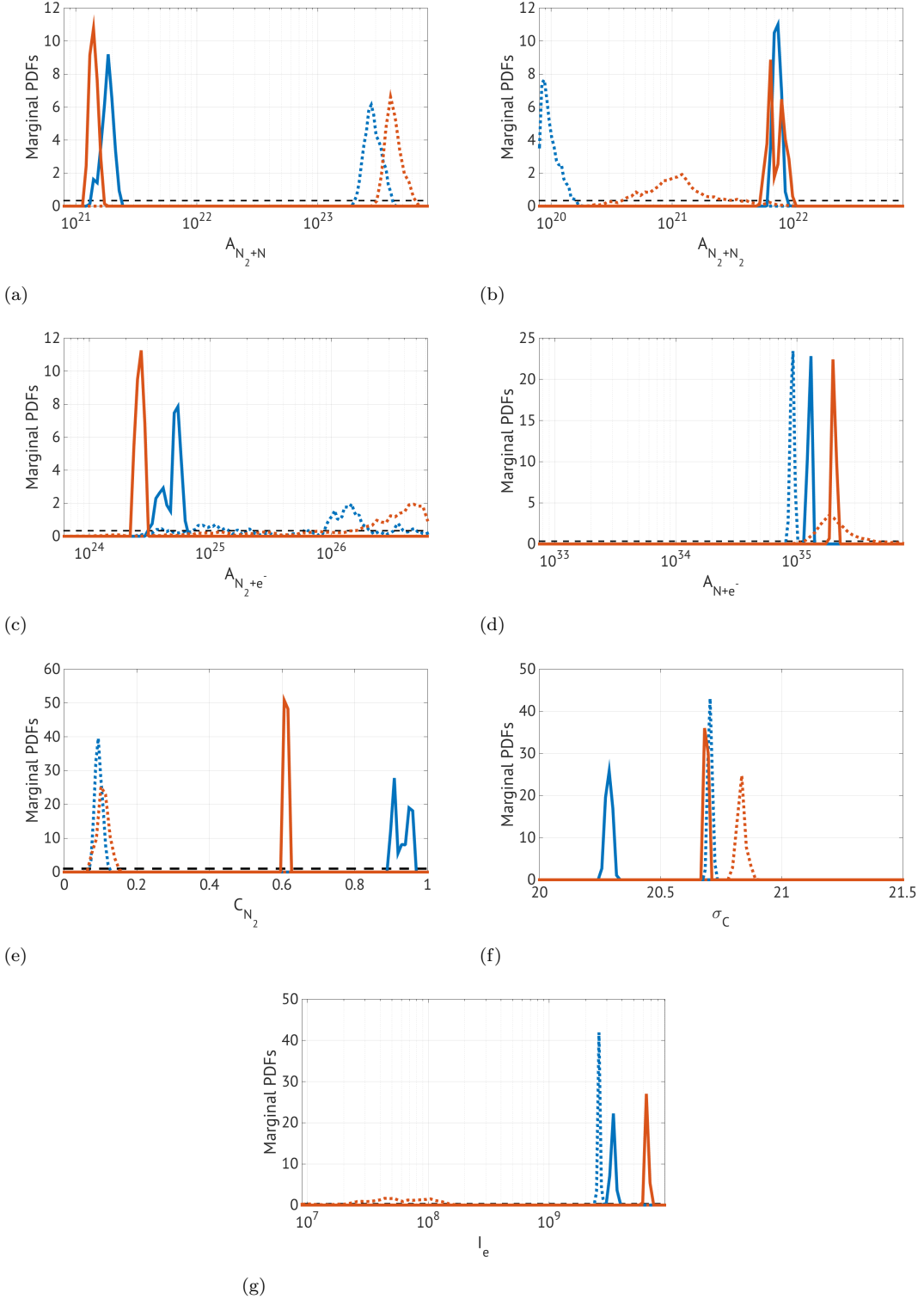


FIGURE 6.23: Comparison between the Parameters Posterior Distributions of the Multi-Temperature (dashed lines) and of the Stochastic Multi-Temperature (solid lines). The red color refers to Scenario 1, while the blue indicates Scenario 2.

The posteriors of  $-\mu_{\log(\tau)}$  and  $\sigma_{\log(\tau)}$  are represented in 6.24. The distributions of the mean, in particular, respects the intuition that the larger the inflow velocity, the stronger the non-equilibrium phenomena and the slower the thermal relaxation process. Thus, a larger time constant for the second scenario compared to first test case should have been expected.

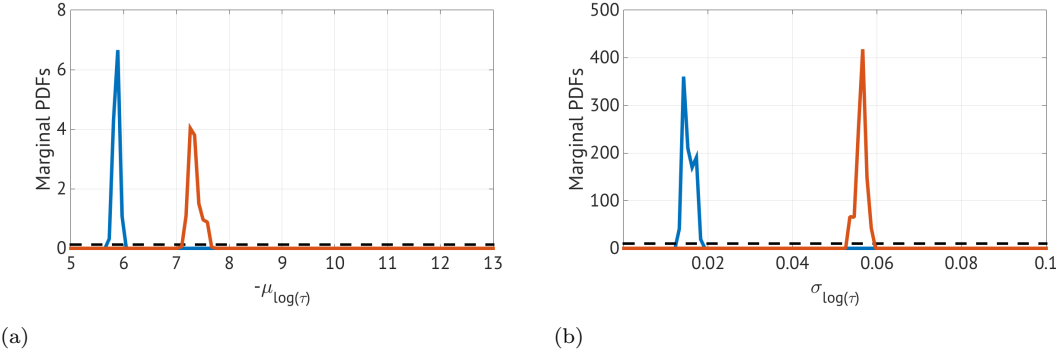


FIGURE 6.24: *Comparison between the Hyperparameters Posterior Distributions. Red color refers to Scenario 1, while the blue indicates Scenario 2.*

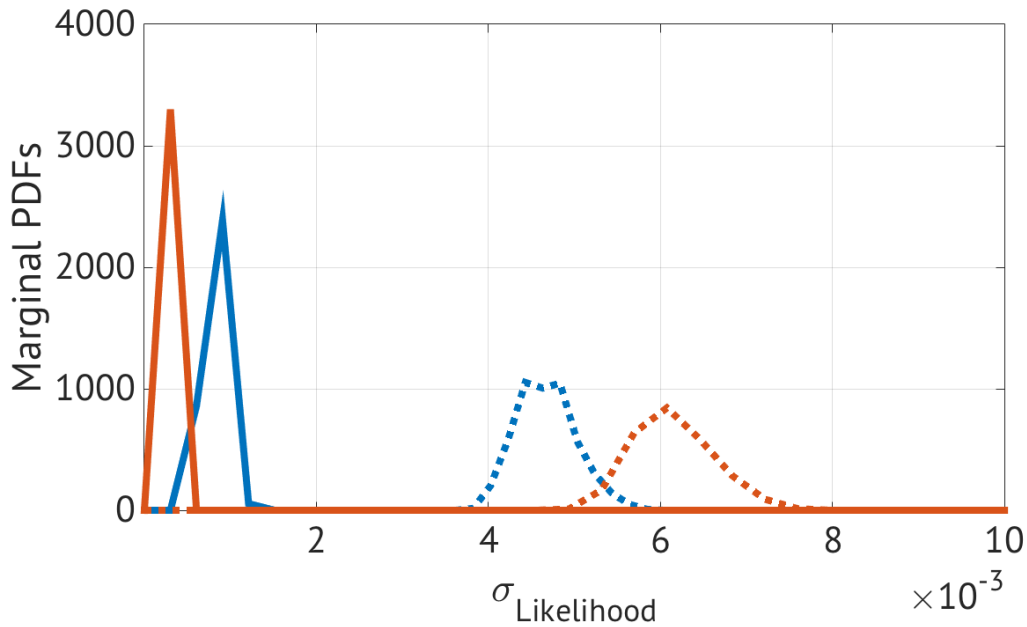


FIGURE 6.25: *Likelihood Posterior Distribution for the Multi-Temperature (dashed lines) and of the Stochastic Multi-Temperature (solid lines). Red color refers to Scenario 1, while the blue indicates Scenario 2.*

The posterior for the last hyperparameter  $\sigma_L$ , shown in Fig. 6.25, reveals that the uncertainty that arises from unspecified origins and that we represented through the likelihood has been reduced by the stochastic model by 95% for the first scenario and by 80% for the second one. This fact clearly attests that the most part of the model

error has been moved backward to the physics-based stochastic model.

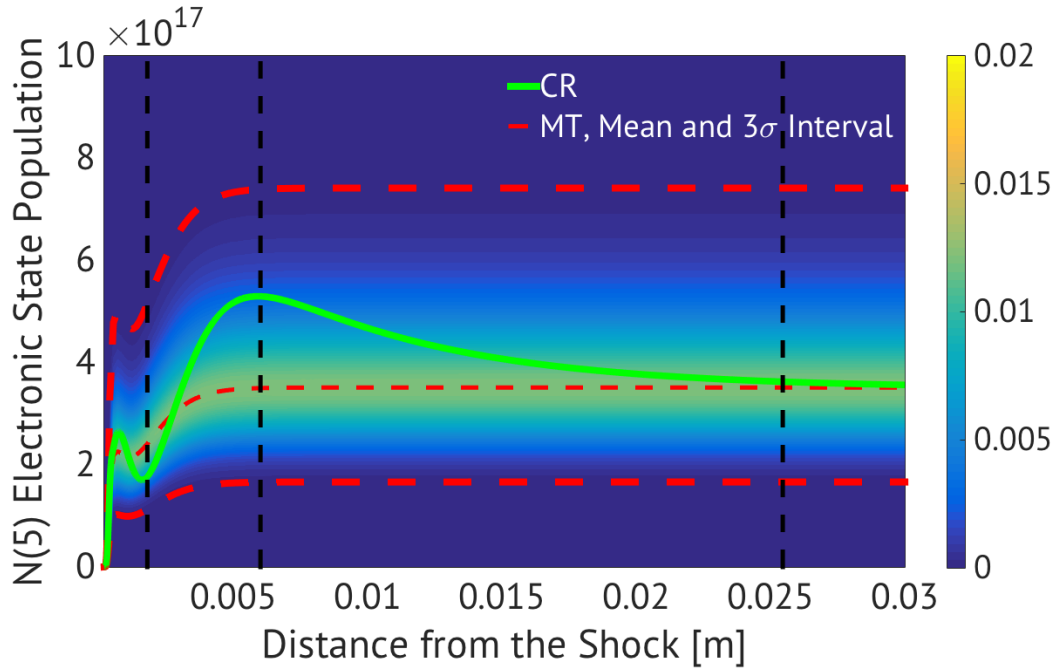
Fig.s 6.13 and 6.19 point out the strong correlation that affects  $C_{N_2}$ ,  $\sigma_C$ ,  $A_{N_2+N}$  in scenarios 1 and 2 and  $C_{N_2}$ ,  $\sigma_C$ ,  $A_{N_2+N}$  and  $A_{N_2+N_2}$  in scenario 1. Such relationship between the parameters derives from their linked character in describing the dissociative processes, as it was pointed out in Chap. 2 while presenting the equations for the thermal relaxation.

## 6.4 Forward Propagation

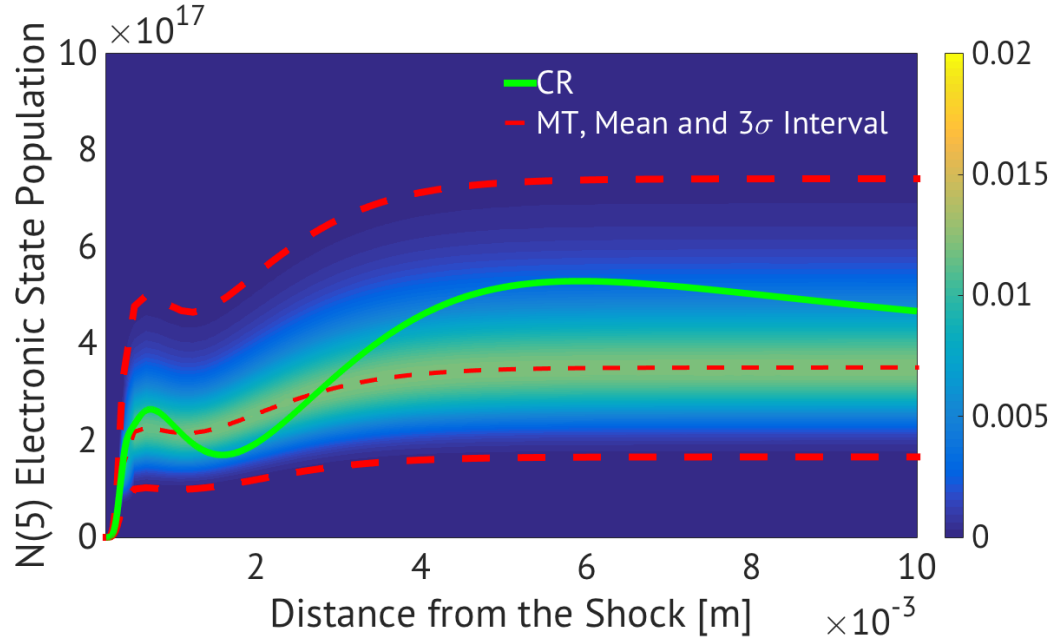
[h] The parameters and hyperparameters uncertainties have been finally propagated to the Nitrogen Electronic Level Populations by solving the forward problem and taking into account the multiplicative contribution that arises from the stochastic model represented by the likelihood function (see Fig. 6.1). This section presents the results for the spatial evolution of the fifth electronic state and for the populations distributions over the overall electronic energy levels at certain spatial points.

#### 6.4.0.1 Scenario 1: Multi-Temperature Model

[h]



(a)



(b)

FIGURE 6.26: Posterior Distribution of  $N(5)$  Electronic State Population (i.e., Observable Quantity) (a), zoomed in the region close to the shock (b).

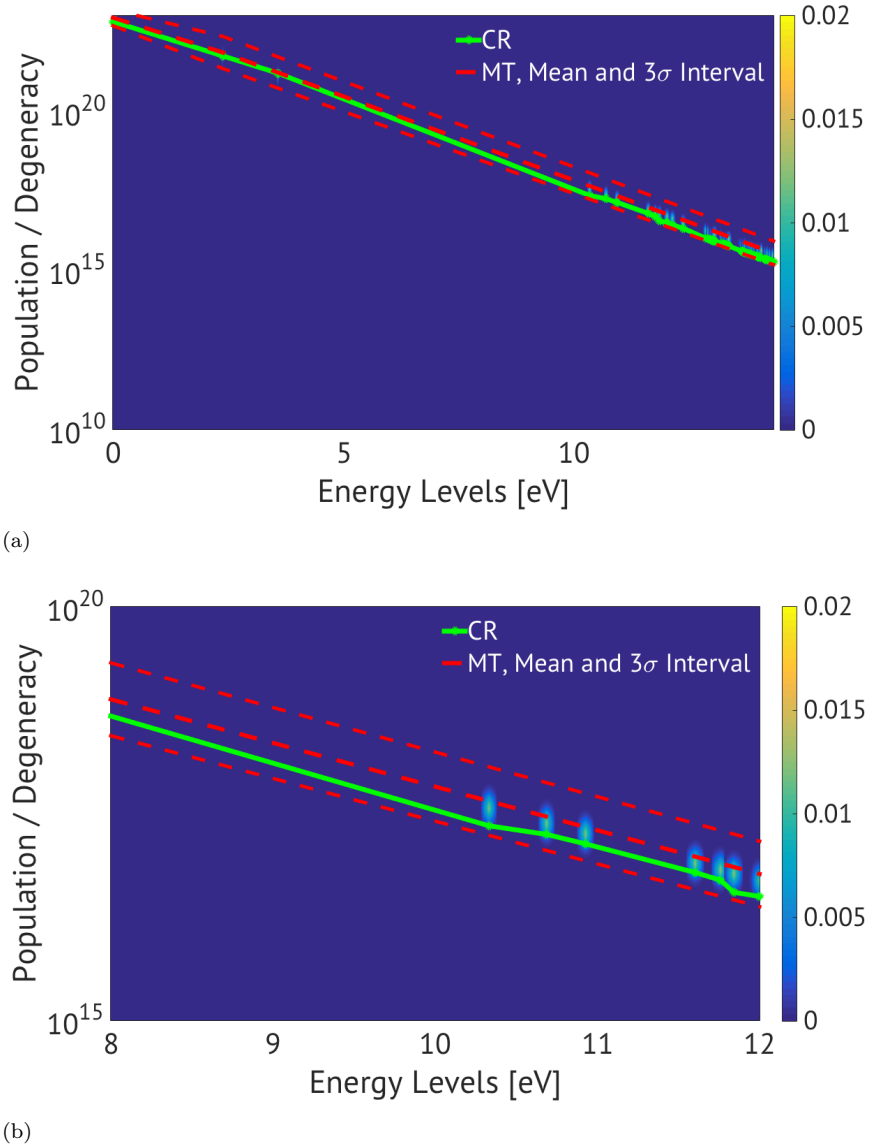
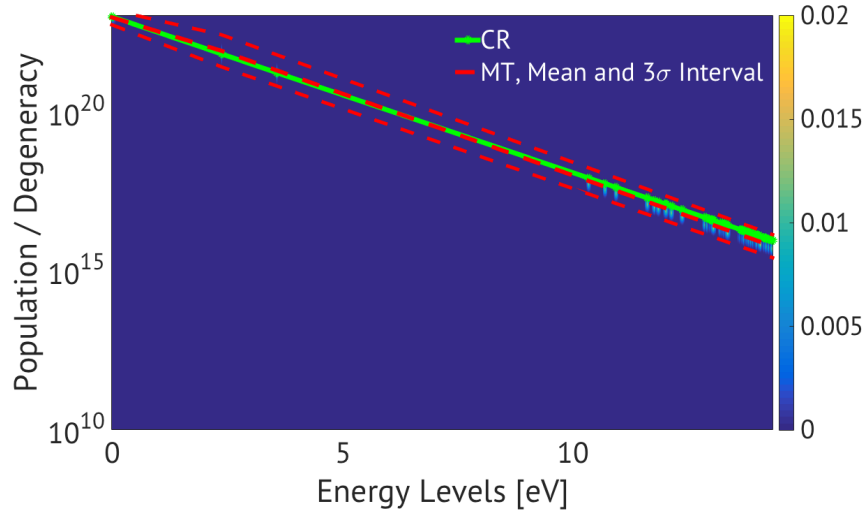
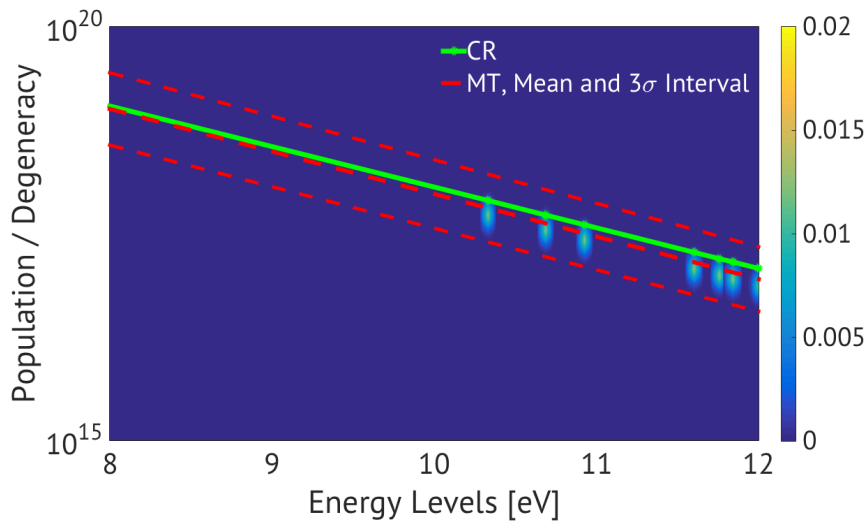


FIGURE 6.27: *Posterior Distribution of the Nitrogen Electronic States with distance from the shock  $x = 0.18\text{cm}$  (a) with the relative 5th Electronic State zoomed in Fig. (b).*



(a)



(b)

FIGURE 6.28: *Posterior Distribution of the Nitrogen Electronic States with distance from the shock  $x = 0.6\text{cm}$  (a) with the relative 5th Electronic State zoomed in Fig. (b).*

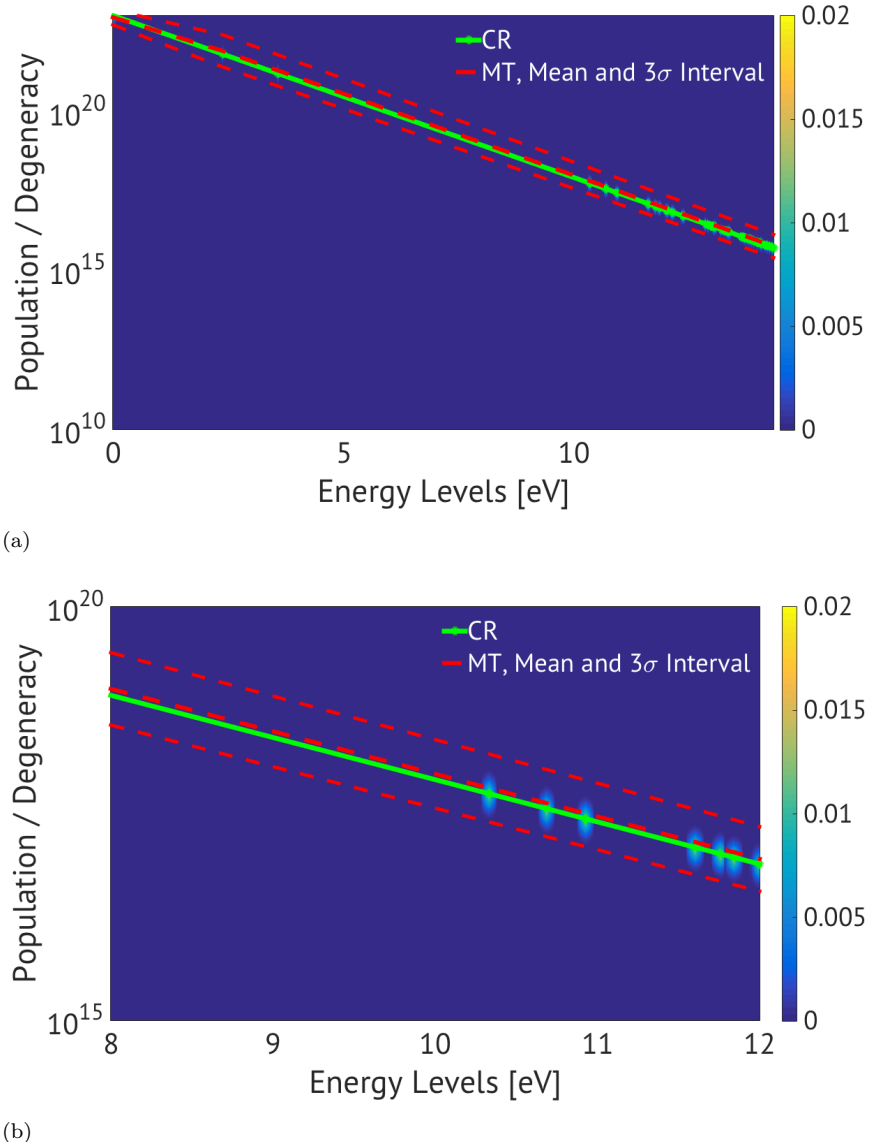


FIGURE 6.29: *Posterior Distribution of the Nitrogen Electronic States with distance from the shock  $x = 2.5\text{cm}$  (a) with the relative 5th Electronic State ( $10.687\text{eV}$ ) zoomed in Fig. (b).*

#### 6.4.0.2 Scenario 1: Stochastic Multi-Temperature Model

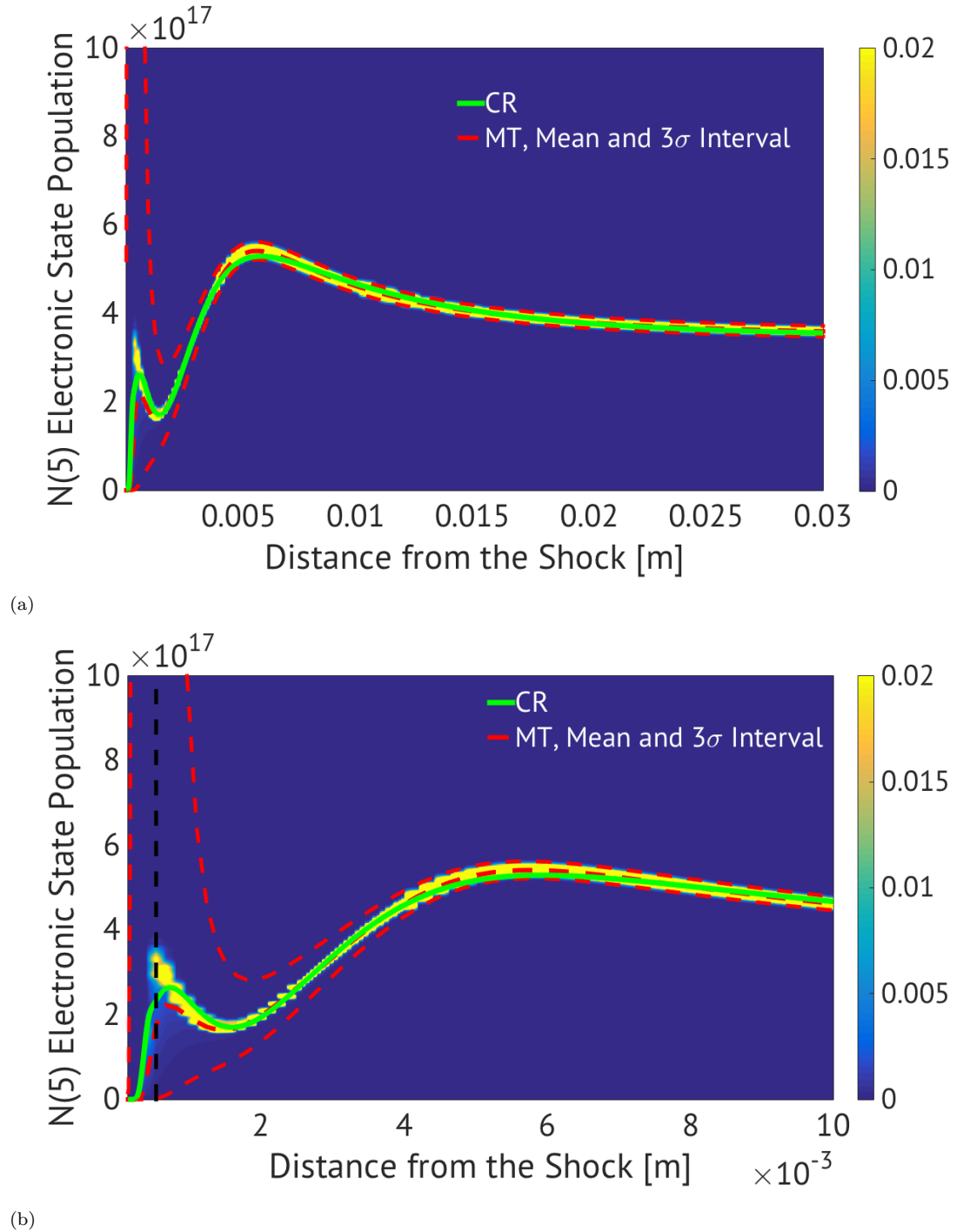


FIGURE 6.30: *Posterior Distribution of  $N(5)$  Electronic State Population (i.e., Observable Quantity) (a), zoomed in the region close to the shock (b).*

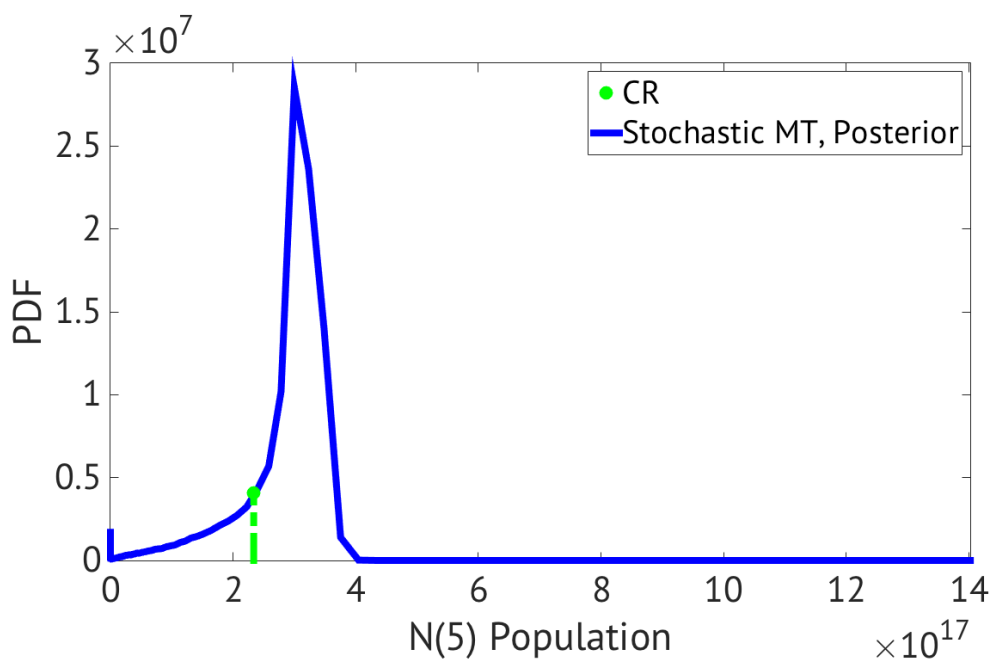


FIGURE 6.31: Posterior Distribution of  $N(5)$  Electronic State Population analyzed at  $0.05\text{cm}$  from the shock.

#### 6.4.0.3 Scenario 2: Multi-Temperature Model

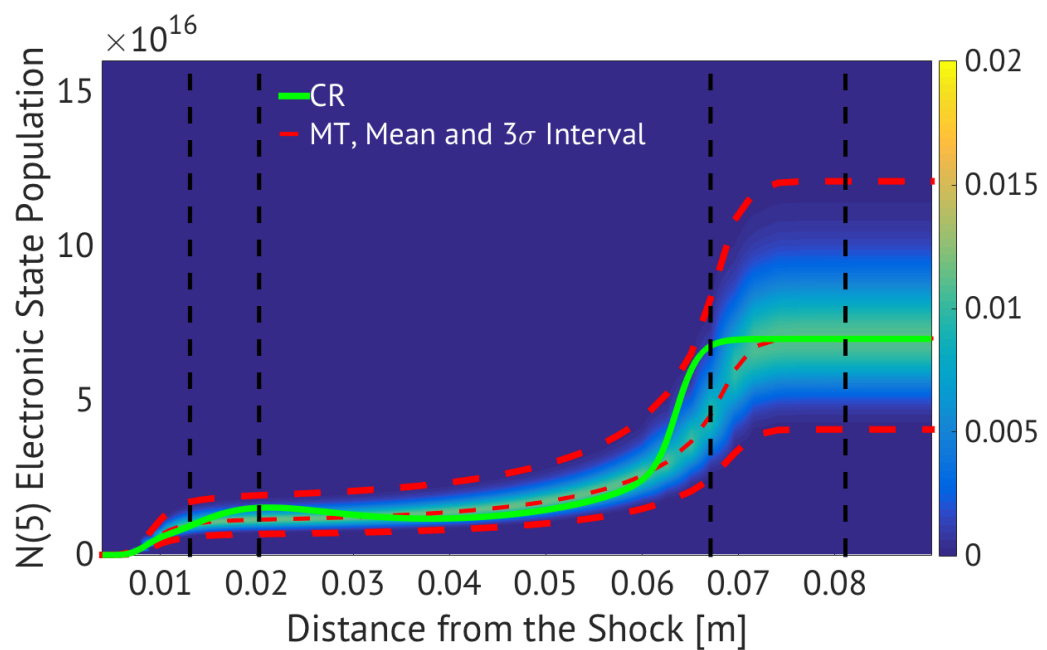
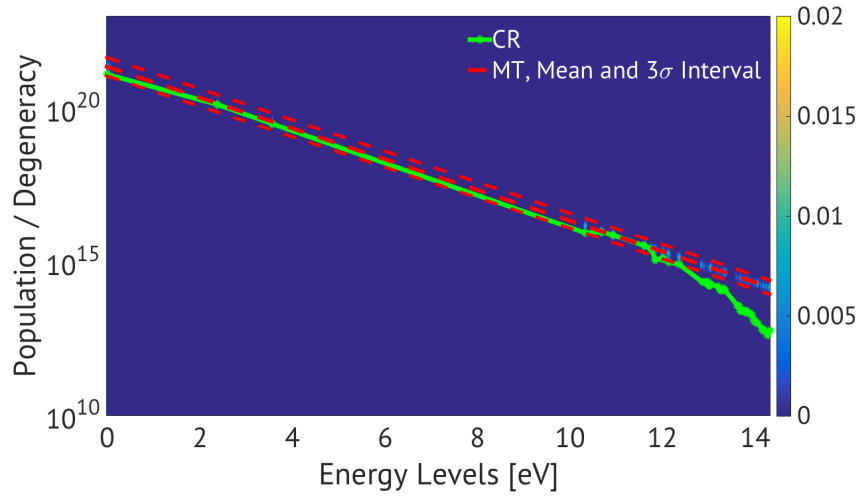
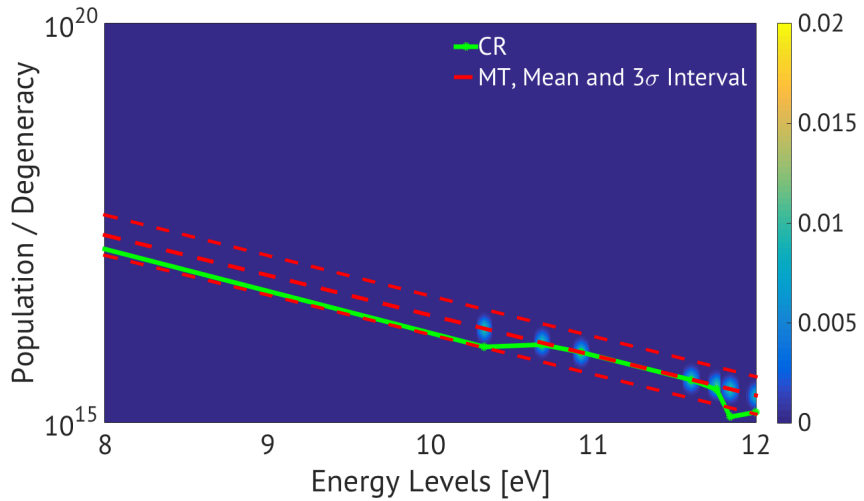


FIGURE 6.32: *Posterior Distribution of  $N(5)$  Electronic State Population (i.e.: Observable Quantity).*

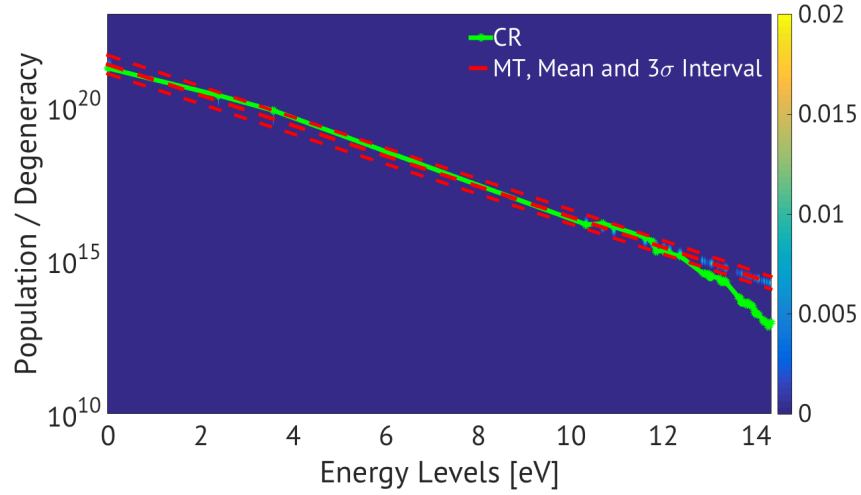


(a)

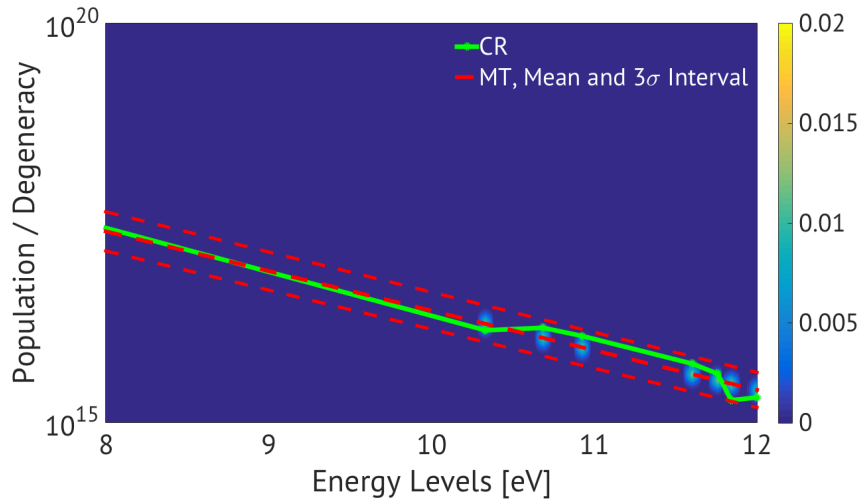


(b)

FIGURE 6.33: *Posterior Distribution of the Nitrogen Electronic States with distance from the shock  $x = 0.12\text{cm}$  (a) with the relative 5th Electronic State ( $10.687\text{eV}$ ) zoomed in Fig. (b).*

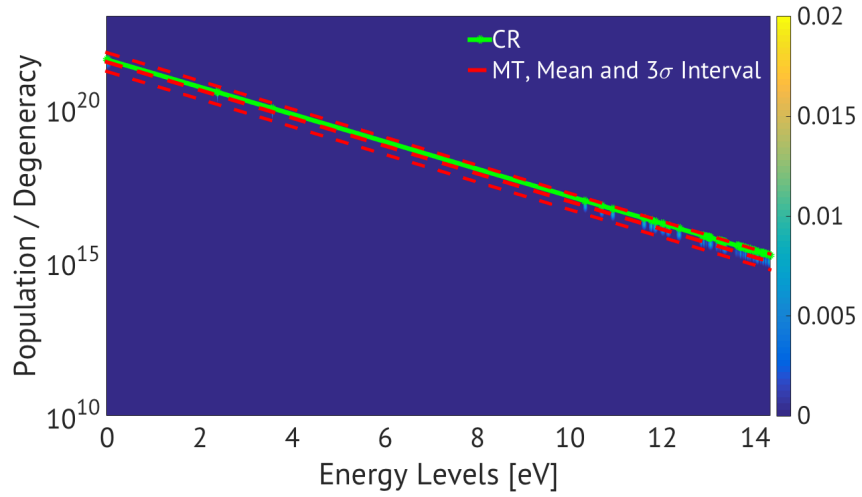


(a)

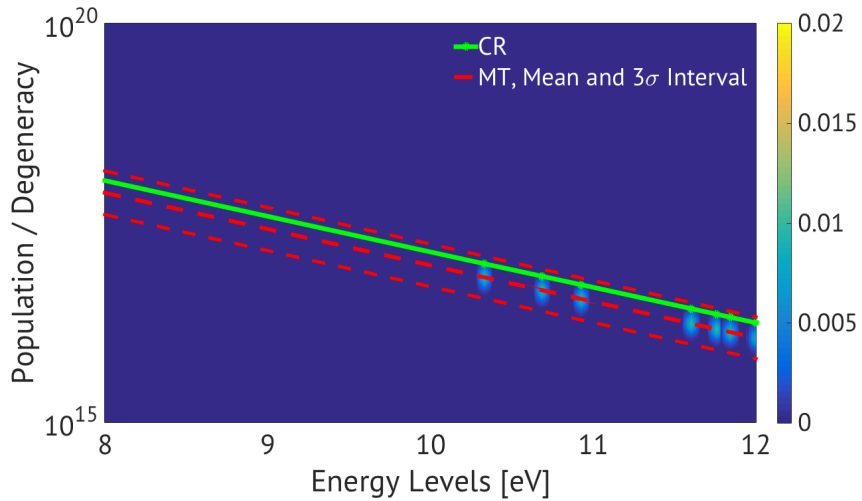


(b)

FIGURE 6.34: *Posterior Distribution of the Nitrogen Electronic States with distance from the shock  $x = 2\text{ cm}$  (a) with the relative 5th Electronic State ( $10.687\text{ eV}$ ) zoomed in Fig. (b).*

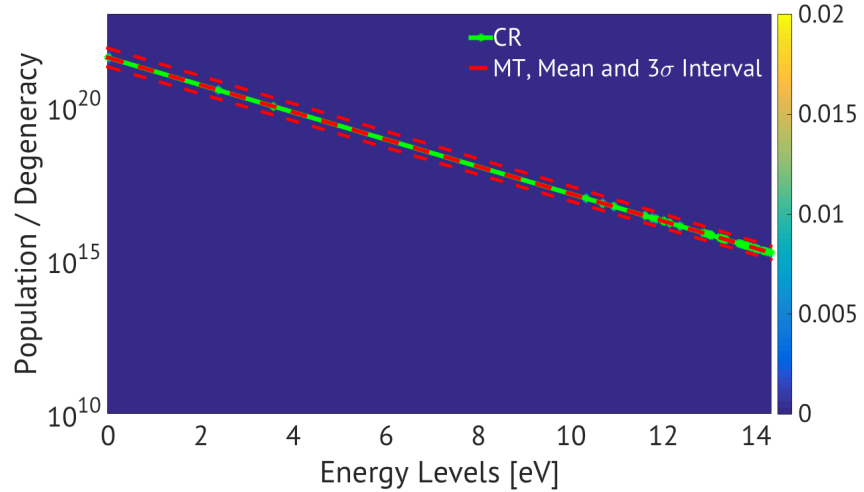


(a)

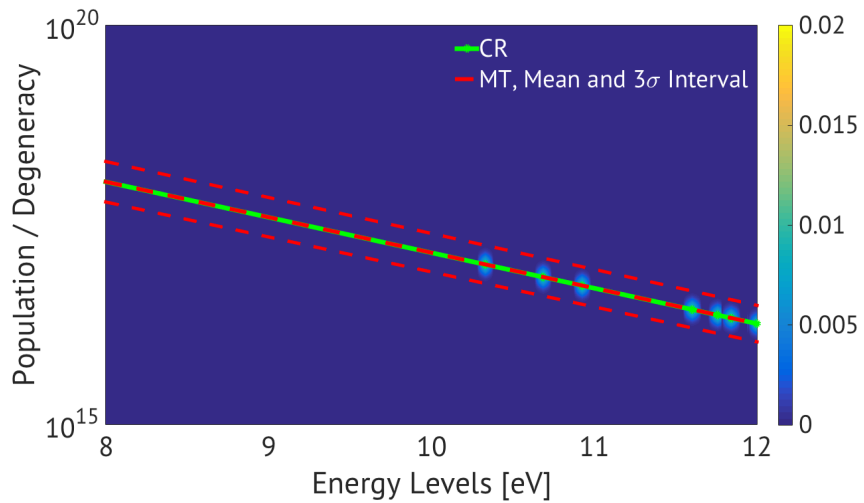


(b)

FIGURE 6.35: *Posterior Distribution of the Nitrogen Electronic States with distance from the shock  $x = 6.7 \text{ cm}$  (a) with the relative 5th Electronic State ( $10.687 \text{ eV}$ ) zoomed in Fig. (b).*



(a)



(b)

FIGURE 6.36: *Posterior Distribution of the Nitrogen Electronic States with distance from the shock  $x = 8\text{cm}$  (a) with the relative 5th Electronic State ( $10.687\text{eV}$ ) zoomed in Fig. (b).*

#### 6.4.0.4 Scenario 2: Stochastic Multi-Temperature Model

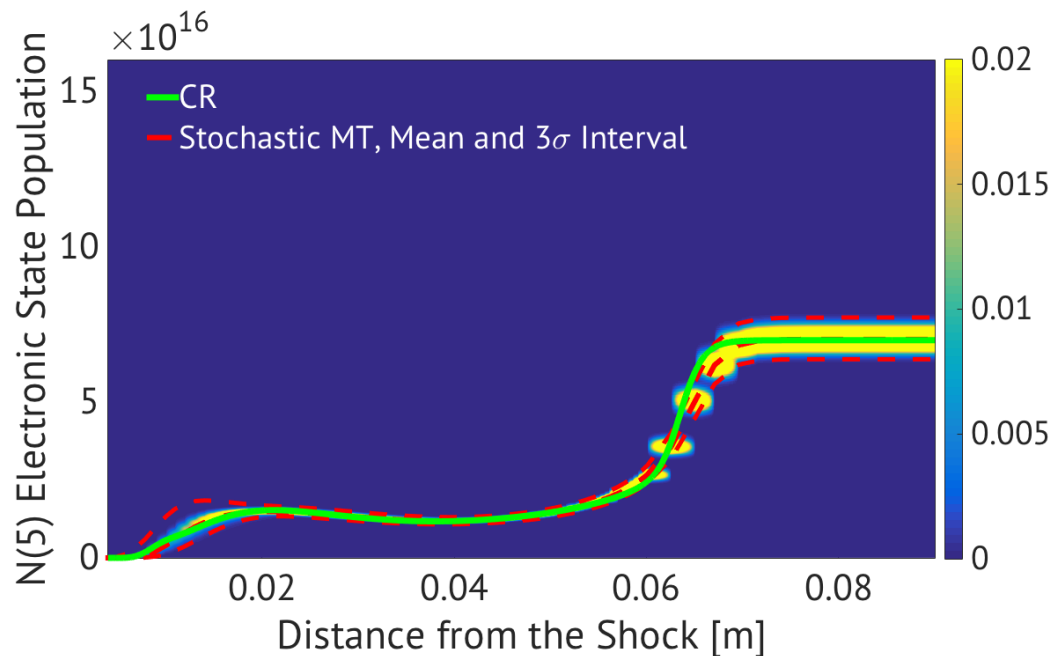


FIGURE 6.37: Posterior Distribution of  $N(5)$  Electronic State Population (i.e.: Observable Quantity) obtained through the Stochastic Multi-Temperature.

#### **6.4.0.5 Considerations**

The uncertainty propagation attested that the calibrated Stochastic Multi-Temperature worked extremely well in the second scenario, almost nullifying the prediction confidence interval; on the other hand, it failed to compute with the same accuracy the population at the first local maximum in the first scenario conditions. This has been likely caused by the simple description adopted for the thermal relaxation dynamics. Indeed, a direct consequence of the first order description is the fact that the stochastic electronic level population has to choose if reproducing accurately either the first local maximum or the equilibrium region. Anyway, even for this first scenario the population predicted by the Stochastic Multi-Temperature appeared more reliable than the one computed by means of the classic Multi-Temperature.

# **Chapter 7**

## **Conclusions and Future Research**

### **7.1 Accomplishments**

The results presented in the previous chapter pointed out the advantages of approaching the validation problem for the prediction of the radiative heat flux by means of a physics-based stochastic description for the model error. Indeed, through a simple and computationally inexpensive representation of the dynamics of thermal relaxation of the high energy electronic levels it has been possible, at the same time:

- To reduce the uncertainty on the flow predicted quantities. Indeed, for the test scenario case characterized by strong non-equilibrium conditions, it has been shown that the addition of the Stochastic description to the Multi-Temperature model almost nullified the electronic population confidence interval.
- To create a strategy for a consistent propagation of the parameters uncertainty and the structural inadequacy to the radiative heat flux, if it is assumed as non-measurable quantity of interest. The error in prediction, that in the older approaches was simply stored in a calibrated term positioned upstream to the observable quantity and for this reason did not influence the quantity of interest, is now accumulated by the stochastic model that has been positioned inside the overall solver. For this reason, not only the radiative intensity but also the radiative heat flux can be informed. The accomplishment of this task has been attested through the reduction of the likelihood standard deviation up to 95%.
- To show that the assumption of the electronic energy states being in equilibrium between each other (Maxwell-Boltzmann distribution) is one of the primary sources of uncertainty in the electronic populations and, as consequence in the radiative heat flux, and, in turn, on the design of a manned planetary vehicles heat shield.

## 7.2 Future Work

Future research related to this thesis work will regard:

- **Moving to Air11 and Coupling with Radiation**

Such step forward will permit to abandon the Computational Radiative Model as basis for comparison and to take advantage of the available air experiments (e.g., Fire II cases of study). Moreover, coupling the radiation solver will permit to approach the radiative heat flux as the direct quantity of interest.

- **Mathematical Formulation of the Stochastic Relaxation Model proposed in this Thesis**

Prof. Panesi and the author of this manuscript are currently working on deriving a mathematical foundation for the Stochastic Relaxation Model proposed in the previous chapters, starting from the Master Equation.

- **Moving the Stochastic Model into the Flow Solver**

So far the stochastic model has been treated as a mere post-processing of the flow solver outcomes. A further step will be coupling such non deterministic term with the model for the computation of the plasma quantities. A possible way in order to achieve this task is the introduction of a stochastic source term in the energy modes governing equations.

- **New Applications for SMUQ**

Mr. Przemyslaw Rostkowski, Graduate Student at University of Illinois at Urbana Champaign, is currently using SMUQ for validating a new ablation model through the data acquired by the Exploration Flight Test 1.

Other challenging models will be tested by means of SMUQ in the future months.

# List of Figures

1.1	“Temperature behind a normal shock wave as a function of free-stream velocity at a standard altitude of 52km.” [1] . . . . .	10
1.2	Representation of the main phenomena occurring in the flow field surrounding a capsule experiencing the (re-)entry in a planetary atmosphere (courtesy of NASA). . . . .	11
1.3	“Comparison of radiative and convective stagnation-point heat transfer.” [1] . . . . .	12
2.1	“Flow regime classification according to the Knudsen number” [5] . . . . .	15
2.2	“Electronic energy level population for atomci nitrogen. CR model at 0.2 cm, 0.4 cm and 0.6 cm” [8]. Free stream characteristic quantities: $P_1 = 2.0Pa$ , $T_1 = 195K$ , $u_1 = 11360m/s$ . Post-shock characteristic quantities: $P_2 = 3827Pa$ , $T_2 = 62377$ , $u_2 = 1899m/s$ . . . . .	17
2.3	The radiative intensity $\hat{I}_\lambda$ and the radiative heat flux $\hat{q}_{rad}$ are computed by the Flow Solver and the Radiative Model in series. $\mathbf{u}$ represents the set of the scenario inputs (e.g., free stream pressure, temperature and shock speed), $\boldsymbol{\theta}_{FS}$ and $\boldsymbol{\theta}_{RS}$ indicate the sets of model parameters respectively of the flow solver and of the radiative model, and $\mathbf{y}_{FS}$ are the outputs of the flow solver (e.g., populations of the energy levels) . . . . .	25
2.4	“Schematic description of shock-tube measurements” [14] . . . . .	25
4.1	Abstract problem without any model imperfection. . . . .	34
4.2	Kennedy-O’Hagan’s representation of the model uncertainty. . . . .	36
4.3	Representation of the model uncertainty proposed by Oliver <i>et al.</i> . . . . .	37
4.4	The process of making reliable predictions for unobservable quantities. . . . .	39
4.5	10000 uncorrelated points obtained from sampling a multivariate normal distribution with $\mu = [2, 3]$ and $\sigma = [3, 1.5; 1.5, 2]$ . . . . .	43
4.6	A Markov chain random walk (b) for sampling 200 points from a generic PDF (a). . . . .	44
4.7	Metropolis Algorithm: Two candidate jumps for the PDF $P(X)$ (black lines) obtained from the current point $X_t$ by means of the same proposal $q(X_i, X_{i+1})$ (blue lines, not normalized). The $X^*$ proposed in (a) will certainly be accepted in the ( $\alpha = 1.90$ ), while the $X^*$ in (b) will be rejected with a probability of 56% ( $\alpha = 0.4370$ ) . . . . .	45

4.8 Metropolis Algorithm: On the left column: three different proposal functions (blue lines): $q_1 = \mathcal{N}(\mu_q; \sigma_q = \sigma_{q_1})$ (a), $q_2 = \mathcal{N}(\mu_q; \sigma_q = \sigma_{q_1}/2)$ (c), $q_3 = \mathcal{N}(\mu_q; \sigma_q = \sigma_{q_1}/4)$ (e). On the right column: three different Metropolis-Hastings Markov chains produced by means of three different proposal functions, respectively: (b) from (a), (d) from (c) and (f) from (e). . . . .	47
4.9 Delayed Rejection Method: A first candidate point $X^*$ has been obtained in (a) sampling a normal proposal distribution with $\sigma_q$ and it has been rejected. A new proposal has then been computed with $\sigma'_q = \sigma_q/2$ and it generated a candidate $X^{*'}$ (b). This point has been rejected as well and a new point $X^{*''}$ has been produced from a new distribution with $\sigma''_q = \sigma_q/4$ (c). . . . .	49
4.10 Adaptive Method: A MCMC is started from the black point for sampling the target distribution in (a). The resulting chain and the current proposal distribution (level lines) are shown at four computational times: at the first point (b), at an instant right after the end of the non-adaptation period (c) (note that the covariance matrix is almost diagonal), and at two successive instants (d and e). . . . .	51
4.11 Convergence of chain by MH, DR, AM and DRAM, from a case of study in Haario <i>et al.</i> 's paper [39]. The sum of the residual squares between data and output is plotted against simulation time . . . . .	52
4.12 50% – HPD regions (area in blue) for the PDF in black. . . . .	54
4.13 Schematic representation of SMUQ's working strategy in solving the Calibration and Validation processes: once the input parameters for the Bayesian Inference, for the Markov Chain and for the Delayed Rejection Adaptive Method are specified, SMUQ is able to quantify the model uncertainty and to establish the reliability of the model predictions taking advantage of the available data $D$ . . . . .	56
5.1 Introduction of a stochastic model between the Flow Solver and the Radiative Model. Such term upgrades 2.3 in order to apply the approach discussed in Subsec. 4.2.2 to a reliable prediction of the radiative heat flux $\hat{q}_{rad}$ . . . . .	61
5.2 Comparison between the Populations of the Electronic States obtained in a region close to the shock by means of a Collisional Radiative model (black points), a Multi-Temperature model (red line) (a) and a Stochastic Multi-Temperature (blue lines) (b). . . . .	62
6.1 Application of the two approaches discussed in Sec. 4.2 (Kennedy and O'Hagan's strategy (a) and the method of Olivier <i>et al.</i> (b)) to the problem of validating the Park's TTv model predictions of the Population of the Nitrogen 5th Electronic Level. . . . .	66
6.2 Collisional Radiative Solution for the Population of Nitrogen 5th Electronic State in the first scenario, $P_0 = 39.9\text{Pa}$ , $T_0 = 195\text{K}$ and $u_0 = 10340\text{m/s}$ (a), and in the second one, $P_0 = 2\text{Pa}$ , $T_0 = 195\text{K}$ and $u_0 = 13360\text{m/s}$ (b). . . . .	67
6.3 Scenario 1: Sensitivity of the Nitrogen 5th Electronic State Population to each of the MT Parameters in function of the distance from the shock. . . . .	71

6.4 Scenario 1: Contribution of each of the MT Parameters to the Population of the Nitrogen 5th Electronic State. Sensitivity analyzed at three distances from the shock: 0.03cm (a), 0.07cm (b), 2cm (c) and 2.6cm (d).	71
6.5 Scenario 2: Sensitivity of the Nitrogen 5th Electronic State Population to each of the MT Parameters in function of the distance from the shock.	72
6.6 Scenario 2: Contribution of each of the MT Parameters to the Population of the Nitrogen 5th Electronic State. Sensitivity analyzed at three distances from the shock: 1.05cm (a), 3cm (b) and 8.05cm (c).	72
6.7 Scenario 1: Sensitivity of the Nitrogen 5th Electronic Population to each of the Stochastic MT Parameters in function of the shock distance.	73
6.8 Scenario 1: Contribution of each of the Stochastic MT Parameters to the Population of the Nitrogen 5th Electronic State. Sensitivity analyzed at three distances from the shock: 0.03cm (a), 0.07cm (b), 2cm (c) and 2.6cm (d).	73
6.9 Scenario 2: Sensitivity of the Nitrogen 5th Electronic State Population to each of the Stochastic MT Parameters in function of the distance from the shock.	74
6.10 Scenario 2: Contribution of each of the Stochastic MT Parameters to the Population of the Nitrogen 5th Electronic Level. Sensitivity analyzed at three distances from the shock: 1.05cm (a), 3cm (b) and 8.05cm (c).	74
6.11 Posterior Distributions of the Calibrated MT Parameters.	78
6.12 Correlation between the Calibrated MT Parameters.	79
6.13 Correlation between the MT Calibrated Parameters $A_{N_2+N}$ , $A_{N_2+N_2}$ , $\sigma_C$ and $C_{N_2}$	80
6.14 Posterior Distributions of the Calibrated Parameters of the Stochastic MT.	81
6.15 Posterior Distributions of the Calibrated Parameters of the Stochastic MT.	82
6.16 Correlation between the Calibrated Parameters of the Stochastic MT.	82
6.17 Posterior Distribution of the Calibrated MT Parameters.	83
6.18 Correlation between the Calibrated MT Parameters.	84
6.19 Correlation between the MT $A_{N_2+N}$ , $C_{N_2}$ and $\sigma_C$ .	84
6.20 Posterior Distributions of the Calibrated Parameters of the Stochastic MT.	85
6.21 Posterior Distributions of the Calibrated Parameters of the Stochastic MT.	86
6.22 Correlation between the Calibrated Parameters of the Stochastic MT.	86
6.23 Comparison between the Parameters Posterior Distributions of the Multi-Temperature (dashed lines) and of the Stochastic Multi-Temperature (solid lines). The red color refers to Scenario 1, while the blue indicates Scenario 2.	87
6.24 Comparison between the Hyperparameters Posterior Distributions. Red color refers to Scenario 1, while the blue indicates Scenario 2.	88
6.25 Likelihood Posterior Distribution for the Multi-Temperature (dashed lines) and of the Stochastic Multi-Temperature (solid lines). Red color refers to Scenario 1, while the blue indicates Scenario 2.	88
6.26 Posterior Distribution of N(5) Electronic State Population (i.e, Observable Quantity) (a), zoomed in the region close to the shock (b).	90

6.27 Posterior Distribution of the Nitrogen Electronic States with distance from the shock $x = 0.18cm$ (a) with the relative 5th Electronic State zoomed in Fig. (b). . . . .	91
6.28 Posterior Distribution of the Nitrogen Electronic States with distance from the shock $x = 0.6cm$ (a) with the relative 5th Electronic State zoomed in Fig. (b). . . . .	92
6.29 Posterior Distribution of the Nitrogen Electronic States with distance from the shock $x = 2.5cm$ (a) with the relative 5th Electronic State ( $10.687eV$ ) zoomed in Fig. (b). . . . .	93
6.30 Posterior Distribution of N(5) Electronic State Population (i.e, Observable Quantity) (a), zoomed in the region close to the shock (b). . . . .	94
6.31 Posterior Distribution of N(5) Electronic State Population analyzed at $0.05cm$ from the shock. . . . .	95
6.32 Posterior Distribution of N(5) Electronic State Population (i.e: Observable Quantity). . . . .	96
6.33 Posterior Distribution of the Nitrogen Electronic States with distance from the shock $x = 0.12cm$ (a) with the relative 5th Electronic State ( $10.687eV$ ) zoomed in Fig. (b). . . . .	97
6.34 Posterior Distribution of the Nitrogen Electronic States with distance from the shock $x = 2cm$ (a) with the relative 5th Electronic State ( $10.687eV$ ) zoomed in Fig. (b). . . . .	98
6.35 Posterior Distribution of the Nitrogen Electronic States with distance from the shock $x = 6.7cm$ (a) with the relative 5th Electronic State ( $10.687eV$ ) zoomed in Fig. (b). . . . .	99
6.36 Posterior Distribution of the Nitrogen Electronic States with distance from the shock $x = 8cm$ (a) with the relative 5th Electronic State ( $10.687eV$ ) zoomed in Fig. (b). . . . .	100
6.37 Posterior Distribution of N(5) Electronic State Population (i.e: Observable Quantity) obtained through the Stochastic Multi-Temperature. . . . .	101

# List of Tables

6.1	Occurring Reactions.	65
6.2	Inflow Conditions.	68
6.3	Model Parameters and their variabilities.	69
6.4	Stochastic Model Hyperparameters and their variabilities.	69
6.5	Ranking of Multi-Temperature and the Stochastic Multi-Temperature Model Parameters by Importance	75
6.6	Prior Distributions for the Parameters and Hyperparameters.	76
6.7	SMUQ Inputs.	77



# Bibliography

- [1] J.D. Anderson. *Hypersonic and High Temperature Gas Dynamics*. McGraw-Hill series in aeronautical and aerospace engineering. American Institute of Aeronautics and Astronautics, 2000.
- [2] Surzhikov ST. Radiative-collisional models in non-equilibrium aerothermodynamics of entry probes. *J. Heat Transfer*, 134(3):031002–031002–11, 2012.
- [3] W.G. Vincenti and C.H. Kruger. *Introduction to physical gas dynamics*. Krieger, 1967.
- [4] Peter A. Gnoffo. Planetary-entry gas dynamics. *Annual Review of Fluid Mechanics*, 31(1):459–494, 1999.
- [5] Alessandro Munafo. *Multi-Scale models and computational methods for aerothermodynamics*. Ph.d. thesis, Ecole Centrale Paris, Jan 2014.
- [6] M. Mitchner and C.H. Kruger. *Partially ionized gases*. Wiley series in plasma physics. Wiley, 1973.
- [7] C. Park. *Nonequilibrium Hypersonic Aerothermodynamics*. Wiley, 1990.
- [8] Marco Panesi. *Physical models for nonequilibrium plasma flow simulations at high speed re-entry conditions*. Ph.d. thesis, von Karman Institute / Universit degli studi di Pisa, July 2009.
- [9] P.A. Thompson. *Compressible-fluid dynamics*. Control Systems Engineering Series. McGraw-Hill, 1972.
- [10] Michael J. Moran and Howard N. Shapiro. *Fundamentals of engineering thermodynamics*. Wiley, 1998.
- [11] G.A. Bird. *Molecular Gas Dynamics and the Direct Simulation of Gas Flows*. Oxford engineering science series. Clarendon Press, 1998.

- [12] D. R. Bates, A. E. Kingston, and R. W. P. McWhirter. Recombination between electrons and atomic ions. i. optically thin plasmas. *Proceedings of the Royal Society of London. Series A, Mathematical and Physical Sciences*, 267(1330):297–312, 1962.
- [13] N.M. Laurendeau. *Statistical Thermodynamics: Fundamentals and Applications*. Cambridge University Press, 2005.
- [14] K. Miki, M. Panesi, E. E. Prudencio, and S. Prudhomme. Estimation of the nitrogen ionization reaction rate using electric arc shock tube data and bayesian model analysis. *Physics of Plasmas*, 2012.
- [15] Yen Liu, Marco Panesi, Amal Sahai, and Marcel Vinokur. General multi-group macroscopic modeling for thermo-chemical non-equilibrium gas mixtures. *The Journal of Chemical Physics*, 142(13), 2015.
- [16] Chul Park, John T. Howe, Richard L. Jaffe, and Graham V. Candler. Review of chemical-kinetic problems of future nasa missions, ii: Mars entries. *Journal of Thermophysics and Heat Transfer*, 8(1):9–22, 1 1994.
- [17] S. P. Sharma and D. W. Schwenke. Rate parameters for coupled rotation-vibration-dissociation phenomena in h<sub>2</sub>. *Journal of Thermophysics and Heat Transfer*, 5:4 (1):469–480, 1991.
- [18] P. A. Gnoffo, R. N. Gupta, and J. L. Shinn. Conservation equations and physical models for hypersonic air flows in thermal and chemical nonequilibrium. *NASA STI/Recon Technical Report*, (N 89:16115), 1989.
- [19] Christopher Owen Johnston. *Nonequilibrium Shock-Layer Radiative Heating for Earth and Titan Entry*. Ph.d. thesis, Virginia Polytechnic Inst. and State Univ., Nov 2006.
- [20] Deepak Bose, Evan McCorkle, Corinna Thompson, David Bogdanoff, Dinesh Prabhu, Gary Allen, and Jay Grinstead. Analysis and model validation of shock layer radiation in air. *46th AIAA Aerospace Sciences Meeting and Exhibit. Reno, Nevada*.
- [21] H.R. Griem. *Spectral line broadening by plasmas*. Pure and Applied Physics Series. New York ; London : Academic Press, 1974.
- [22] P.J. Roache. *Verification and Validation in Computational Science and Engineering*. Hermosa Publishers, Albuquerque, New Mexico, USA, 1998.
- [23] W.L. Oberkampf and C.J. Roy. *Verification and Validation in Scientific Computing*. Cambridge University Press, 2010.

- [24] T. A. Oliver, G. Terejanu, C. S. Simmons, and R. D. Moser. Validating predictions of unobserved quantities. *Computer Methods in Applied Mechanics and Engineering*, 283:1310 – 1335, 2015.
- [25] K. C. Estacio-Hiroms and E. E. Prudencio. Queso, quantification of uncertainty for estimation, simulation, and optimization: Version 0.45.3 users manual. Technical report, October 2012.
- [26] K. Miki, M. Panesi, and S. Prudhomme. Systematic validation of non-equilibrium thermochemical models using bayesian inference. *Journal of Computational Physics*, 298:125 – 144, 2015.
- [27] Angelikopoulos, P., C. Papadimitriou, and P. Koumoutsakos. Bayesian uncertainty quantification and propagation in molecular dynamics simulations: A high performance computing framework. *The Journal of Chemical Physics*, 137(14):144103, 2012.
- [28] K. Miki, M. Panesi, E.E. Prudencio, and S. Prudhomme. Probabilistic models and uncertainty quantification for the ionization reaction rate of atomic nitrogen. *Journal of Computational Physics*, 231(9):3871 – 3886, 2012.
- [29] S. Dutta, R. D. Braun, and C. D. Karlgaard. Uncertainty quantification for mars entry, descent, and landing reconstruction using adaptive filtering. *Journal of Spacecraft and Rockets*, 51:3:967–977, May-June 2014.
- [30] Marc C. Kennedy and Anthony O'Hagan. Bayesian calibration of computer models. *Journal of the Royal Statistical Society: Series B (Statistical Methodology)*, 63(3):425–464, 2001.
- [31] A. Tarantola. *Inverse Problem Theory and Methods for Model Parameter Estimation*. Society for Industrial and Applied Mathematics, 2005.
- [32] R. T. Cox. Probability, frequency and reasonable expectation. *American Journal of Physics*, 14(1):1–13, 1946.
- [33] D. S. Sivia and J. Skilling. *Data analysis : a Bayesian Tutorial*. Oxford science publications. Oxford University Press, Oxford, New York, 2006.
- [34] C. P. Robert and G. Casella. *Monte Carlo Statistical Methods*. Springer Texts in Statistics, Springer-Verlag New York, Inc., Secaucus, NJ, USA, 2005.
- [35] K. Mosegaard and A. Tarantola. *Probabilistic Approach to Inverse Problems*. International Handbook of Earthquake and Engineering Seismology, Part A., p 237-265, Academic Press, 2002.

- [36] Dimitris Bertsimas and John Tsitsiklis. Simulated annealing. *Statist. Sci.*, 8(1):10–15, 02 1993.
- [37] Andrew Gelman and Donald B. Rubin. Inference from iterative simulation using multiple sequences. *Statist. Sci.*, 7(4):457–472, 11 1992.
- [38] Antonietta Mira Peter J. Green. Delayed rejection in reversible jump metropolis-hastings. *Biometrika*, 88(4):1035–1053, 2001.
- [39] H. Haario, M. Laine, A. Mira, and E. Saksman. Dram: Efficient adaptive mcmc. *Statistics and Computing*, 16(4):339–354.
- [40] Heikki Haario, Eero Saksman, and Johanna Tamminen. An adaptive metropolis algorithm. *Bernoulli*, 7(2):223–242, 04 2001.
- [41] B. M. Adams et al. Dakota, a multilevel parallel object-oriented framework for design optimization, parameter estimation, uncertainty quantification, and sensitivity analysis: Version 6.3 users manual. Technical report, July 2014.
- [42] Technical report.
- [43] G. Casella and E. I. George. Explaining the gibbs sampler. *The American Statistician*, 46(3):167–174, 1992.
- [44] Quanhua Sun and Graham V. Boyd, Iain D. Nd Candler. A hybrid continuum/particle approach for modeling subsonic, rarefied gas flows. *Journal of Computational Physics*, 194(1):256–277, 10.02.2004.
- [45] M. Panesi, T. Magin, A. Bourdon, A. Bultel, and O. Chazot. Fire ll flight experiment analysis by means of a collisional-radiative model. *Journal of Thermophysics and Heat Transfer*, 23:2:236–248, 2009.
- [46] M. Panesi, K. Miki, S. Prudhomme, and A. Brandis. On the assessment of a bayesian validation methodology for data reduction models relevant to shock tube experiments. *Computer Methods in Applied Mechanics and Engineering*, 213:216:383 – 398, 2012.
- [47] T. A. Oliver and R. D. Moser. Bayesian uncertainty quantification applied to rans turbulence models. *Journal of Physics: Conference Series*, 318(4):042032, 2011.
- [48] I. Babuška, F. Nobile, and R. Tempone. A systematic approach to model validation based on bayesian updates and prediction related rejection criteria. *Computer Methods in Applied Mechanics and Engineering*, 197(2932):2517 – 2539, 2008. Validation Challenge Workshop.

- [49] G. Iaccarino and T. Magin. Uncertainty quantification in computational fluid dynamics. Technical report, NATO Science and Technology Organization, Papers presented at the AVT-193 RTO AVT-VKI Lecture Series held at the von Krmn Institute, Rhode St. Gense, Belgium on 24-28 October 2011., July 2013.
- [50] W. J. Browne and D. Draper. A comparison of bayesian and likelihood-based methods for fitting multilevel models. *Bayesian Anal.*, 1(3):473–514, 09 2006.
- [51] R.T. Cox. *Algebra of Probable Inference*. Johns Hopkins University Press, 1961.
- [52] M. Strong, J. E. Oakley, and J. Chilcott. Managing structural uncertainty in health economic decision models: a discrepancy approach. *Journal of the Royal Statistical Society: Series C (Applied Statistics)*, 61(1):25–45, 2012.
- [53] R. Stogner, P. T. Bauman, K. W. Schulz, R. Upadhyay, and A. Maurente. Uncertainty and parameter sensitivity in multiphysics reentry flows. *Aerospace Sciences Meetings, American Institute of Aeronautics and Astronautics, Orlando, FL*, 4-7, January 2011.